




12-2016

## Strategies for Controlling Bulk Heterojunction Morphology

Zach Daniel Seibers

*University of Tennessee, Knoxville, zseibers@vols.utk.edu*

Follow this and additional works at: [https://trace.tennessee.edu/utk\\_graddiss](https://trace.tennessee.edu/utk_graddiss)

 Part of the [Other Materials Science and Engineering Commons](#), [Polymer and Organic Materials Commons](#), and the [Semiconductor and Optical Materials Commons](#)

---

### Recommended Citation

Seibers, Zach Daniel, "Strategies for Controlling Bulk Heterojunction Morphology. " PhD diss., University of Tennessee, 2016.

[https://trace.tennessee.edu/utk\\_graddiss/4164](https://trace.tennessee.edu/utk_graddiss/4164)

This Dissertation is brought to you for free and open access by the Graduate School at TRACE: Tennessee Research and Creative Exchange. It has been accepted for inclusion in Doctoral Dissertations by an authorized administrator of TRACE: Tennessee Research and Creative Exchange. For more information, please contact [trace@utk.edu](mailto:trace@utk.edu).

To the Graduate Council:

I am submitting herewith a dissertation written by Zach Daniel Seibers entitled "Strategies for Controlling Bulk Heterojunction Morphology." I have examined the final electronic copy of this dissertation for form and content and recommend that it be accepted in partial fulfillment of the requirements for the degree of Doctor of Philosophy, with a major in Energy Science and Engineering.

Sydney M. Kilbey II, Major Professor

We have read this dissertation and recommend its acceptance:

John F. Ankner, Mark D. Dadmun, Brian K. Long, Bobby L. Sumpter

Accepted for the Council:

Carolyn R. Hodges

Vice Provost and Dean of the Graduate School

(Original signatures are on file with official student records.)

# Strategies for Controlling Bulk Heterojunction Morphology

A Dissertation Presented for the  
Doctor of Philosophy  
Degree  
The University of Tennessee, Knoxville

Zach Daniel Seibers

December 2016

© by Zach Daniel Seibers, 2016  
All Rights Reserved.

*This dissertation is dedicated to my wife Chelsea and my supportive family.*

# Acknowledgements

Completing this doctoral dissertation marks a tremendous accomplishment in my personal and professional life that would not be possible without the support of my colleagues, family, and friends.

I would like to thank my adviser, Professor S. Michael Kilbey II, for his unwavering support of my professional goals, as well as his understanding through the many personal challenges that I have faced during my tenure as a PhD student. It is undeniable that your ambition and strong work ethic has motivated me to exceed my own expectations and develop into the person I am today.

I would also like to acknowledge my committee members, who have helped me tremendously during my years at the University of Tennessee. Professor Mike Dadmun has helped me understand the complexities of neutron scattering and provided counsel on a wide range of topics related to polymer physics. Dr. Brian Long has pushed me to understand synthetic polymer chemistry and helped me develop my techniques in the laboratory. Dr. John Ankner has been relentless in his efforts to help me learn neutron reflectivity and analyze seemingly endless sets of data. The insightful conversations with Dr. Bobby Sumpter have been critical in designing and understanding the projects contained within my dissertation.

I am truly thankful for the Bredesen Center for Interdisciplinary Graduate Research and Education for providing me an educational platform to suit my personal and research-oriented interests. Just as important has been the Tennessee Solar Conversion and Storage using Outreach, Research, and Education (TN-SCORE)

program for their financial support and emphasis on community outreach. Together, these programs have presented me with a truly unique educational environment that has allowed me to develop an interdisciplinary skill set that is ahead of its time.

I would like to acknowledge numerous people who did not serve in an official capacity, but have aided me throughout my career. Dr. Holly Stretz, you believed in me before I believed in myself; I am truly thankful for your support and the opportunities you have presented me throughout the last 10 years. Dr. John Dunlap, your patience and seemingly endless knowledge of microscopy has been an invaluable resource that has allowed me to learn unimaginable techniques during my dissertation studies. Dr. Deanna Pickel helped me develop my polymer synthesis and mass spectroscopy techniques. On numerous occasions, Dr. Jan-Michael Carrillo provided unique insight from a simulation's perspective that dramatically influenced my work. My collaborators at Penn State University, Dr. Enrique Gomez, Dr. Thin Le, and Josh Litofsky. Your knowledge and willingness to help me learn the science driving organic electronics has played a huge role in my success as a PhD student.

I am also thankful for all of the current and past members of the Kilbey research group at the University of Tennessee: Bethany Aden, Evan Boone, Kamlesh Bornani, Graham Collier, Jessie Davis, Chaitra Deodhar, Ben Hopkins, Jiadi Hou, Camille Kite, Mike Kochemba, Rachel Ramirez, Sina Sabury, Xu Wang, and Jeremiah Woodcock. Enduring the "marathon" that is a dissertation would not have been possible without your friendship and support. I wish all of you the best in your future endeavors.

I would be remiss if I did not mention my friends and family for supporting my ambitions to pursue such a demanding career. From holidays to birthdays, my dissertation studies have pulled me away from numerous gatherings; your patience and understanding of which has not been overlooked. To my parents, Mom, Dad, Ashley, Aunt Storme, and my grandparents. Throughout my life you have supported my ambitions and never let me settle for anything less than my dreams, I have you to thank for giving me the confidence, intellect, and passion to pursue them. My

siblings, Matthew, Hunter, Ty, and Grace. I hope I have remained the positive role model and loving big brother that you deserve; not a day passes without me wishing I was back home with each of you. Robert French, even in the darkest of times you have helped me stay grounded and reminded me why I started this endeavor to begin with, our shared love for science.

Most of all I want to thank Chelsea. My anam cara, role model, and loving wife; you have sacrificed so much with me to make this doctorate a reality. Your unfaltering support has helped me overcome many obstacles in life and this PhD is no exception.



# Abstract

Organic photovoltaic devices have been extensively studied as a means to produce sustainable energy. However, the performance of organic-photovoltaic (OPV) devices is dependent upon a number of factors including the morphology of the active layer, device architecture, and processing conditions. Recent research has indicated that fullerenes in the bulk heterojunction are entropically driven to the silicon and air interfaces upon crystallization of P3HT, which occurs during thermal annealing. The first chapter of this research focuses on investigating the structure and function of end-tethered poly(3-hexylthiophene) chains to a transparent electrode as an anode buffer layer. Neutron reflectivity reveals that these P3HT brush layers have severe effects on the vertical distribution of PCBM across the depth of the BHJ films, the extent of which depends on the grafting density of the P3HT brush layer. These results are confirmed by energy-filtered transmission electron microscopy measurements.

Another emerging trend in the advancement of OPVs is through the addition of a third component to impose morphological or electronic benefits to BHJ-based devices. In Chapter 3 of this dissertation, three different low MW P3HTs are incorporated into BHJ films as additives to reveal fundamental aspects of their behavior as a function of size and loading level. The best performing loading levels for each additive are found to be inversely proportional to the MW of the P3HT additive and appear to be driven by a coarsening of BHJ film morphology. The incorporation of porphyrin-based additives into BHJ OPV devices has been an emerging trend in recent years due to their strong solar absorption and  $\pi - \pi$

interactions between PCBM nanoparticles and porphyrin centers. Building on these reports, and the investigations of low MW P3HTs, porphyrin-capped low MW P3HTs (PP-P3HT)s are synthesized and incorporated into BHJ films as additives. Although PP-P3HTs impose many substantial morphological benefits to BHJ films, these favorable properties are overshadowed by lackluster device performances, ostensibly due to the presence of the Si-O linkage between the porphyrin and P3HT chains.

# Table of Contents

<b>1</b>	<b>Introduction</b>	<b>1</b>
1.1	Motivation . . . . .	2
1.2	Organic Photovoltaic Devices . . . . .	3
1.3	Introduction to the Synthesis of P3HTs . . . . .	8
1.4	Characterization of P3HTs . . . . .	13
1.4.1	Size Exclusion Chromatography . . . . .	13
1.4.2	Nuclear Magnetic Resonance Spectroscopy . . . . .	14
1.4.3	MALDI-TOF Spectroscopy . . . . .	14
1.5	Characterization of BHJ Films . . . . .	17
1.5.1	OPV Device Performance . . . . .	18
1.5.2	Transmission Electron Microscopy . . . . .	20
1.5.3	Neutron Reflectometry . . . . .	22
1.5.4	Ellipsometry . . . . .	24
1.5.5	Differential Scanning Calorimetry . . . . .	26
1.6	Research Objectives . . . . .	28
<b>2</b>	<b>End-Tethered P3HTs as Anode Buffer Layer Replacement</b>	<b>31</b>
2.1	Abstract . . . . .	32
2.2	Introduction . . . . .	32
2.3	Results & Discussion . . . . .	36
2.4	Conclusions . . . . .	49

2.5	Experimental . . . . .	50
2.5.1	Synthesis of silane-terminated P3HTs . . . . .	50
2.5.2	Surface Preparation and Deposition . . . . .	51
2.5.3	Bulk Heterojunction Film Preparation . . . . .	52
2.5.4	Neutron Reflectometry . . . . .	52
2.5.5	Multiangle Ellipsometry . . . . .	53
2.5.6	Spectroscopic Ellipsometry . . . . .	53
2.5.7	Cross-Sectional Transmission Electron Microscopy . . . . .	54
<b>3</b>	<b>Low Molecular Weight P3HT Chains as BHJ Additives</b>	<b>55</b>
3.1	Abstract . . . . .	56
3.2	Introduction . . . . .	57
3.3	Results & Discussion . . . . .	61
3.3.1	Device Performance . . . . .	62
3.3.2	GI-SAXS . . . . .	64
3.3.3	GI-WAXS . . . . .	67
3.3.4	TEM . . . . .	69
3.3.5	Neutron Reflectivity . . . . .	69
3.3.6	Contact Angle . . . . .	74
3.4	Conclusions . . . . .	76
3.5	Experimental . . . . .	77
3.5.1	Device Fabrication & Performance . . . . .	77
3.5.2	X-Ray Scattering . . . . .	77
3.5.3	Energy-Filtered Transmission Electron Microscopy . . . . .	78
3.5.4	Neutron Reflectivity . . . . .	78
3.5.5	Contact Angle . . . . .	79
<b>4</b>	<b>Porphyrin-Capped P3HTs as Additives</b>	<b>81</b>
4.1	Abstract . . . . .	82
4.2	Introduction . . . . .	82

4.3	Results & Discussion . . . . .	86
4.3.1	Synthesis . . . . .	86
4.3.2	UV-Vis Spectroscopy . . . . .	88
4.3.3	Fluorescence Quenching . . . . .	92
4.3.4	X-Ray Diffraction . . . . .	93
4.3.5	Differential Scanning Calorimetry . . . . .	95
4.3.6	Device Performance . . . . .	99
4.4	Conclusions . . . . .	104
4.5	Experimental . . . . .	105
4.5.1	Synthesis of THTP . . . . .	105
4.5.2	Synthesis of allyl-P3HT . . . . .	106
4.5.3	Synthesis of PP-P3HT . . . . .	106
4.5.4	Uv-Vis and Fluorescence Spectroscopy . . . . .	106
4.5.5	Differential Scanning Calorimetry . . . . .	107
4.5.6	X-Ray Diffraction . . . . .	107
4.5.7	Device Performance . . . . .	107
<b>5</b>	<b>Summary, Conclusions, and Future Work</b>	<b>109</b>
	<b>Bibliography</b>	<b>113</b>
	<b>Appendices</b>	<b>144</b>
<b>A</b>	<b>Experimental Procedures and Techniques for Data Interpretation</b>	<b>145</b>
A.1	Synthesis of Poly(3-hexylthiophene)s . . . . .	146
A.1.1	Grignard Conversion to the Activated Monomer . . . . .	147
A.1.2	Preparation of GC-MS Sample . . . . .	147
A.1.3	Growth of P3HTs via the KCTP Mechanism . . . . .	147
A.2	Hydrosilylation of P3HTs . . . . .	149
A.3	Piranha Cleansing Method . . . . .	151

A.4	Derivation of Mass Balance in Binary Films for NR Modeling . . . . .	153
A.5	MALDI Analysis of Polymer End-Groups . . . . .	155
A.6	Cross-Sectional TEM Sample Preparation via the Liftout Method . . .	157
<b>B</b>	<b>Supporting Information</b>	<b>161</b>
B.1	Chapter 1 . . . . .	162
B.2	Chapter 2 . . . . .	163
B.2.1	SEC Elugrams . . . . .	163
B.2.2	NMR . . . . .	164
B.2.3	MALDI . . . . .	165
B.3	Chapter 3 Supporting Information . . . . .	166
B.3.1	List of P3HT-PCBM BHJ Additives . . . . .	166
B.3.2	GPC Elugrams for different MW P3HTs . . . . .	170
B.3.3	NMR of Different Low MW P3HTs . . . . .	171
B.4	Chapter 4 Supporting Information . . . . .	172
B.4.1	GPC of P3HT-PPs . . . . .	172
B.4.2	NMR of P3HT-allyl . . . . .	173
B.4.3	MALDI Spectra of P3HT-PP Intermediates . . . . .	174
B.4.4	Plots of $V_{oc}$ and FF as a Function of P3HT-PP Loading Level	175
<b>Vita</b>		<b>176</b>

# List of Tables

1.1	Reported $\Delta H_f$ values for P3HT . . . . .	27
2.1	End-tethered P3HT grafting densities . . . . .	39
3.1	Low MW P3HT properties . . . . .	62
3.2	Power conversion efficiencies for additive-modified films . . . . .	63
3.3	Contact angle measurements of BHJ components . . . . .	75
3.4	Wu model parameters . . . . .	80
4.1	PP-P3HT MW properties . . . . .	90
4.2	Thermal properties of BHJ blends . . . . .	97
4.3	DSC data for melt-point depression studies . . . . .	98
4.4	Power conversion efficiencies for BHJs containing porphyrin-capped P3HTs . . . . .	102
B.1	List of BHJ additives and PCEs . . . . .	166
B.2	List of BHJ additives . . . . .	167

# List of Figures

1.1	Organic photovoltaic device schematic . . . . .	5
1.2	Possible thiophene couplings . . . . .	8
1.3	GRIM preparation of regiospecific monomer . . . . .	9
1.4	Synthesis of P3HT . . . . .	11
1.5	GCMS chromatogram of DB3HT conversion . . . . .	12
1.6	$^1\text{H-NMR}$ spectrum for P3HT . . . . .	15
1.7	Example MALDI spectra for allyl-terminated P3HT . . . . .	17
1.8	Current-voltage diagram . . . . .	19
1.9	Energy-filtered TEM comparison . . . . .	21
1.10	Scattering length density profile . . . . .	25
2.1	Schematic for P3HT brush formation . . . . .	37
2.2	NR data & fits of P3HT brushes . . . . .	38
2.3	NR data & fits of BHJ films as cast atop P3HT brushes . . . . .	41
2.4	As-cast and annealed SLD profiles of BHJ films cast atop P3HT brushes	43
2.5	Spectroscopic ellipsometry measurements of annealed BHJ films cast atop P3HT brushes . . . . .	44
2.6	NR data & fits of annealed BHJ films atop P3HT brushes . . . . .	45
2.7	EF-TEM of brush-modified BHJ films . . . . .	48
3.1	MD simulations of BHJ films containing low MW P3HT additives . .	60
3.2	Illuminated and Dark J-V Curves . . . . .	64



3.3	GI-SAXS for low MW P3HT-modified films . . . . .	66
3.4	Critical loading level and PCE . . . . .	67
3.5	GI-WAXS detector images of BHJ films . . . . .	68
3.6	1D GI-WAXS diffraction patterns for BHJ films . . . . .	70
3.7	EF-TEM images of low P3HT-modified films . . . . .	71
3.8	Comparison of simulated & experimental NR measurements . . . . .	72
3.9	Comparison of simulated & experimental SLD profiles . . . . .	73
4.1	Reaction scheme for PP-P3HTs . . . . .	88
4.2	NMR of THTP and PP-P3HTs . . . . .	89
4.3	UV-Vis spectra of THTP, P3HT, and PP-P3HT . . . . .	91
4.4	UV-Vis of porphyrin-P3HTs in solution and film . . . . .	92
4.5	UV-Vis spectra of P3HT and PP-P3HT thin films . . . . .	93
4.6	UV-Vis spectra for neat PP-P3HT and PP-P3HT/PCBM thin films . . . . .	94
4.7	Fluorescence quenching of PP-P3HTs with PCBM . . . . .	95
4.8	XRD data for porphyrin-capped P3HTs . . . . .	96
4.9	Melting temperatures of allyl- and PP-P3HT as a function of PCBM . . . . .	100
4.10	J-V curves for PP-P3HT devices . . . . .	101
4.11	PCE and $J_{sc}$ as a function of PP-P3HT loading level . . . . .	103
A.1	Schlenk flask used for hydrosilylation reactions . . . . .	150
A.2	MALDI spectra of ideal P3HT-HBr . . . . .	156
A.3	FIB lift out sequence 1 . . . . .	158
A.4	FIB lift out sequence 2 . . . . .	159
B.1	SEC elugrams for allyl-P3HT . . . . .	163
B.2	NMR spectra for allyl-P3HT . . . . .	164
B.3	MALDI allyl-terminated P3HTs . . . . .	165
B.4	SEC elugrams for low MW P3HTs . . . . .	170
B.5	NMR spectra for each low MW P3HT . . . . .	171

B.6	SEC elugrams for allyl- and porphyrin-terminated P3HTs . . . . .	172
B.7	NMR spectra of allyl-terminated P3HT . . . . .	173
B.8	MALDI spectra for allyl-terminated P3HT . . . . .	174
B.9	Voc as a function of P3HT-PP loading level . . . . .	175
B.10	FF as a function of P3HT-PP loading level . . . . .	175

# Chapter 1

## Introduction

## 1.1 Motivation

The growing global demand for energy and climate issues associated with greenhouse gas emissions originating from the combustion of fossil fuels have driven an international effort to develop environmentally-friendly means of energy production. One of the most promising forms of energy production is through direct photovoltaic conversion of incoming sunlight via the photoelectric effect. Solar panels based on doped crystalline-silicon (Si) dominate current energy markets due to their exceptional efficiency that has exceeded 24% and operating lifetimes of up to 30 years. Despite their remarkable performance, the widespread adoption of traditional Si-based solar cells is limited by their high manufacturing costs that arise due to the extreme processing conditions required during production.<sup>1</sup> Furthermore, the weight and rigidity of traditional panels limits their practical installation to rooftops or dedicated large open spaces. In response to these pitfalls, a great deal of effort in recent decades has focused on the development of alternative solar conversion technologies that will enable solar energy to become a significant component of future energy infrastructure.

One promising class of solar cells that meets many of these challenges are based on blends of organic donor and acceptor materials, such as  $\pi$ -conjugated polymers and fullerene nanoparticles, respectively. These organic photovoltaic (OPV) devices are compatible with solution-based processing techniques and feature few exotic metals, allowing their production cost to be drastically lower than traditional solar cells. These attributes, combined with the flexible and lightweight nature of OPVs, make them a promising technology for large-scale deployment in a variety of applications. Studies have indicated that long-term performance efficiencies of 15% are necessary to make commercial OPV devices competitive with existing solar cell technologies based on Si.<sup>2</sup> These prospects have inspired a major research effort focused on the development of new materials and processing techniques to increase the performance and lifetime of OPV devices. The scientific community has responded with substantial

performance enhancements through the design of low bandgap, donor-type polymers, photon-trapping coatings, and electrode materials that have thus far culminated in lab-scale devices surpassing 11% efficiency.<sup>3-5</sup> While promising, these devices require processing techniques unfeasible for commercial-scale panel production, or suffer from limited performance lifetimes stemming either from UV-induced degradation pathways or catastrophic inter-layer diffusion, or a combination of the two.

Although considerable OPV performance increases have resulted from materials development, comparatively less progress has been made towards optimizing and stabilizing the morphology of the active layer. The inherent physical and chemical differences between typical donor (polymers) and acceptor (nanoparticles) materials ultimately result in a thermodynamically-driven separation between the two phases. The problems associated with this lack of morphological control are exaggerated when devices are tested under real-world operating conditions, such as thermal cycling or moisture exposure. To overcome these material incompatibilities, it is necessary to explore methods by which these thermodynamic barriers can be reduced or alleviated without sacrificing performance or the solution-processible nature of OPV panel manufacturing.

## 1.2 Organic Photovoltaic Devices

The first OPVs were reported in the late 1970s in response to a national effort to reduce the dependency on foreign oil as an energy source.<sup>6,7</sup> These primitive devices featured poor power conversion efficiencies (PCEs) due to the low concentration and limited mobility of free-charge carriers from the donor materials. OPV technology remained stagnant for nearly 20 years, at which point concerns over climate change and the growing global demand for energy has reinvigorated research focused on cost-effective energy sources as alternatives to fossil fuels. Spurred by these driving forces, many important milestones have been reached that have led to the relatively quick advancement of OPV devices. Among these achievements is the reported synthesis of

well-defined  $\pi$ -conjugated polymers that absorb more of the incoming solar radiation and feature higher charge mobilities than previous materials.<sup>8</sup> Just as important was the realization that electron transfer from an excited donor-type polymer to fullerene acceptors occurs rapidly with exceptionally high quantum efficiency, which is extremely important for charge-carrier separation in PV cells.<sup>9</sup>

While many factors influence the performance of OPV devices, arguably the most important component is the active layer because it is responsible for the generation, separation, and transport to and extraction at the anode or cathode, respectively. Major gains in performance were achieved with the discovery of the bulk heterojunction (BHJ) active layer design, wherein the donor polymer and acceptor fullerene are mixed in solution before casting.<sup>9,10</sup> This architecture, which is marked by nanoscale donor-rich and acceptor-rich domains in intimate contact, which significantly increases the interfacial area between the donor and acceptor materials compared to traditional bi-layer OPV devices. In addition, the BHJ structure also maintains continuous pathways to the anode and cathode. Typical benchmark BHJ OPVs feature an active layer composed of poly(3-hexylthiophene) (P3HT) and phenyl-C<sub>61</sub>-butyric acid methyl ester (PCBM) fullerenes as the donor and acceptor materials, respectively.

Figure 1.1 depicts four critical steps for conversion of sunlight to electricity. The sequence includes 1) exciton generation, 2) exciton migration, 3) exciton dissociation, and 4) charge extraction. Exciton generation occurs upon absorption of a photon by the donor polymer that excites an electron from the valence band to the conductive band, forming a relatively unstable electron-hole pair known as an exciton. After generation, these excitons must migrate to the donor/acceptor (DA) interface without undergoing band-to-band recombination, in which the exciton collapses to its empty valence band state. After migrating to a DA interface, the exciton is dissociated into an electron ( $e^-$ ) and a hole ( $h^+$ ) due to a difference in energy level of the highest occupied molecular orbital (HOMO) of the donor and lowest unoccupied molecular orbital (LUMO) of the acceptor. The hole and electron are then transported through

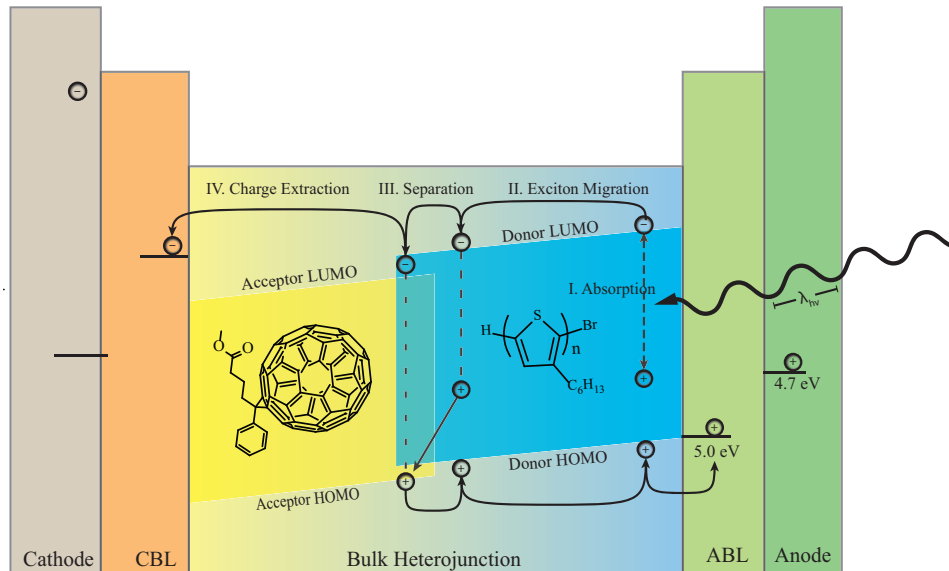


**Figure 1.1:** Schematic of photoelectric process within BHJ organic solar cell consisting of P3HT as the donor polymer and PCBM as the acceptor fullerene. The life cycle of the generated charge as shown in steps I-IV.

continuous donor and acceptor domains to the cathode and anode, respectively.<sup>11</sup> One or both electrodes are often coated by charge-selective interfacial buffer layers that preferentially allow electrons and holes to pass to the cathode and anode, respectively. Buffer layers must be chosen carefully to satisfy the demands of the physical and electronic interactions while also creating and maintaining an electronic asymmetry required to bias the device.<sup>12-14</sup>

The sensitivity of these electronic processes to the conditions of the active layer have been well studied, and critical design parameters have been identified such as *a*) the efficient absorption of sunlight (bandgap), *b*) crystallization of the donor polymer to increase conductivity,<sup>15</sup> *c*) domain widths on the order of the exciton diffusion length-scale ( $\approx 10-15$  nm), and *d*) presence of continuous domains of the donor and acceptor phases to their respective electrodes.<sup>11</sup> In particular, it has been shown that the efficiency of these electronic processes is highly dependent

on the interfacial area between the donor and acceptor domains.<sup>16</sup> Thus, there is a trade-off between maximizing donor-acceptor (DA) interfacial area and retaining sufficiently continuous domains so that electrons and holes reach their respective electrode. Although these specifications have been recognized, limited success in achieving consistent control over the morphology of BHJ blends has been reported in part due to inherent incompatibilities between the donor polymer and acceptor nanoparticle.

Investigations of fullerene loading in BHJ-based devices have revealed that optimal performance is achieved at blend compositions of 1:1 PCBM:P3HT in lab-scale samples.<sup>17</sup> Neutron reflectometry (NR) and X-ray studies of bilayer films suggest that the thermodynamic loading limit of PCBM in a P3HT film occurs at a far lower level of  $\approx 20\%$ .<sup>18</sup> Perhaps stemming from an abundance of PCBM, various NR experiments consistently report that fullerenes migrate to one<sup>19-21</sup> or both interfaces,<sup>22-24</sup> depending on the device architecture and processing methods. These foundational works have inspired a range of studies focused on understanding the kinetic details of BHJ film morphology and processing effects.

Optical and electron microscopy have been used to link PCBM aggregation to the crystallization of P3HT, which expunges PCBM into the amorphous regions of the polymer matrix.<sup>15,18,25,26</sup> These observations are reinforced by numerous X-ray studies reporting increases in crystallinity and PCBM aggregate size upon thermal and solvent annealing.<sup>27-30</sup> Thermal annealing of BHJ films has been segmented into two distinct time windows: Initially, within 5 min, crystallization of P3HT occurs, followed by the formation of PCBM fullerene aggregates for up to 30 min.<sup>28</sup> It has been suggested that the morphology of the BHJ is largely dependent on the surface energy of the substrate or buffer layer upon which the film is cast;<sup>31,32</sup> however, neutron reflectivity (NR) studies have brought this idea into question because no changes in film morphology were observed when the hydrophilicity of the substrate was manipulated.<sup>33</sup> There are also numerous studies suggesting that PCBM preferentially migrates to confined interfaces upon thermal annealing, regardless of their type or



makeup (e.g., anode, cathode, or buffer layers).<sup>29,34,35</sup> These segregation tendencies have also been confirmed through cross-sectional transmission electron microscopy experiments from which detailed depth profile information has been obtained.<sup>36</sup> The disparity of these results underscores the sensitivity of BHJ films, and, therefore, OPV performance, to the choice of materials and processing conditions used during device fabrication.

Many materials and processing strategies have been used to control the morphology of OPV materials and eliminate their tendency to phase separate. Compared to typical single-solvent casting processes, the use of solvent mixtures has been shown to provide access to interesting morphological states and increase device performance.<sup>37-40</sup> The morphology of BHJ films is also responsive to solvent vapor annealing, where heated solvent vapors provide mobility to one or more of the components in the film.<sup>41-43</sup> There is also a growing number of polymeric and block-copolymeric additives that have shown to increase device performance, thereby providing an additional handle by which BHJ morphology can be manipulated.

Although significant improvements in device performance have been attained over the last twenty years, OPV devices lag in performance and lack the stability needed to be competitive with existing photovoltaic conversion technologies. Given the lack of consistency between reports, it is also clear that a better understanding of the morphological development of BHJ films is paramount to harnessing their transient nature. Overcoming the deficiencies that limit OPV performance warrants clarification of links between the design of materials, layer arrangement, film processing, and device performance. This knowledge can be used to develop novel or appropriate pathways by which BHJ morphology can be influenced through controllable yet scalable methods.

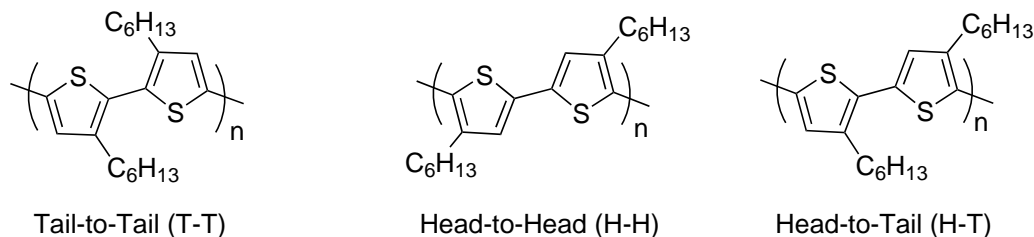


**Figure 1.2:** Three possible monomer couplings for P3HTs: tail-to-tail (TT), head-to-head (HH), and head-to-tail (HT).

### 1.3 Introduction to the Synthesis of P3HTs

The donor polymer is a critical component in the overall performance of OPV devices because it is responsible for the absorption of incoming sunlight and the generation of excitons. Of the many prospective materials, polythiophenes stand out as promising candidates because of their electron-rich backbone and appropriate bandgap for efficient solar absorption. The first generations of polythiophenes featured broad molecular weight distributions and were insoluble in most organic solvents, rendering them impractical for use in OPV applications.<sup>44,45</sup> Years later, it was discovered that the addition of alkyl chains on the thiophene ring improved the solubility of polythiophenes in many organic solvents; however, early devices demonstrated limited device performances due to a lack of charge carrier mobility.<sup>46</sup> The poor charge mobilities were later attributed to a significant number of head-to-head (HH) or tail-to-tail (TT) linkages that limited the  $\pi - \pi$  stacking between polymer chains.<sup>47-49</sup> The three possible coupling between P3HT monomer units is shown in Figure 1.2.

Perhaps one of the biggest advances on the field of OPVs occurred in the early 1990s by Chen and Rieke: they developed the synthesis of highly regioregular poly(3-hexylthiophene) (rr-P3HT).<sup>50</sup> Their work introduced the concept of using highly reactive ZnBr stereoregular monomers that can be coupled using a Pd catalyst to obtain high abundance of head-to-tail (HT) couplings by sterically hindering the HH and TT coupling reaction mechanisms. Later, McCullough used lithium diisopropylamide and magnesium dibromide at sub-zero reaction temperatures to

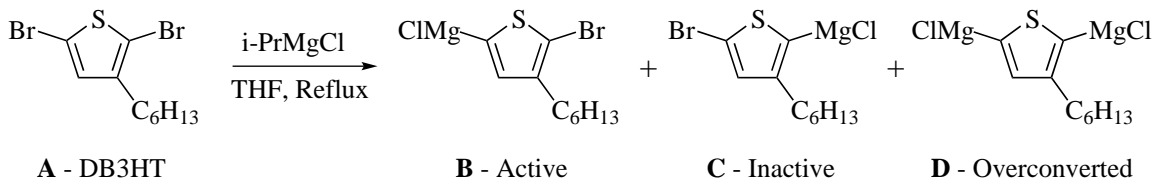


**Figure 1.3:** GRIM synthesis of regiospecific monomer used to prepare highly rr-P3HTs.

create the stereospecific monomer.<sup>49</sup> While the rr-P3HTs obtained via these pathways featured the properties necessary for higher performing OPV devices, their synthesis involved extensive monomer preparations and cryogenic reaction conditions that are economically unfeasible at commercial scale.

Eventually, McCullough pioneered preparation of the regiospecific monomer by use of Grignard reagents, which would become the basis of the Grignard metathesis (GRIM) method for preparing P3HTs, which is a type of Kumada Catalyst-transfer polycondensation (KCTP).<sup>51,52</sup> Figure 1.3 shows this monomer preparation route that is advantageous because it relies on the reactive nature of the magnesiocloride functional groups for polymer growth. This aspect of the KCTP method is far superior because device-quality P3HT can be synthesized using commercially available starting materials and reaction conditions that are feasible at a production scale. A central enabling feature of the GRIM method is the generation and reactivity of the regiospecific monomer, 2-bromo-5-magnesiocloro-3-hexylthiophene **B**, which yields P3HTs with HT couplings. In order to create P3HT with high regioregularity it is essential to not "over-convert" the 2,5-dibromo-3-hexylthiophene (DB3HT), which would lead to the over-converted monomer product, **D**, which is known to broaden the molecular weight distribution and result in loss of control over end-group composition.<sup>53</sup>

The improved monomer preparation methods and use of specially designed catalysts comprise a practical approach to synthesize highly regioregular ( $\geq 99\%$ ) P3HT, or rr-P3HT, with tight control over the molecular weight.<sup>51,52</sup> Illustrated in

Figure 1.4 is the mechanism of KCTP in which monomers are coupled by the repeated oxidative addition (OA), transmetalation (TM), and reductive elimination (RE) steps involving the activated monomer units and the Ni catalyst. Regioselective monomer assembly occurs due to steric interactions between the ligands of the [1,3-Bis(diphenylphosphino)propane]dichloronickel(II) (Ni(dppp)Cl<sub>2</sub>) catalyst and the hexyl side-chain of the active monomer **B**. Although the KCTP process is a condensation polymerization, the Ni catalyst remains associated with a growing polymer chain end and, therefore, the polymerization resembles a chain-growth polymerization. This chain-growth-like nature enables control over the degree of polymerization (DP), or number of repeat units, by adjusting the molar ratio of activated monomer to the Ni catalyst as shown in Equation 1.1.  $N_{DB3HT}$  and  $N_{Ni}$  represent the moles of DB3HT monomer and Ni catalyst, respectively, and  $X_{act}$  is the fraction of the active isomer after the Grignard conversion, which is typically  $\approx 80\%$ .

$$DP = \frac{X_{act}N_{DB3HT}}{N_{Ni}} \quad (1.1)$$

Another advantage of the growth of P3HT by KCTP is the chemical versatility and control over the end groups of the polymer chain. Control over the end groups of P3HT is critical because it enables access to numerous post-polymerization modification strategies for a variety of applications.<sup>53,55-59</sup> The most prevalent origins of loss of control over end groups arises due to conversion to di-converted monomer or the presence of unreacted Grignard reagent, which will react with the Br groups at the chain ends during polymer growth.<sup>53</sup> In this dissertation, complete conversion of the DB3HT monomer is ensured by controlling the stoichiometry (by adding a slight excess of DB3HT monomer) and monitoring by gas chromatography mass spectroscopy (GC-MS). An example chromatogram for and ideal conversion is shown in Figure 1.5. This spectrum shows a small amount ( $\leq 2\%$ ) of unconverted monomer which has no deleterious impact on the KCTP mechanism. The peak location of the over-converted monomer is shown in red for reference.

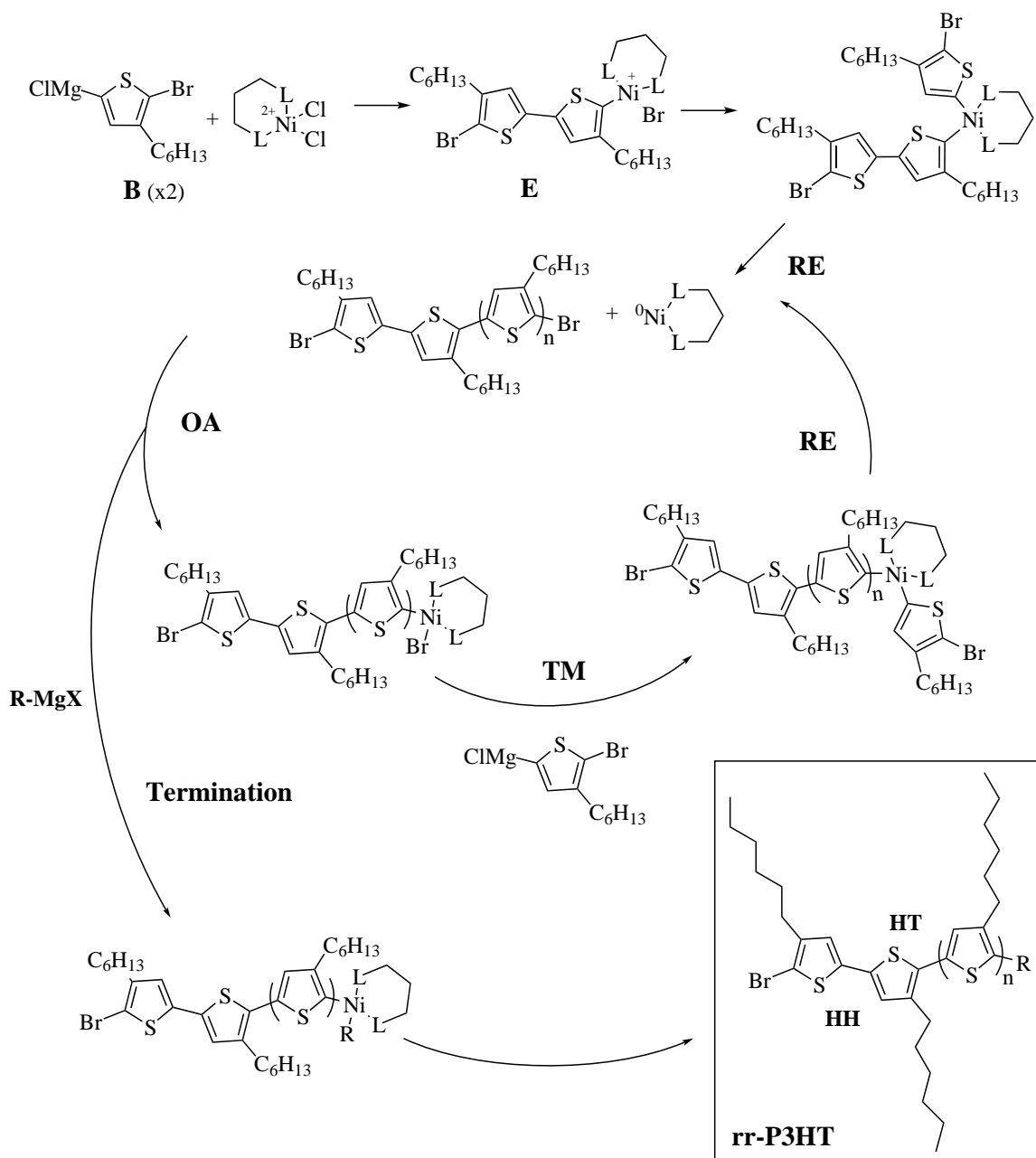


**Figure 1.4:** Mechanism of KTCP reaction used to synthesize P3HT in this dissertation work. P3HTs are grown by the repeated oxidative addition (OA), Transmetalation (TM), and Reductive Elimination (RE) cycles. Adapted from Jeffries-El et al.<sup>54</sup>

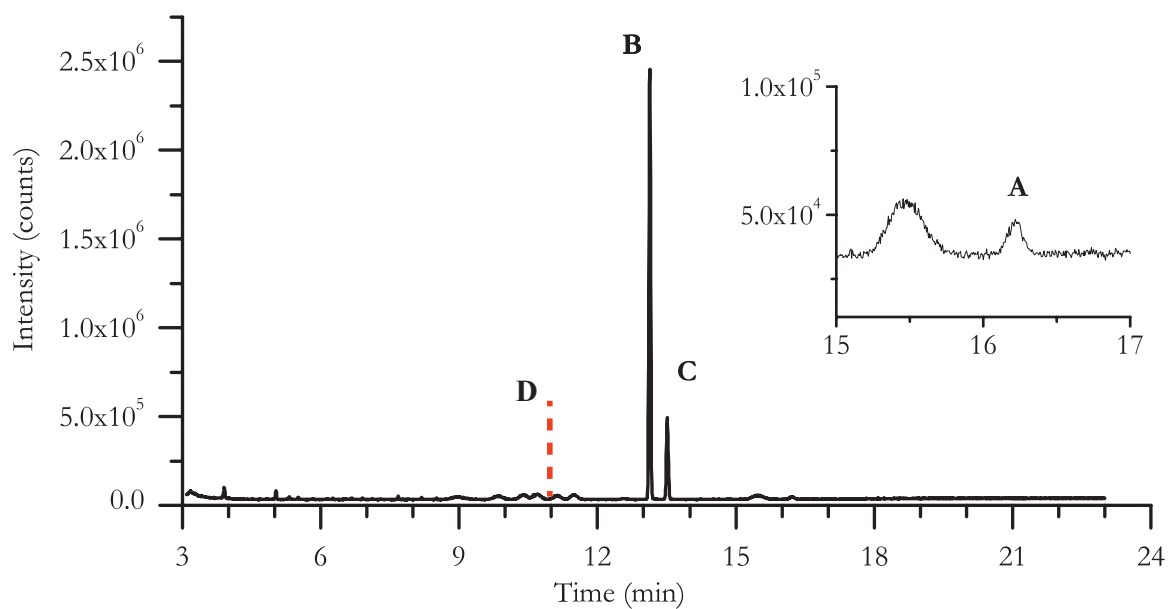


**Figure 1.5:** Example GC-MS chromatogram after converting the DB3HT monomer **A** conversion to the active **B** and inactive **C** isomers. By only converting 98% of the DB3HT no over-converted monomer is present, as indicated by the unconverted monomer peak shown in the in-set at 16.4 min. The unconverted monomer peak **D** is shown as the red dashed line at 11 min for reference.

## 1.4 Characterization of P3HTs

Given the established links between molecular properties of polymers and their behaviors in solution and in films, a crucial component of this dissertation is the synthesis and thorough characterization of various P3HT products. Establishing accurate structure-property relationships relevant to BHJ morphology and OPV device performance requires a detailed understanding of the chemical structure and properties of the polymers synthesized. For P3HTs in particular, MW, regioregularity (RR), and end-group composition have been linked to changes in electronic and morphological properties of OPV devices. Numerous methods to assess the MW and polydispersity of P3HTs have been reported, however, each have their own advantages and disadvantages in their experimental implementation and data interpretation.

### 1.4.1 Size Exclusion Chromatography

Size exclusion chromatography (SEC) is the simplest method for determining MW and polydispersity of polymeric materials. During SEC, a polymer sample is dissolved in a mobile solvent phase and passed through a column that separates the polymer chains by hydrodynamic volume. These different sized polymers elute from the column at different times and, through a pre-determined calibration, are transcoded into a molecular weight (relative to a standard). From SEC measurements, the relative number-average ( $M_N$ ) and weight-average ( $M_W$ ) MW values are obtained from the analysis of the elugram and the polydispersity index can be calculated using Equation 1.2.

$$PDI = M_W/M_N \quad (1.2)$$

One well-known difficulty in assessing P3HT MW via SEC is overcoming their tendency to aggregate, which is due to the rod-like conformation that is adopted by P3HT in solution. As a result, P3HTs feature an inflated hydrodynamic volume, which results in relatively overestimated MWs compared to PS standards.<sup>58,60</sup>

Because of this overestimation, it has become common practice to complement MWs measured by SEC with values determined by other techniques.

### 1.4.2 Nuclear Magnetic Resonance Spectroscopy

Nuclear magnetic resonance (NMR) spectroscopy is another useful tool to measure the MW and regioregularity of P3HTs. An example NMR of P3HT is shown in Figure 1.6. The RR of P3HT is calculated by comparing proton signals (of the 4-position of the thiophene ring) of the head-to-tail coupled monomers (6.98 ppm) to those of head-to-head coupling (7.02 ppm). These peaks are depicted in Figure 1.6 as **a** for the HT coupled monomers and **a'** for the HH coupled monomers.

For highly regioregular P3HTs used in this work, which predominantly feature HT coupled repeat units,  $^1\text{H}$ -NMR is used to estimate MWs by the integrated signals attributed to the protons on the  $\alpha$  carbon of the hexyl side chain nearest the thiophene ring. As shown in Figure 1.6, the  $\alpha$  protons on a HT coupled monomer unit (**b**) appear at 2.80 ppm; however, the  $\alpha$  protons at the chain ends (**b'**) are shifted upfield in the range of 2.4-2.65 ppm due to the different chemical environment brought on by the end groups. The ratio of the integrated signals of **b** to **b'** yields the degree of polymerization (DP). For the allyl-terminated P3HT shown in Figure 1.6, the DP = 15, and corresponds to a  $M_n$  of 3,000 g/mol. MW analysis via  $^1\text{H}$ -NMR can be complicated when the repeat unit and end-group signals overlap, or if the P3HT end groups are not exclusively allyl/Br terminated (i.e. contain high amounts of H/H, allyl/allyl, or Br/Br). For higher MW P3HTs, which in my experience  $M_n \geq 15,000$  g/mol, using  $^1\text{H}$ -NMR to calculate MW becomes less trivial as the end-group concentration becomes too low to obtain a clean signal.

### 1.4.3 MALDI-TOF Spectroscopy

The end-group composition of P3HTs synthesized in this work will be determined using Matrix Assisted Laser Desorption Ionization Time-of-Flight Mass Spectroscopy



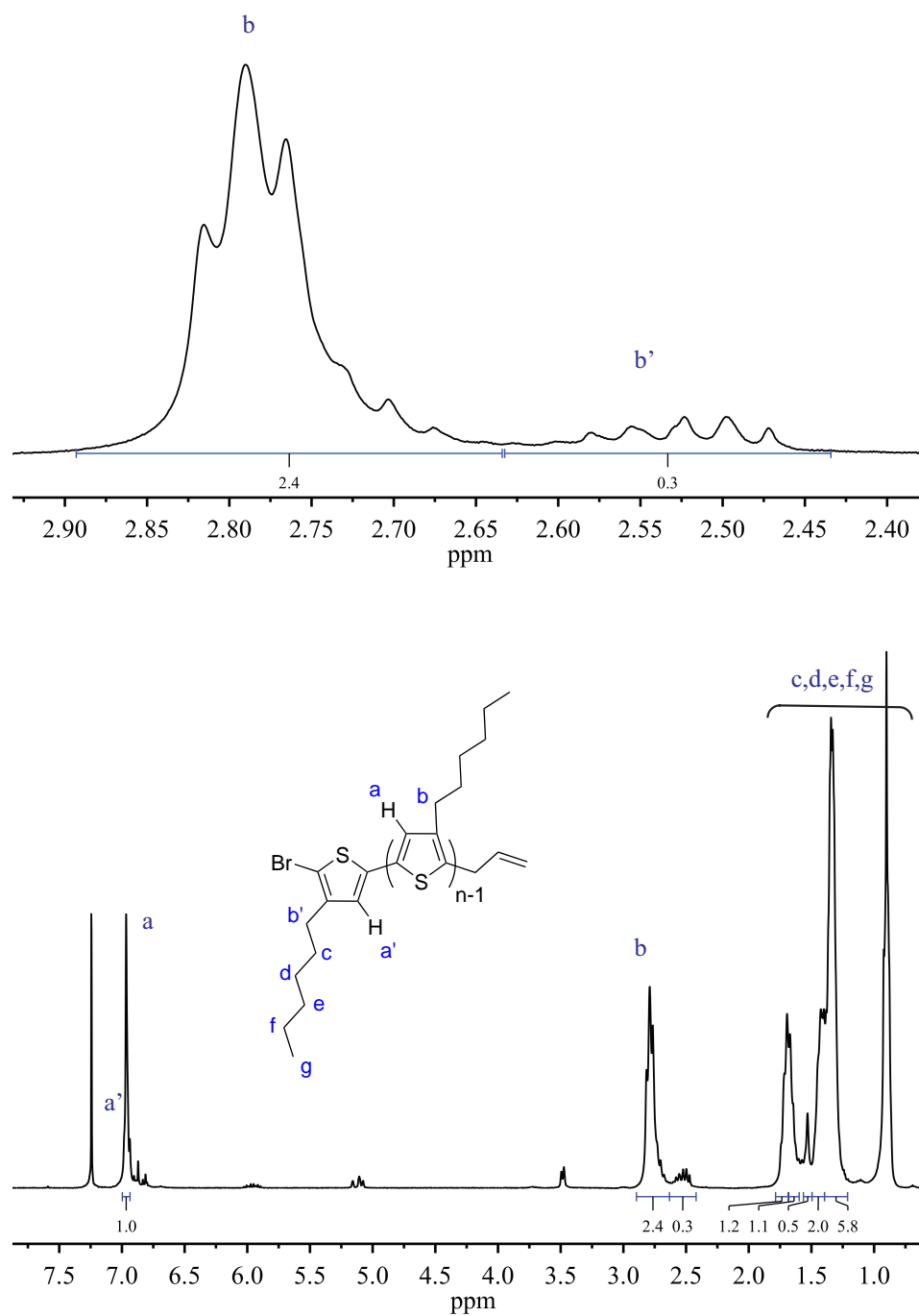


**Figure 1.6:**  $^1\text{H-NMR}$  spectrum for P3HT synthesized via KCTP and quenched with allylmagnesium bromide to yield allyl/Br end groups. The top figure is zoomed in on the methylene protons of the hexyl side chain and the bottom shows the full spectrum.

(MALDI-TOF MS). MALDI-TOF MS, a soft ionization technique, requires the use of a matrix to absorb high energy radiation that results in ionization of the analyte. Upon ionization, the analytes travel through a time-of-flight tube and are separated based on their mass-to-charge ratio, commonly denoted as  $m/z$ . Modern MALDI-TOF MS instruments are capable of achieving strong isotopic separation with high resolution, which is absolutely necessary when analyzing samples featuring end groups with masses that differ only by a few atomic mass units. Excellent resolution is reflected in the data shown in Figure 1.7, where an allyl-terminated P3HT sample features four different distributions that correspond to the pairs of end-groups present on the polymer: Specifically, the spectrum shows chains with: H/allyl, allyl/allyl, Br/allyl, and Br/Br end groups. In this work, end-group composition is determined using the intensity of the monoisotopic mass peaks as the representative peak from each distribution. The desorption/ionization processes in MALDI-TOF MS are mass dependent, meaning that the technique favors chains of lower molecular weight within the polymer sample.<sup>58,61,62</sup> Ultimately, this preference leads to lower MWs (than measured by SEC) and limits end-group analysis to polymers of relatively low MW ( $\leq 10,000$  g/mol).

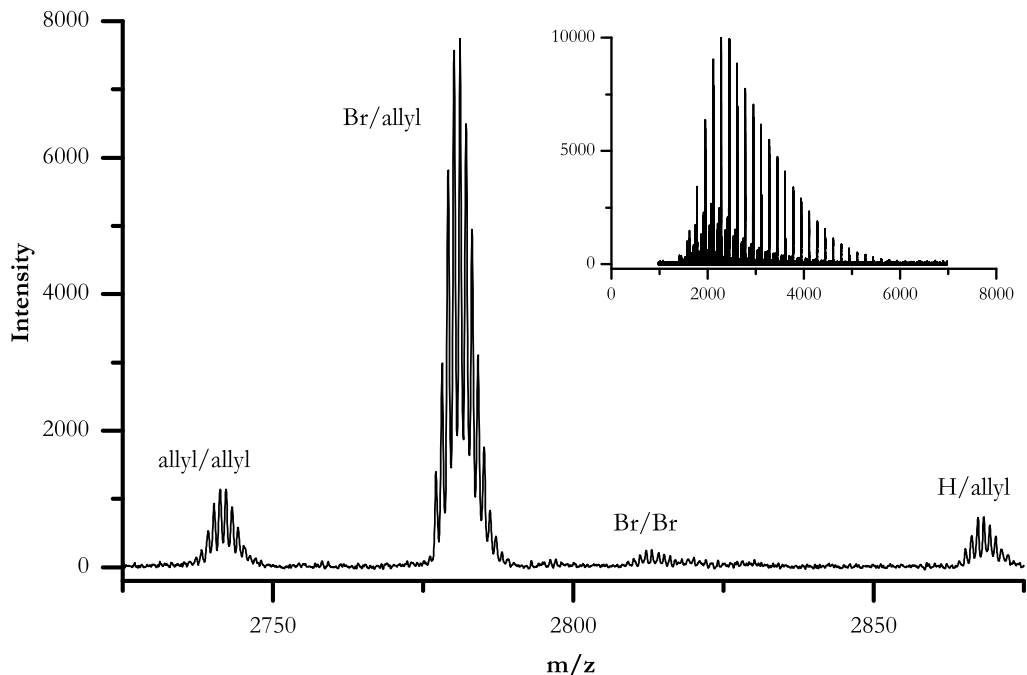


**Figure 1.7:** Example mass distributions obtained from MALDI-TOF MS measurements of allyl-terminated P3HT obtained by quenching a KCTP reaction with allyl-MgBr. The spectrum features the 16-mer region and the inset shows the full P3HT spectrum.

## 1.5 Characterization of BHJ Films

Aside from choice of materials, the electronic properties of OPV devices are sensitive to a vast array of morphological properties: donor and acceptor domain size, donor crystallinity, vertical distribution of fullerene, total film thickness, and surface roughness. Assessing these aspects of BHJ films morphology requires a range of characterization techniques tailored to the soft materials used in OPV applications. Throughout this dissertation, the performance of numerous lab-scale devices will be tested and their morphological properties will be characterized by small- and wide-angle X-ray scattering, neutron reflectivity, transmission electron microscopy, and differential scanning calorimetry.

### 1.5.1 OPV Device Performance

The power conversion efficiency (PCE), or the efficiency of the conversion of sunlight to electricity, is arguably the most important measurement in the design and implementation of new OPV materials. The PCE of OPV devices are calculated according to Equation 1.3, which is simply the ratio of that maximum power ( $P_{max}$ ) to the incoming solar illumination, which is known from a calibrated light source designed to replicate Earth’s incoming solar spectrum.

$$PCE = \frac{P_{max}}{P_{inc}} \quad (1.3)$$

The  $P_{max}$  output of OPV devices is calculated according to Equation 1.4, where the short circuit current ( $I_{SC}$ ), open circuit voltage ( $V_{OC}$ ), and fill factor (FF) are obtained from experiments in which the bias voltage is swept while the device is illuminated.

$$P_{max} = I_{SC}V_{OC}FF \quad (1.4)$$

A schematic of an I-V curve is shown in Figure 1.8. Here the darker gray box indicates the theoretical maximum power, or power output assuming no losses. This is calculated as the product of the  $V_{OC}$  and  $J_{OC}$ . The lighter gray box marks the area representing the measured maximum power,  $P_{max}$ . The theoretical power output and  $P_{max}$  are related by a scalar factor known as the fill factor (FF), which represents the charge transfer efficiency after accounting for losses across the device. There are two main mechanisms leading to the loss of charge carriers in OPVs, *geminate* and *nongeminate* recombination. Geminate recombination occurs when an electron-hole pair recombine before separating (at a DA interface) due to the strong electrostatic interactions between them. Nongeminate refers to recombination that occurs after the electron and hole have separated into free charge carriers and occurs over much longer timescales than geminate recombination. Nongeminate recombination can occur between an electron and hole that originate from different charge generation

events. The presence of impurities throughout the BHJ film can increase nongeminate recombination, and are often referred to as *trap-assisted recombination*.

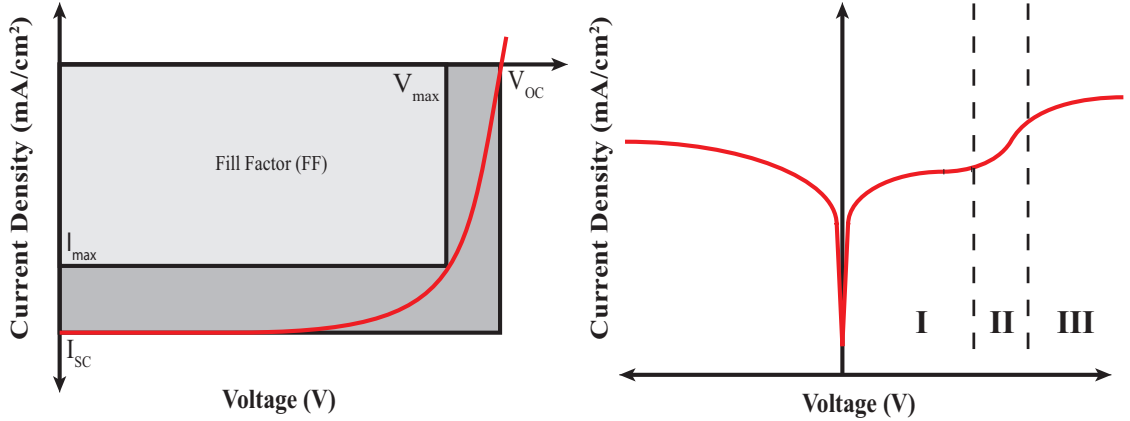


**Figure 1.8:** Example current-voltage diagram used to assess the performance of solar cells under controlled illumination (left) and dark conditions (right). Adapted from Servaites et. al.<sup>63</sup>.

Aside from seeking to maximize power output, OPV performance measurements are critical for determining why a device performs at a higher or lower efficiency. In particular, extensive information about the types of resistance governing the performance of OPV devices can be obtained from dark curve measurements.<sup>63</sup> An example dark curve for an OPV device is shown in Figure 1.8. At low voltages (region I), the J-V characteristics are primarily determined by the shunt resistance,  $R_{sh}$ , which generally occur due to manufacturing defects. Essentially, low  $R_{sh}$  values indicate that power loss is occurring due to charges taking an alternative path rather than flowing through the solar cell junction. For an ideal solar cell,  $R_{sh} = \text{inf}$ , all of the photo-generated charges would travel through the donor and acceptor materials to the electrodes. At moderate voltages (region II), the J-V characteristics are dictated by the diode characteristics of the device, or more simply how much recombination is occurring at the DA interface. At high voltages (region III), the performance is primarily driven by the series resistance,  $R_s$ . The  $R_s$  is comprised of the resistance of the metal contacts, presence of impurities, and the depth of the BHJ active layer. In

an ideal OPV device the  $R_s = 0$ . Guided by these rules of thumb, the dark curve can provide information to explain the performance of OPV devices under illuminated conditions.

### 1.5.2 Transmission Electron Microscopy

Transmission electron microscopy (TEM) is used to directly image the phase separation of donor and acceptor materials in BHJ films. For OPV materials, TEM micrographs are most commonly collected in bright-field (BF) imaging mode. In BF imaging contrast originates from incoherent and elastic scattering between the incident electrons and the Coulomb field of the nuclei within the sample.<sup>64</sup> The cross-section for BF imaging is dependent on the mass of the scattering atoms, which carries consequences that must be considered when imaging soft materials. To summarize, thinner regions or regions rich in low atomic number elements will appear as brighter, while thicker regions or those rich in heavy atoms rich in will appear darker. Since the micrograph is assumed to be a simple projection of the sample along the illumination axis, contrast arising from BF-TEM imaging can occur through differences in mass, density, and thickness. Contrast enhancement has been achieved through controlled defocusing of the TEM, however this method leads to a corresponding reduction in the maximum attainable resolution compared to in-focus imaging, and therefore, limits the quantitative evaluation of domain sizes.<sup>65</sup> Nevertheless, two materials with similar makeup and density, which is the case for P3HT and PCBM thin films, are indistinguishable in BF-TEM.

The use of energy filters is one alternative to BF-TEM that avoids the resolution issues arising from defocused imaging. In energy-filtered (EF) TEM, different materials are highlighted based on the amount of energy lost from the collision of an incoming electron with a single atom or molecule as it passes through the sample. To determine the signature of each material is accomplished through electron energy loss spectroscopy (EELS) measurements of pure films of each material in the sample.

By setting the energy filter to appropriate levels based on these EELS measurements, EF-TEM can provide high contrast images of donor and acceptor domains with sharp focus and nanometer-scale resolution. Numerous EF-TEM studies of BHJ films have reported that P3HT can be selectively illuminated using the the plasmon loss peak located at 19-20 eV and PCBM can be imaged using the peak at 30 eV, respectively.<sup>66-71</sup> An example highlighting the utility of EF-TEM on P3HT and PCBM films is shown in Figure 1.9, which depicts the contrast that arises from a control film featuring P3HT (yellow) and PCBM (blue). Because EF-TEM only captures electrons interacting with a single atom, its application is limited to relatively thin samples ( $\approx 60$  nm) so that a sufficient number of single-event electrons can be captured by the camera.

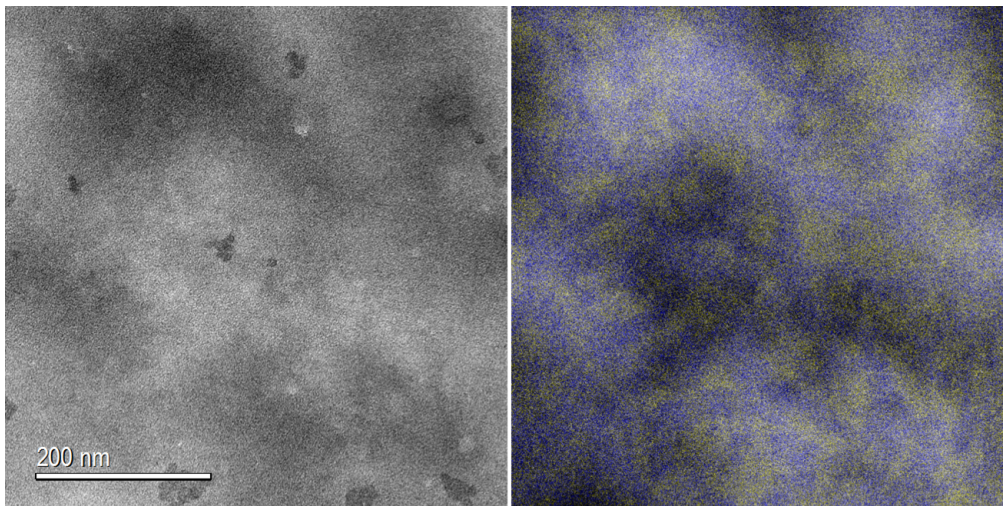


**Figure 1.9:** Unfiltered (left) and EF-TEM composition (right) micrographs of a BHJ blend. P3HT-rich regions are denoted by blue and PCBM-rich in yellow.

While classic TEM grids featuring manufactured holes are acceptable for bulk BHJ film phase behavior, these measurements fall short in determining the effect of at the substrate and air interfaces on morphology of OPVs. Capturing the morphology at these interfaces by TEM requires cross-sectioning of the film. The preparation of lamella can be accomplished using a dual beam scanning electron microscope (SEM) focused ion beam (FIB) outfitted with a nano-manipulator tool.

The nanomanipulator allows small lamella from a larger BHJ film cast on Si to be extracted. The extracted small lamella is then platinum-welded onto specially designed copper posts, which allow the film to lay "on its side", making the depth-cross-section perpendicular to the electron beam in the microscope. Lamella are extracted via the trench method, which for brevity, has been covered in more detail in Appendix A.6.<sup>72,73</sup> This technique is applied to BHJ films cast atop silicon or P3HT brush-modified substrates. The work, which is described in Chapter 2, allows vertical PCBM phase segregation across the depth of BHJ films to be examined. The cross-sectional EF-TEM images collected from these samples will be used to qualitatively assess the depth distribution of PCBM and confirm the PCBM depth profiles obtained from neutron reflectivity measurements.

### 1.5.3 Neutron Reflectometry

Probing the morphology of BHJ films is complicated by a multitude of factors, including strong optical absorption, a general lack of contrast with X-rays, and sensitivity to fabrication techniques used in electron microscopy. Neutrons offer a unique opportunity to avoid these difficulties because they scatter from atomic nuclei rather than electron shells (as in the case with X-rays). Furthermore, the short wavelengths of thermal neutrons make it possible to resolve structure at the nanoscale. In neutron reflectivity (NR), a collimated beam of neutrons illuminates a sample at a shallow angle while a detector records the intensity of reflected neutrons at the same shallow angle. The intensity of these reflected neutrons are measured as a function of the momentum transfer vector,  $q_z$ , which is a function of the incident angle ( $\theta_s$ ) and neutron wavelength ( $\lambda$ ), as shown in Equation 1.5.

$$q_z = \frac{4\pi}{\lambda} \sin \theta \quad (1.5)$$

Aside from variations in neutron wavelength and scattering angle, changes in the reflected intensity also originate from differences in scattering length density (SLD)



as a function of depth within the sample. For morphological studies of BHJ films, these changes in intensity are characteristic of differences in PCBM volume fraction through the depth of the film. This arises due to the inherent contrast resulting from differences in SLD between the P3HT- (H rich,  $0.68 \times 10^{-6} \text{ \AA}^{-2}$ ) and PCBM-containing (H deficient,  $4.3 \times 10^{-6} \text{ \AA}^{-2}$ ) regions within the film. The SLDs reported for P3HT and PCBM vary slightly between sources primarily due to discrepancies in the bulk density of the two materials. However the values used here represent common estimates used in similar BHJ morphological studies.

By assuming the film's laterally-averaged concentration to be constant and only a function of depth, a model based on the First Born Approximation can be used to describe the collected reflectivity profiles. This model is shown mathematically in Equation 1.6, where  $\rho$  is the SLD at a particular depth.

$$R(Q) = \frac{16\pi^2}{q^2} \sum_{n=1}^{\infty} \left| \int_{-\infty}^{\infty} [\rho_{n+1}(z) - \rho_n(z)] e^{-iqz} dz \right|^2 \quad (1.6)$$

The data was fit using an excel spreadsheet based on an exact optical treatment of Parratt's recursion formula, features within the collected reflectivity profiles are replicated by the model through iterative data fitting. To simplify the fitting process and to physically constrain fits to realistic SLD values and thicknesses for BHJ films, a mass balance can be imposed on the model. A complete mathematical derivation of the mass balance is presented in Section A.4, and the general expression obtained is shown in Equation 1.7. In this expression,  $\mu_{PCBM}$  is the total volume fraction of PCBM in the film,  $d_n$  is the thickness of layer  $n$ , and  $\phi_n$  is the volume fraction of PCBM of layer  $n$ . Using this mass balance also requires that the density of each component be constant for each layer.

$$= \nu (d_1 + d_2 + d_3) = \phi_1 d_1 + \phi_2 d_2 + \phi_3 d_3 \quad (1.7)$$

The SLD for each layer used in the fitting software can be converted to volume fractions of PCBM,  $\phi_{PCBM}$ , by use of Equation 1.8, where the layer SLD,  $(Nb)_n$ , is based on the pure component SLD of PCBM and of P3HT, and their PCBM volume fractions,  $\phi_{PCBM}$ .

$$(Nb)_n = \phi_{PCBM}(Nb)_{PCBM} + (1 - \phi_{PCBM})(Nb)_{P3HT} \quad (1.8)$$

The constraints imposed by these relationships drastically reduce the domain space, helping to ensure that only physically realistic models are tested. Furthermore, consistency is enforced across different fitting models by preserving mass balance on samples before and after annealing treatments.

An example NR profile is shown in Figure 1.10. It reveals changes in PCBM concentration after thermal annealing. The sharp maximum at  $z \approx 1300$  nm is indicative of the SiOx layer between the Si substrate ( $z \geq 1350$  nm) and the BHJ film. Drastic segregation of PCBM to the film/ substrate interface is observed after thermal annealing, as indicated by the difference between the SLD profiles before (dashed line) and after (solid line) annealing. At the air-film interface, located at  $z \approx 200$  nm, there is a reduction in the PCBM content after thermal annealing. Although the fits are substantially different before and after thermal annealing, the integrated SLD across the domain of the BHJ film is consistent between samples due to having implemented mass balance between the two fits.

#### 1.5.4 Ellipsometry

Some of the ellipsometry measurements used to monitor film thicknesses were made using a Beaglehole Picometer Ellipsometer located at UTK. This instrument uses a NeHe laser (632.2 nm), and because of its sensitivity it is especially suited to confirm the cleanliness of the silicon substrates: The silicon oxide layer thickness after cleaning should be  $\approx 1.5$  nm. Because BHJ films tend to absorb light at this wavelength, this technique is not appropriate for measuring thick P3HT films ( $\approx$

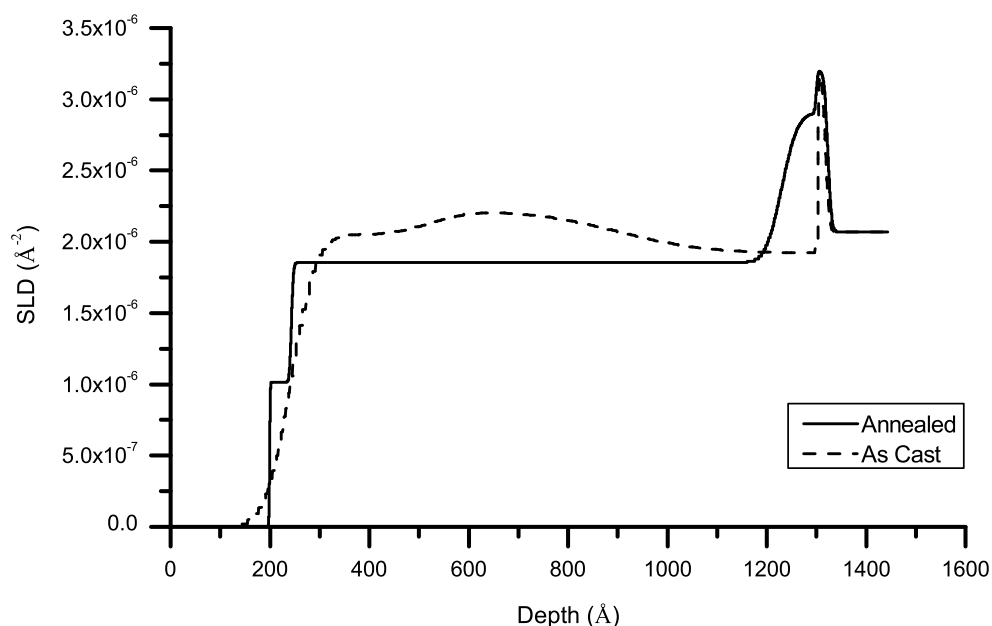


**Figure 1.10:** Representative scattering length density profile of a BHJ film cast on a brush-modified silicon substrate before (dotted line) and after (solid lines) annealing at 150 °C. The SLD at each depth is directly related to the composition of PCBM. This sample represents a case of severe PCBM aggregation at the Si substrate/film interface after annealing.

40 nm) or films containing PCBM nanoparticles. However, given the thin nature of P3HT brush layers studied in Chapter 2, the absorbance of end-grafted P3HTs is minimal and therefore it is acceptable to use this instrument to estimate the layer thickness before deposition of the BHJ film.

Thickness measurements of BHJ films by ellipsometry necessitates the use of wavelengths that are not absorbed by materials in the BHJ. For this reason the total BHJ film thicknesses will be measured using a spectroscopic ellipsometer (manufactured by J.A. Woollam Co., Inc.) that is located at the Center for Nanophase Materials Science (CNMS). Outfitted with a white light source, this instrument allows the wavelengths outside of the absorption band of the BHJ film to be selected, thereby removing effects due to absorption. For these measurements, spectroscopic scans are

performed across a range of wavelengths (700-900 nm) and at multiple angles so that Cauchy model parameters can be obtained via Equation 1.9. From my efforts, I found  $A_n = 1.7129$  and  $B_n = 0.10976$ , which are consistent with other reports on similar P3HT:PCBM films.<sup>74</sup> These parameters,  $A_n$  and  $B_n$ , can be used to calculate the refractive index,  $\eta$  as a function of wavelength by using the Cauchy relationship shown in Equation 1.9.

$$\eta = A + \frac{B}{\lambda^2} \quad (1.9)$$

The refractive index values are then used to iteratively fit the ellipsometry data using a slab layer model. Spectroscopic ellipsometry has been particularly useful in studies of BHJ films, where measured BHJ film thicknesses are used in the fitting of NR data.

### 1.5.5 Differential Scanning Calorimetry

One method that has proven useful for measuring the presence and extent of thermal processes, such as crystallization or melting in BHJ films, is differential scanning calorimetry (DSC). In a DSC experiment, a mass of BHJ film material is heated at a controlled rate, and any changes in the energy required to heat the sample at a constant rate is recorded. These changes in energy (heat) flow indicate the presence of endothermic or exothermic processes occurring within the sample. For BHJ blends, DSC has seen frequent use in measuring the amount of crystalline P3HT with changes in molecular properties or in the presence of additives.<sup>56,75-81</sup> The percent crystallinity of a P3HT sample can be calculated by dividing the measured enthalpy of melting ( $\Delta H_m$ ) by that of a theoretical crystal ( $\Delta H_f$ ), as shown in Equation 1.10.

$$W_c = \frac{\Delta H_m}{\Delta H_f} \quad (1.10)$$

The exact value of  $\Delta H_f$  is a point of contention, as indicated by the range of values summarized in Table 1.1. This discrepancy arises due to the different forms that P3HT crystals can take, as well as sensitivity of the measurements to sample

preparation and particular instruments used. I have favored the use of 37 or 43 J g<sup>-1</sup> as an appropriate estimate of  $\Delta H_f$ , and this value will be used in this dissertation. For P3HT crystallinity measurements comparing similar films, as in different loading levels of the same additive, the choice of  $\Delta H_f$  makes little difference because it uniformly changes the results by a scalar quantity.

**Table 1.1:** Reported  $\Delta H_f$  values used for P3HT. The \* values identified by an asterisk indicate that the authors found different values for different P3HT crystal form factors.

$\Delta H_f$ [J g <sup>-1</sup> ]	Authors
37	Pascui <sup>82</sup>
43	Remy <sup>83</sup>
50	Snyder <sup>81</sup>
99	Malik <sup>84</sup>
37-50*	Lee and Dadmun <sup>85</sup>
39-99*	Koch <sup>86,87</sup>

Aside from crystallization studies, DSC is also useful for its ability to estimate Flory-Huggins interaction parameters,  $\chi$ , between two materials via melting point depression. The melting point depression due to mixing of a crystalline polymer with PCBM is described mathematically by Equation 1.11, where the subscript  $s$  denotes the diluent (PCBM) and  $m$  refers to the crystalline P3HT,  $\phi_s$  is the volume fraction of PCBM,  $\Delta H_f$  is the heat of fusion of the P3HT,  $\nu_s$  is the molar volume of PCBM (607 cm<sup>3</sup>/mol)<sup>88</sup>, and  $\nu_m$  is the monomer repeat unit volume of P3HT (151 cm<sup>3</sup>/mol)<sup>89</sup>, and R is the ideal gas constant.

$$\frac{1}{T_m} - \frac{1}{T_m^0} = \frac{R}{\Delta H_f} \frac{\nu_m}{\nu_s} [\phi_s - \chi\phi_s^2] \quad (1.11)$$

Fitting Equation 1.11 to collected melting point data by using  $\chi$  as the only adjustable parameter will yield the optimum value for the measured sample set.

Flory Huggins analysis has been used to investigate the crystallization processes that drive the separation of PCBM in BHJ blends featuring regioregular and

regiorandom P3HTs.<sup>90</sup> A similar technique has been used to show that P3HT miscibility with PCBM decreases as MW is increased.<sup>75</sup> In both of these studies,  $\chi$  values ranging from 0.4–0.9 obtained for P3HTs depending on MW. In these dissertation studies, the measurement of Flory-Huggins interaction parameters will be particularly useful in Chapter 4, where DSC experiments are used to determine if capping P3HTs with porphyrins changes their behavior in comparison to allyl-terminated P3HTs.

## 1.6 Research Objectives

The overall goal of this dissertation research is to explore strategies designed to influence the morphology of donor-acceptor blends commonly used in the active layers of organic solar cells. These strategies will rely on the synthesis and characterization of different variations of poly(3-hexylthiophene)s (P3HTs) designed to influence the morphology of BHJ film through distinctly different mechanisms. The scope of this research includes:

- I. Grafting of polymer chains directly to the anode surface as an interfacial buffer layer.
- II. Using low molecular weight P3HTs as additives to form bi-disperse donor polymer blends.
- III. Design and synthesis of porphyrin-functionalized P3HTs chosen to modify self assembly at donor-acceptor interfaces.

These strategies are enabled by my ability to fine-tune synthetic parameters, as well as to perform the necessary characterizations that are used to describe the resulting behavior of the films. Although OPV device performance is an immediate motivating factor, it is emphasized that the utility of this research lies in its focus on understanding the morphological development of polymer-nanoparticle systems.

It is anticipated that the results from this body of work will provide insight into new methods for controlling thin film morphology through controllable, yet scalable chemical processes that are applicable to more sophisticated state-of-the-art materials. Lastly, while this work emphasizes improving OPV devices, the results will provide fundamental insight for controlling the morphology of other polymer-nanoparticle systems such as nanocomposites, self-healing materials, and tags used in imaging systems.

In Chapter 2, a detailed morphological study is performed on surface-grafted P3HTs as an anode buffer layer replacement material. The synthesis and characterization of these end-functionalized P3HTs is presented along with the grafting-to process used to accomplish the attachment of the P3HTs to Si substrates. Properties of these brush layers such as thickness, roughness, and optical absorption properties are analyzed by ellipsometry, atomic force microscopy, and UV-Vis spectroscopy, respectively. The grafting density of these layers is controlled by thermal annealing at temperatures above and below the glass transition temperature of P3HT. This is shown to affect the behavior of these layers and their impact on BHJ morphology. The effect of these tethered P3HT layers is shown to have a significant impact on the morphology of BHJ films after thermal annealing at 150 °C, as revealed by NR and cross-section EF-TEM.

In Chapter 3, the impact of low MW P3HTs as additives are explored as a means to influence BHJ morphology by providing thermodynamic competition with PCBM nanoparticles. The synthesis and characterization of these P3HTs is presented, and their incorporation into BHJ films at different loading levels is investigated. The effects of the P3HT additives on these films is revealed using NR, x-ray scattering, EF-TEM, and device performance studies. It is noteworthy that all additive-modified films produced an increase in device performance at different loading levels. Interestingly, for two of the additives, the performance increases coincide with the maximum loading limit achievable before inducing a coarsening of the BHJ film morphology. This work was performed alongside Peta-scale molecular dynamics

simulations, which complements the discussion of the underlying mechanisms driving these increases in device performance.

Chapter 4 extends the investigation of BHJ additives to porphyrin-capped P3HTs, which are designed to control fullerene segregation by taking advantage of strong  $\pi-\pi$  interactions between porphyrin macrocycle and fullerene nanoparticles. The synthesis of the end-functional P3HTs and mono-hydroxy porphyrins are presented along with extensive molecular characterization that confirm successful coupling between the P3HT and the porphyrin macrocycle. These additives are integrated into BHJ films at various loading levels, and their impact on BHJ morphology is explored using UV-Vis spectroscopy, fluorescence spectroscopy, AFM, EF-TEM, and device performance studies.

Lastly, Chapter 5 summarizes the main results from this dissertation work and their impact on the field of OPVs. Also included is a brief discussion on future veins of research that would provide logical and worthwhile extensions of my work.

Following these chapters and the references are two appendices. Non-obvious or novel derivations and experimental procedures are presented in Appendix A. The presentation of data that is secondary to project goals or the main discussions will be reserved for Appendix B. Listed figures will be summarized in the Supporting Information sections of Chapters 2 through 4.



## Chapter 2

# End-Tethered P3HTs as Anode Buffer Layer Replacement

## 2.1 Abstract

Electrode buffer layers play an integral role in organic electronic devices as they impart electronic benefits critical for efficient operation while simultaneously mediating interactions at the electrode/film interface. In this chapter, the morphological impact of end-tethered poly(3-hexylthiophene) (P3HT) are investigated as a means to alter the morphology of thermally-annealed bulk heterojunction (BHJ) films comprising a blend of P3HT and [6,6]-phenyl-C61-butyric acid methyl ester fullerenes (PCBM) commonly used in organic photovoltaic devices. Control over the grafting density of end-tethered P3HTs is afforded through thermal annealing at different temperatures during the surface grafting process. Neutron reflectometry and imaging using energy-filtered transmission electron microscopy (EF-TEM) reveal that BHJ films applied via spin-casting atop these interfacial layers exhibit substantial reductions in the PCBM volume fraction near the substrate-film interface. However, upon thermal annealing, PCBM segregation to the substrate-film interface increases in systems having end-tethered P3HT chains.

## 2.2 Introduction

In a conventional OPV structure, the device would be constructed with a transparent anode to allow photons to illuminate the BHJ film. One of the best performing transparent anode materials to date, ITO, is renowned for its high conductivity and ease of application to a variety of substrates. Because ITO has a work function of approximately 4.7 eV, it is not ohmically aligned with the HOMO of donor polymers or the LUMO of fullerene-based acceptors.<sup>91</sup> This misalignment enables ITO to collect both positive (holes) and negative (electrons) charge carriers, which in practice, can lead to reductions in the collected current and open-circuit voltage,  $V_{oc}$ .<sup>92,93</sup> Inspired

by performance increases of organic light-emitting diodes, the addition of specially-designed anode buffer layers has been shown to alleviate many issues that challenge the use of ITO as an anode in OPV devices.<sup>13</sup>

There is a growing body of work suggesting that anode and cathode interfaces play a significant role in the efficiency and stability of fullerene-based OPVs.<sup>31,32,94</sup> Buffer layer materials are essential ingredients, and they must be chosen carefully so that they satisfy physical and electronic demands while also providing the electronic bias needed to direct the flow of electrons and holes within the device.<sup>12,14,95-97</sup> To improve or maximize performance, ideal ABLs should:

1. Provide ohmic contact with the donor material without increasing the series resistance of the device;
2. Transport holes to the anode while blocking electrons;
3. Be transparent in conventional device configurations; and
4. Remain chemically stable and non reactive toward BHJ materials, including during UV radiation exposure.

The ability to efficiently block electrons and transport holes is perhaps the most important property, as otherwise reductions in the  $V_{oc}$  occur along with increasing rates of nongeminate recombination at the anode.<sup>12,14,95-97</sup> BHJ morphology is consistently reported to be sensitive to the surface energy of the substrate and nature of the processing, for example, before or after deposition of the top electrode.<sup>29,31-35,98,99</sup> Therefore, buffer layer materials also provide an opportunity to influence the BHJ morphology at the electrode/BHJ film interface.

A mixture of poly(3,4-ethylenedioxythiophene) and polystyrene sulfonate (PEDOT:PSS) is the most widely used ABL material for P3HT-PCBM BHJs. Electronically, PEDOT:PSS is an ideal ABL in OPV devices because it is hole-selective and features an appropriate band gap for use with a range of donor-type polymers.<sup>65,100</sup> PEDOT:PSS films have been reported to relieve jagged features on the surface of

ITO, which otherwise cause superficial spikes in the work function of ITO.<sup>101–103</sup> From a morphological perspective, PEDOT:PSS ABLs increase P3HT crystallization parallel to the substrate, thereby increasing hole conductivity and forming a natural filter that discourages PCBM migration to the anode.<sup>22</sup> Regardless of these benefits, PEDOT:PSS buffer layers have major drawbacks that limit their maximum performance and lifetime. First, the electron-blocking potential of PEDOT:PSS is lower than that of many other materials, which suggests there is room for improvement.<sup>104–107</sup> Second, the acidity of the PEDOT:PSS dispersion leeches indium from the ITO contact and enables various UV- catalyzed degradation pathways in the BHJ materials.<sup>98,99,104,105,108–113</sup> This problem is compounded by the hygroscopic nature of PEDOT:PSS, which leads to water retention from casting and moisture absorption from the atmosphere.<sup>114</sup> The contaminant by water has been repeatedly linked to UV-induced device degradation pathways that decrease the performance and operating lifetime of devices.<sup>114–120</sup>

Addressing the aforementioned chemical, electronic, and morphological properties in the development of new ABL materials provides an opportunity to improve cell stability and, as a result, cross a critical performance barrier currently facing OPV technology. To this end, many concepts ranging from polymers, block copolymers, self-assembled monolayers (SAMs), and inorganic buffer layers have been the subject of numerous investigations and are reviewed in-full elsewhere.<sup>13</sup> This increase in research has reinforced the importance of their charge-selective properties and also highlighted buffer layer attributes that affect OPV device performance. For example, plasmonic effects lead to an increase in film absorption and an increase in device current.<sup>121,122</sup> Self-assembled monolayers have been used to induce dipole effects at the anode interface, and these surface dipoles have led to substantial gains in hole transport.<sup>123–127</sup> These layers also modify the wettability of the surface, therefore, influencing the as-cast and annealed BHJ film morphology. In short, despite the astounding number of efforts to outperform PEDOT:PSS as the champion buffer layer, there remains a significant need for buffer layers that meet the OPV device

electronic demands while enhancing long-term stability and retaining their solution-processible nature.

Arrays of density grafted, end-tethered polymer chains, so-called "polymer brushes", comprised of conjugated polymers are an interesting concept as a buffer layer, as they present an opportunity to modify electrode surface properties and affect morphology while establishing a barrier layer. The covalent attachment of the chains to the electrode provide a robust linkage that makes the interfacial layer amenable to a range of doping or synthetic modification strategies that tune electronic properties or facilitate charge extraction, thus helping these scaffolds meet the demands of traditional buffer layers. To date, there are only a few reports investigating polymer brushes as buffer layers for BHJ OPVs. Brush layers of poly(triphenylamine acrylate) were shown to be three times more conductive to hole transport than analogous untreated films; however, OPV device performance was not reported.<sup>128</sup> Previous investigations of BHJs utilizing end-tethered P3HTs (ET-P3HTs) as an ABL demonstrated an increase in the short-circuit current that was overshadowed by a decrease in the open-circuit voltage, resulting in power conversion efficiencies of 2.27%, which is on par with control devices fabricated with a PEDOT:PSS ABL.<sup>57</sup> Despite the demonstration of the potential to enhance device properties, that work lacked an investigation of the impact of those P3HT buffer layers on BHJ morphology. This gap is addressed in this chapter of my dissertation.

This investigation is accomplished by primarily using NR and EF-TEM to investigate BHJ film morphology. NR is especially well-suited to studying conjugated polymer/fullerene BHJ blend systems due to the substantial difference in hydrogen content between the two components. This provides contrast from the inherent differences in neutron scattering density. NR measurements suggest a substantial change in the distribution of PCBM through the depth of the film. Additional insight into film morphology is obtained through cross-sectional energy-filtered transmission electron microscopy (EF-TEM), which corroborates depth-dependent distribution

models and PCBM segregation to interfaces that is the basis of the models used to fit the NR data.

## 2.3 Results & Discussion

A schematic of the ET-P3HT fabrication process is presented in Figure 2.1. Allyl-terminated P3HT (allyl-P3HT) was synthesized and characterized to confirm MW and ensure appropriate end-group composition. Purified polymer molecular weight was measured as  $M_n = 5,700$  g/mol with a PDI ( $\text{Đ}$ ) = 1.13. By  $^1\text{H-NMR}$ , the measured DP = 15, which corresponds to a  $M_n$  of 3,000 g/mol. From MALDI analysis (described in Appendix A.5), P3HTs were obtained bearing 90% mono-allyl, 3% di-allyl, and 7% Br/Br end-groups. Having a high composition of mono-allyl end-groups is paramount to ensuring sufficient chains to graft to the substrate surface (anode). These allyl-P3HTs were functionalized with chlorosilane moieties via hydrosilylation of the allyl double bond. After casting onto piranha-cleaned substrates, films were annealed at 120, 150, or 210 °C under vacuum for 24 h to facilitate P3HT attachment by reaction with surface hydroxyl groups. The different annealing temperatures are explored to determine if the extent of P3HT grafting, or grafting density, can be control with thermal annealing processes by providing mobility to the P3HT chains that increase the chance of migration to and reaction at the substrate.

In practice, the grafting density,  $\sigma$  (chains/nm<sup>2</sup>), is calculated using Equation 2.1, where  $t$  is the layer thickness,  $N$  is Avagadros number,  $\rho$  is the bulk polymer mass density, and MW is the number-average molecular weight.

$$\sigma = \frac{\rho t N_A}{MW} \quad (2.1)$$

NR and ellipsometry were both used to determine the thickness of the ET-P3HT layers used to calculate the grafting density. Ellipsometry measurements of the ET-P3HT films were recorded at multiple points on the surface. Reflectivity data for

the P3HT brushes is shown in Figure 2.2 in  $R$  versus  $q$  format. Each of these data sets exhibit steep drops in reflectivity from the critical edge at  $q \approx 0.01 \text{ \AA}^{-1}$  arising from the lower SLD of P3HT (compared to the Si substrate). The absence of Keissig fringes and the broad, drawn-out profile of the data indicate that the brush layers are thin. The thickness of the P3HT brush layers annealed at different temperatures corresponds to the global minimum that appears in each data set around  $q \approx 0.04 \text{ \AA}^{-1}$ . Each of the reflectivity curves are well-fit by a single layer model characterized by a thickness,  $t$ , and an interfacial roughness,  $\sigma_R$ , describing the film/air interface. Values of the thickness and roughness of each ET-P3HT brush are presented in Table 2.1, along with brush thickness determined by ellipsometry,  $t_{elli}$ , which are the average of thicknesses measured at multiple points on the surface. Because the majority of the 50 mm diameter wafer is illuminated by the neutron beam, the agreement between the thicknesses determined by NR and ellipsometry suggest that chains are uniformly grafted across the film.

The low grafting densities of these films can be attributed to the macromolecular size and rigidity of the conjugated thiophene backbone. For comparison, more flexible poly(glycidyl methacrylate) chains of 5 kDa achieve grafting densities of approximately 0.6-0.9 chains/nm<sup>2</sup>.<sup>129</sup> To assess whether these ET-P3HTs adopt a

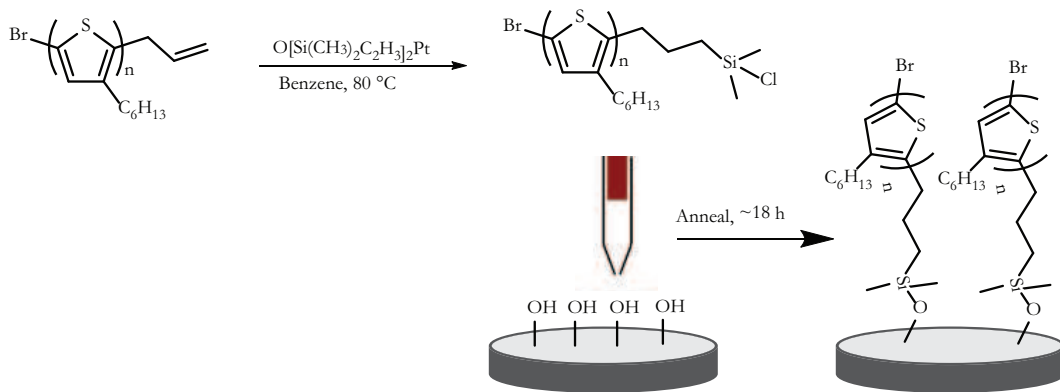


**Figure 2.1:** Schematic showing the hydrosilylation of allyl-P3HTs and the subsequent grafting of these chains to silicon wafers having native hydroxyl groups.

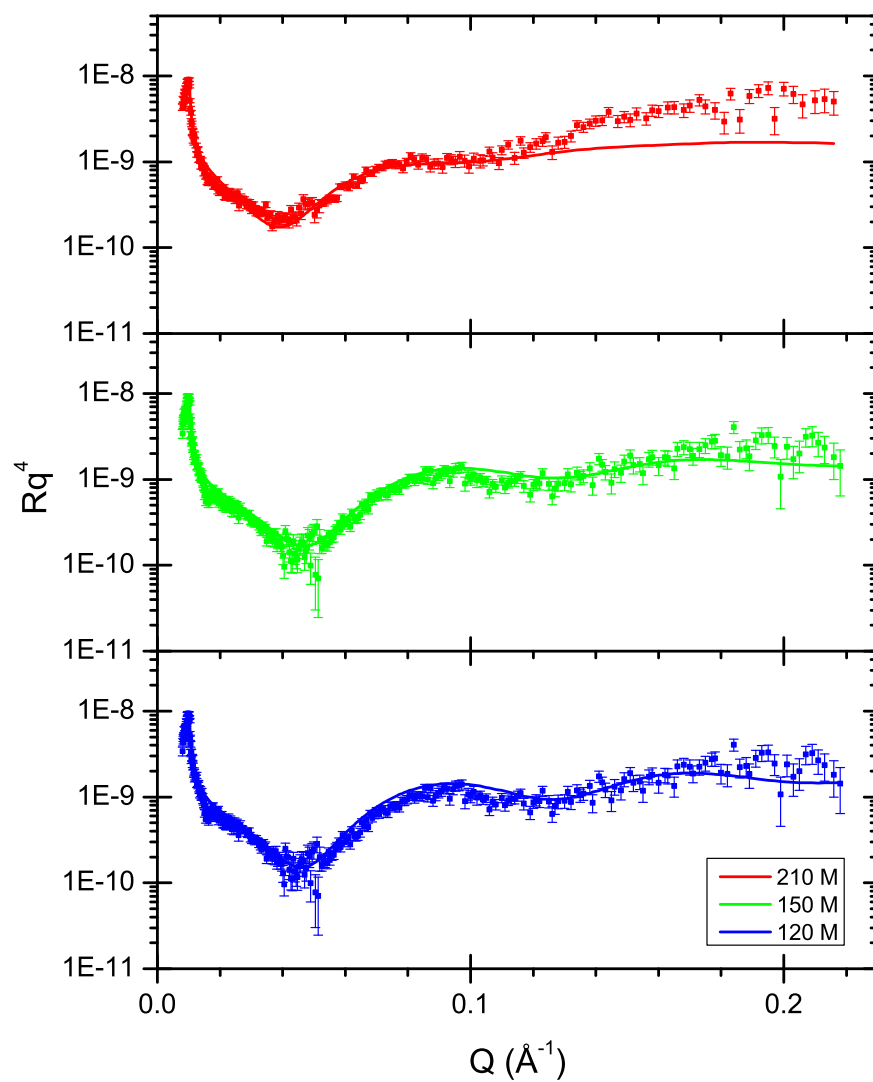


**Figure 2.2:** NR data (data points) and applied single-layer fits (lines) for end-tethered P3HT layers annealed at 120 (blue), 150, (green), and 210 °C (red)



brush-like conformation, the parameter of  $d/2R_g$  is calculated, which compares one-half the distance between grafting points of chain tethering,  $d/2$ , to the radius of gyration,  $R_g$ . End-tethered flexible polymers adopt a crowded upright orientation that qualifies as a polymer brush when  $d/2R_g \leq 1$ .<sup>130,131</sup> The distance between grafting points,  $d$ , is calculated using Equation 2.2.

$$d = 2(\pi\sigma)^{3/5} \tag{2.2}$$

The  $R_g$  of each polymer is calculated using Equation 2.3, in which  $b$  is the statistical segment length and  $N$  is the number of monomer repeat units along the chain.

$$R_g = bN^{3/5} \tag{2.3}$$

For P3HT,  $b$  has previously been estimated to be  $\approx 0.36$  nm, resulting in an  $R_g$  of 2.99 nm for the P3HTs used in this study.<sup>57,132</sup> The values of  $d$  and  $d/2R_g$  are summarized in Table 2.1. Although P3HTs are not typically thought of as flexible polymers, these  $d/2R_g$  values suggest that these ET-P3HTs adopt a crowded brush-like conformation when grafted to the silicon surface.<sup>133</sup> The relatively high grafting densities can be attributed to the extra mobility afforded by the thermally annealed grafting process, which alleviate excluded volume interactions. The low  $\sigma_R$  values are consistent with values previously determined using atomic force microscopy measurements, and they suggest the film is both uniform and smooth.<sup>57</sup>

**Table 2.1:** Height and grafting densities of end-tethered P3HT chains as calculated by Eq. 2.1 where MW= 3,000 g/mol.

Sample	Ellipsometry	Reflectometry		$\sigma$	d	$d/2R_g$
	$t_{elli}(nm)$	$t_{NR}(nm)$	$\sigma_R(nm)$	(chains/nm <sup>2</sup> )	nm	
<b>120</b>	4.1	5.0	4.5	1.10	4.22	0.26
<b>150</b>	7.6	7.3	2.5	1.61	5.29	0.21
<b>210</b>	10.4	8.5	3.5	2.20	6.37	0.20

The NR data for the “as-cast” BHJ films cast atop P3HT brushes annealed at 120 °C, 150 °C, and 210 °C, as well as a control sample in which no brush was applied to the silicon wafer are shown in Figure 2.3. The models used to interpret the data are presented as the solid lines. The laterally-averaged SLD profile obtained from each of the mass-balanced fits using a 3-layer model are shown as the dashed lines in Figure 2.4, where the right axis of each plot indicates the PCBM volume fraction. Despite rigorous efforts to develop accurate models for these NR profiles, it is obvious that there are features at  $q \approx 0.02 \text{ \AA}^{-1}$  in each of the BHJ films cast atop brush layers that are not well-described by the applied models. The unique feature in these films that complicates the data-fitting process is that the Keissig fringes dampen at  $q \approx 0.02 \text{ \AA}^{-1}$ , and then begin to reappear at  $q \approx 0.02 \text{ \AA}^{-1}$ . Typically the dampening of the Keissig fringes indicates a loss of structure detail within the film and the fringes do not reappear, as exhibited by the control film shown in black in Figure 2.3. On the other hand, the fact that the fringes reappear in the case of the BHJ films cast atop the P3HT brushes suggest that these “dead zones” are not caused by a lack of structure. It is possible that the temporary dampening is caused by features of the film that compromise assumptions made in the model used to fit the data, such as lateral uniformity across the surface of the film. It should be noted, however, that the films are not sufficiently rough to cause off-specular scattering features to appear in the detector images. Finally, as will be discussed in the thermally annealed NR measurements of these films, the “dead zones” disappear upon thermal annealing.

While the origin of these dead zones remain unclear at this point, there are still pieces of information that can be extracted from the data with certainty. For example, the critical edge for each BHJ film located at  $q \approx 0.01 \text{ \AA}^{-1}$  is consistently described by a model (using 1, 2, or 3 layers) containing approximately 34% by volume PCBM throughout the total BHJ film. From fitting of the Keissig fringes appearing as “short-range” oscillations in the data indicate the BHJ films are approximately 110 nm thick. While the SLD profiles for the BHJ films cast atop P3HT brush layers are

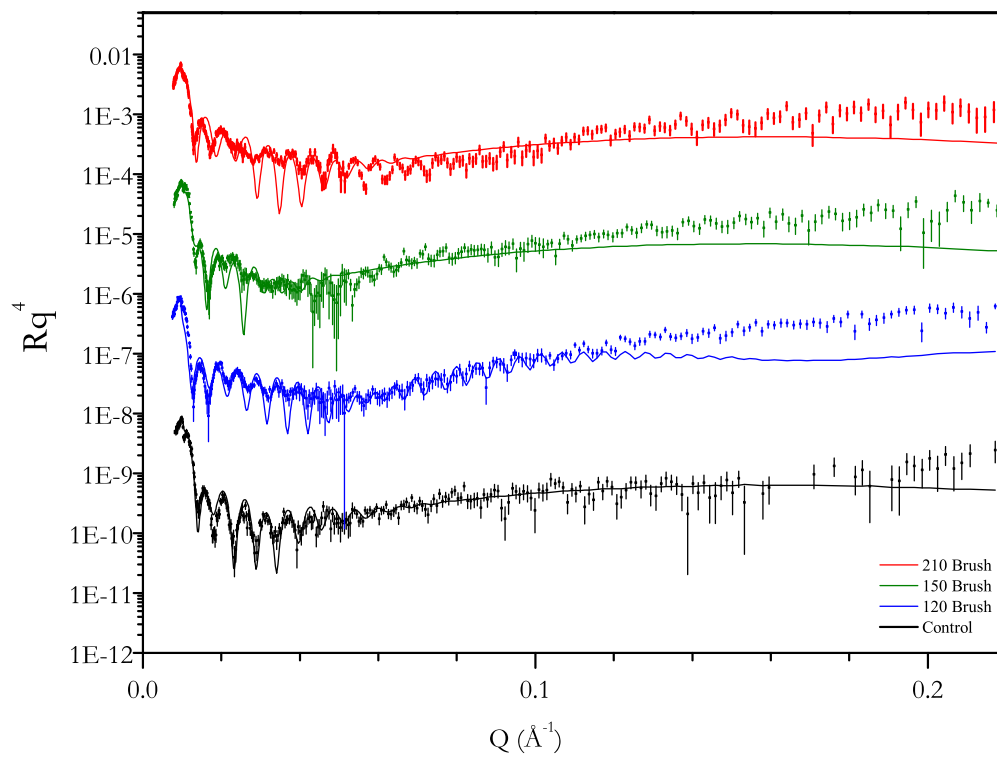


**Figure 2.3:** NR data (data points) and applied three-layer fits (lines) for BHJ films cast atop end-tethered P3HT layers annealed at 120 (blue), 150, (green), and 210 °C (red). Data are offset by 2 decades for clarity.

presented in Figure 2.4, details such as the PCBM volume fraction at the air/film or substrate/film interfaces must be considered with caution.

The control film, which lacks the “dead-zone” features, is well-described by the applied model and therefore substantially more information can be obtained from the model with confidence. The control film also requires  $\approx 34\%$  PCBM in the entire film to fit the critical edge of the collected data. Interestingly, the control film appears to be  $\approx 100$  nm thick, which is slightly thinner than the BHJ films cast atop P3HT brushes. Because the films were cast from the same *o*-chlorobenzene active layer solution, this difference in thickness is attributed to a difference in surface energy of the Si substrate compared to the P3HT-brush modified substrate. The film cast atop bare silicon oxide exhibits a PCBM-rich (37% by vol.) region near the air-film interface that gradually decreases to a minimum PCBM composition of 29% by vol. at the air-film interface.

After thermal annealing at 150 °C, the BHJ film thickness and uniformity were confirmed using spectroscopic ellipsometry measurements recorded across the diameter of each surface. Shown in Figure 2.5, these height profiles confirm that the spin-coating process results in uniform films with height differences of at most 7-10 nm measured center-to-edge. It is important to note that only the center 3 cm of a sample is illuminated by the neutron beam, thus avoiding near-edge regions where the lower thicknesses were observed. Nevertheless, the small difference between the heights measured at the center and at the edges of the samples is in strong agreement with the small rough values determined from analysis of NR data and by previously reported atomic force microscopy measurements.<sup>57</sup>

The NR profile of the BHJ films after thermal annealing at 150 °C are shown alongside their fits in Figure 2.6. As previously mentioned, the “dead-zones” present in the as-cast films are not present after thermal annealing treatments. While it is possible their disappearance is due to macro-scale rearrangement of the surface of the BHJ films, it should be noted that the annealing temperature is relatively low compared to the melting temperatures of P3HT and PCBM ( $\approx 180$  °C and

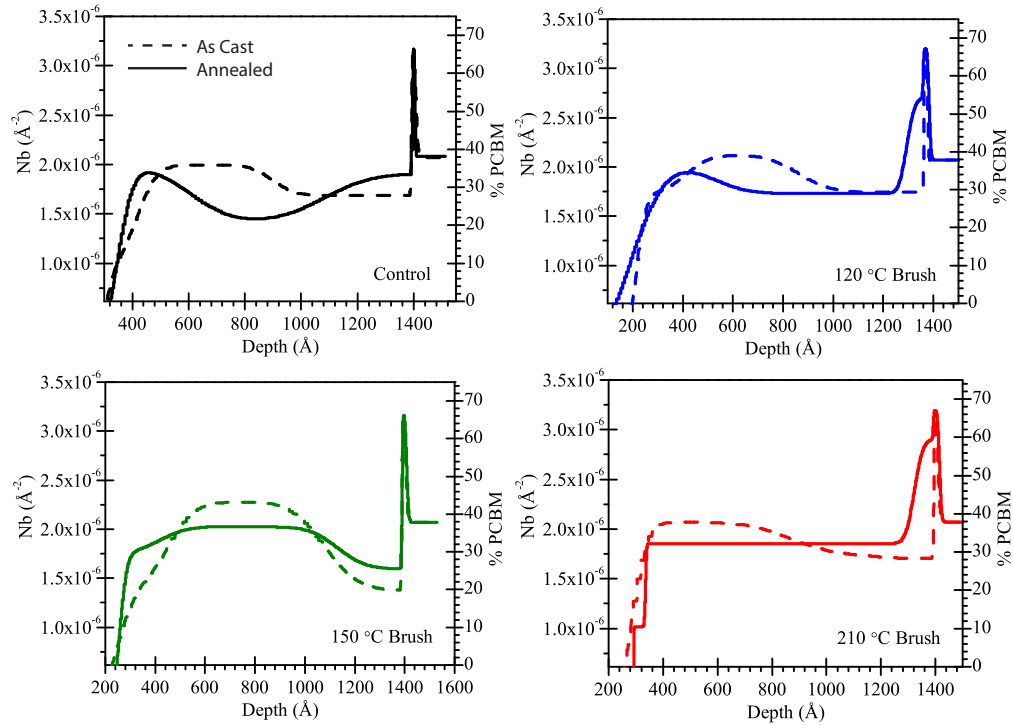


**Figure 2.4:** SLD (left axis) and volume fraction of PCBM (right axis) profiles for the as-cast (dashed) and thermally annealed (solid) BHJ films cast atop brushes annealed at 120 (blue), 150 (green), 210 °C (red); the control featuring no brush (black). The right axis corresponds to the volume fraction of PCBM. The curves have been shifted such that the SiOx/film interface lies at  $\approx 1400$  Å for ease of comparison.

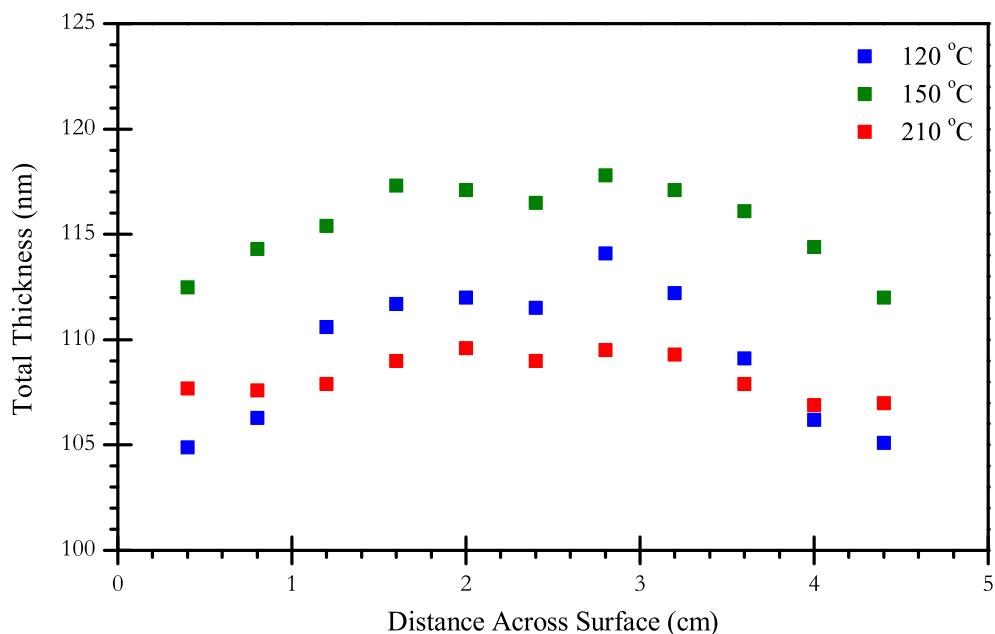


**Figure 2.5:** Spectroscopic ellipsometry measurements for thermally annealed BHJ films deposited on brushes grafted at 120 (blue), 150 (green), 210 °C (red).

280 °C, respectively<sup>75,77</sup>). As such, it is unlikely that any features large enough to compromise the uniformity of the as-cast films would disappear under such short annealing treatments. The SLD profile used to generate the fits are shown as the solid lines in Figure 2.4. One feature that is particularly apparent is the increased amplitude of the Keissig fringes compared to the as-cast samples resulting from contrast within the BHJ film. There is also an increase in the intensity of the long-range oscillations originating from thin layer(s) within the film that is indicative of a thin layer bearing a different SLD than the thicker layer.

For the BHJ film cast directly atop silicon, the SLD profile of thermally annealed film reveals PCBM segregation to the air-film and substrate-film interfaces with PCBM volume fractions reaching 37.5% and 35.5%, respectively. Between these interfaces of this “control” film, the volume fraction of PCBM slowly decreased to a minimum of 22.2%. For BHJ films cast atop P3HT brush layers, thermal annealing resulted in significant segregation of PCBM to the substrate-film interface. For the

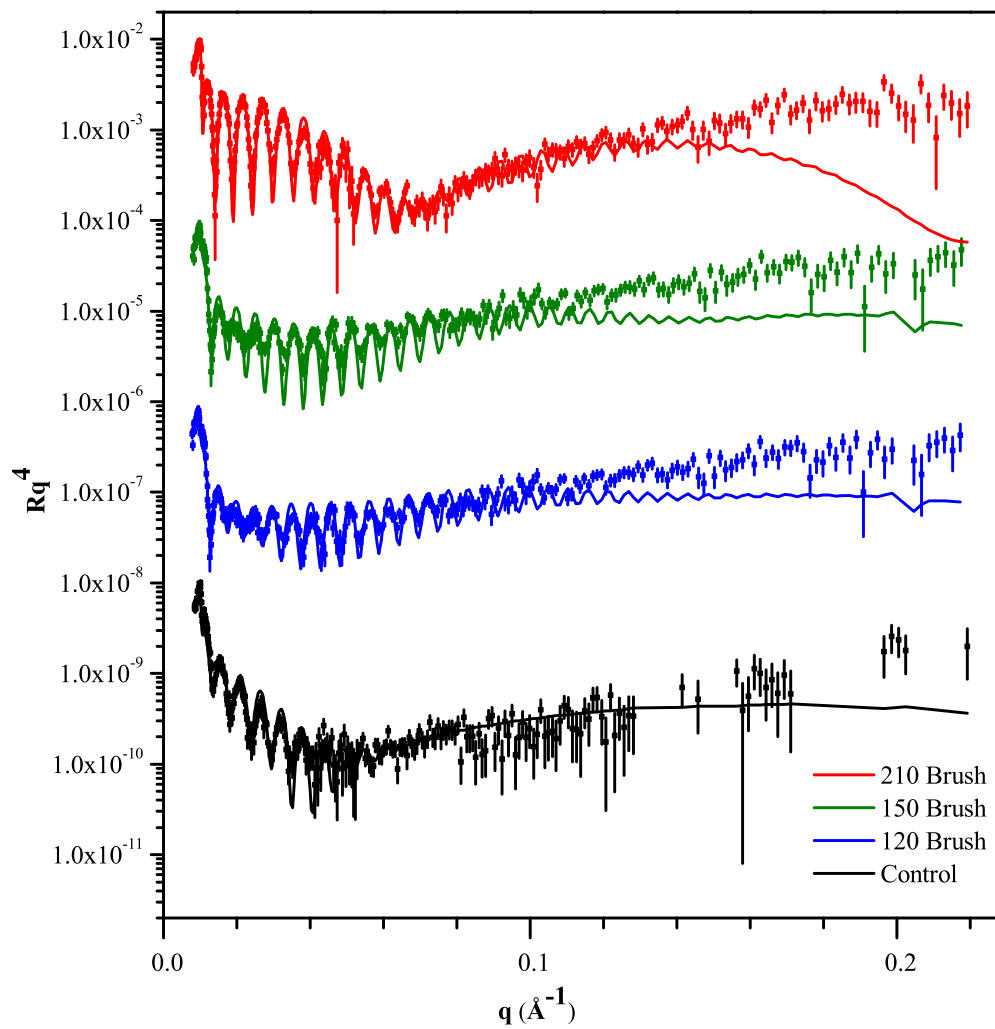


**Figure 2.6:** NR data (points) and theoretical fits (solid lines) for BHJ films thermally annealed at 150 °C atop brushes grafted at 120 (blue), 150 (green), 210 °C (red) shown alongside a control film in which a BHJ film was deposited on silicon (black).

most extreme case, film cast atop the 210 °C P3HT brush, the volume fraction of PCBM was 63% within  $\approx 7$  nm of the substrate-film interface. Above this PCBM-rich layer, the PCBM volume fraction remained constant across the depth of the BHJ film at approximately 34%. Among the brush-modified samples, the BHJ film cast atop the 150 °C brush exhibited the least amount of PCBM segregation to the substrate-film interface at 28% PCBM. For the film cast atop the 120°C brush, significant aggregation was found to both substrate-film and air-film interfaces similar to the control film. The PCBM-rich layer near the substrate-film interface reached 53% PCBM by volume and was  $\approx 7$  nm thick, which is very similar to the 5 nm thickness of the P3HT brush. The film cast atop the 120 °C brush was the only brush-modified film to feature PCBM segregation to the air-film interface, which peaked at 40% PCBM by volume at a depth of 10 nm into the film.

The annealed BHJ films cast atop 150 and 210 °C P3HT brushes require thin layers of low SLD material at the air-film interface to account for the increased reflectivity at  $q \geq 0.1 \text{ \AA}^{-1}$ . Similar features at air-film interfaces have been attributed to solvent-casting effects.<sup>19</sup> Because PCBM is more soluble than P3HT in chlorobenzene, small PCBM-rich domains form during the final drying stages of the spin casting process. Upon thermal annealing, these PCBM-rich regions diffuse into the BHJ film and result in small voids at the air-film interface that effectively lower the SLD. While this behavior is possible, the sudden decrease in SLD at the air interface observed in my results present a slightly different profile that is not well represented by fits similar to those used by Liu et al.<sup>19</sup>, particularly in the high- $q$  region of the data.

Energy-filtered transmission electron microscopy (EF-TEM) has been often used to examine the size and distribution of P3HT- and PCBM-rich domains in a variety of OPV-related studies.<sup>15,69–71,134</sup> Cross-sectional TEM samples thin enough for energy-filtered work necessitate the use of a dual beam focused ion beam (FIB)/ scanning electron microscope (SEM) to prepare (cut and extract) lamella from each sample. In this work, cross-sectional EF-TEM imaging is used to examine the spatial distribution of PCBM fullerene along the film thickness dimension, which also serves as a means



to examine the appropriateness of models used to fit the NR data of the thermally annealed samples. (And because mass balance is enforced between as-cast and annealed samples, the information also lends credence to fits of as-cast samples.) Cross-sectional EF-TEM images of lamella extracted from annealed films measured by NR are shown in Figure 2.7. The images have been colored, using yellow to denote PCBM-rich regions and blue to identify P3HT-rich domains. Each sample features a sharp illumination at the Si-film interface (diagonal feature in the upper right region of each image) that registers as P3HT (blue) due to the plasmon loss of silicon oxide at approximately 21 eV.<sup>135</sup> The control film (left image) clearly shows signs of PCBM segregation to the Si-BHJ interface as indicated by the strong yellow signal. The films coated atop brushes annealed at 120 and 150 °C (middle two images) show more P3HT at the Si-film interface due to the dense grafting of P3HT chains. This finding of relatively low PCBM concentrations at the Si substrate agrees with the results obtained by NR. On the other hand, the sample with a brush annealed at 210 °C exhibits the highest PCBM content at the Si/film interface among the four samples. This is also in agreement with the depth profile determined from fitting the NR results. There is strong agreement between the EF-TEM images and composition (SLD) profile determined from NR measurements insofar as the presence of PCBM at the film-air interface. In both techniques, significantly more PCBM is observed at the air-film interface in the control sample (no P3HT brush) as compared to the brush-modified surfaces. Despite the vast difference in sample size—images were collected across the width of  $\approx 15 \mu\text{m}$  for the EF-TEM studies versus 2 cm for the NR studies—there is strong agreement between the EF-TEM images and NR models presented herein.

Together the NR and EF-TEM results show that PCBM fullerenes tend to segregate toward the Si-interface, even when the surface is decorated with end-tethered P3HT chains. It appears that the amount of PCBM at the film/substrate interface increases as the grafting density of the P3HT chains increase; however, it should be noted that the grafting densities are modest, even though the P3HT

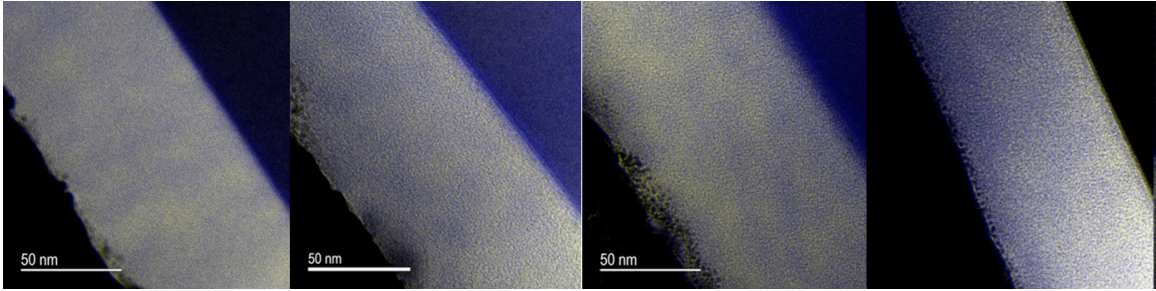


**Figure 2.7:** Cross-sectional EFTEM images of the control and each brush modified substrate annealed 120, 150, and 210 °C (from left to right). In these images the colors yellow and blue indicate PCBM and P3HT rich phases, respectively.

molecular weight is low. The volume fraction of PCBM near the substrate-film interfaces range between 53-63% PCBM depending on the brush grafting temperature. To put these results in context, these measurements are in agreement with existing reports stating that the maximum possible PCBM loading into amorphous P3HT regions is in the range of 67-75% PCBM by volume. These results derive from X-ray scattering<sup>25</sup> and other NR<sup>23,136</sup> experiments.

Interestingly, there is an absence of PCBM aggregation at the air/film interface in the 150 and 210 °C brush samples in comparison to the control film and the film deposited on the brush annealed at 120 °C. This inconsistency could arise due to the increased preference of PCBM to segregate to the substrate-film interface (rather than the air-film interface) in the presence of thicker P3HT brush layers. It is hypothesized that the propensity of PCBM to segregate to the substrate-film interface is driven by the large difference in molecular weight between the grafted P3HTs and the matrix P3HTs. A NR investigation into the miscibility of polystyrene matrix chains (ranging in size from 7-156 kg/mol) in a layer of surface-grafted deuterated PS chains revealed that the ratio of the two polymer MWs play a critical role in determining the partitioning of matrix chains in the polymer brush layer:<sup>137</sup> when the matrix MW is less than the brush MW, there is a significant entropic penalty associated with excluding the matrix chains from the brush layer. This penalty decreases, however, as the matrix MW is increased relative to the brush MW. When

the matrix MW equals or exceeds the graft chain MW, the matrix polymer chains are no longer miscible in the brush as the entropy of mixing cannot overcome the loss of conformational entropy. The end result is that the matrix polymer chains cannot mix into the grafted chains, resulting in entropic dewetting. Given that less matrix P3HT (from the BHJ blend) has segregated to the Si-film interface featuring grafted P3HTs, my results agree with this observation and trend. Because the MW of the matrix polymer is nearly 8 times larger than that of the grafted P3HT chains, there is a strong entropic penalty for the two different-sized chains to mix. It is well established that PCBM is miscible in amorphous regions of P3HT matrix; therefore, it makes sense that PCBM nanoparticles preferentially segregate to the P3HT-brush/Si interface.

## 2.4 Conclusions

These results demonstrate that donor-type polymer brushes as buffer layers provide an interesting and tunable means of influencing BHJ morphology. Despite the chemical similarity to the BHJ donor polymer, ET-P3HTs carry other thermodynamic effects that overshadow their miscibility with P3HTs in the BHJ film. Upon casting, it is shown that the P3HT brush layers decreased PCBM segregation to the substrate-film interface by as much as 20% by volume compared to the untreated surface. Furthermore, these as-cast films feature no significant accumulation of PCBM near the air-film interface.

While this PCBM distribution would seem ideal for OPV applications, this morphology was lost upon thermal annealing, during which major fullerene segregation occurred to the substrate-film interface. The severity of PCBM migration was shown to increase proportionally to the thickness of the ET-P3HT layers and the volume fractions of PCBM obtained were consistent with previously reported loading limits of PCBM into amorphous P3HT domains. The fact that PCBM segregation to the air interface was only observed for the control and the thinnest brush layer (120 °C

brush) samples might be explained by a reduction of surface energy of the substrate allowing for higher volumetric loadings of PCBM. Given the increased presence of PCBM at the substrate-film interface of the 150 and 210 °C brush samples, there appears to be weaker thermodynamic incentives for the PCBM to migrate to the air interface compared to the unmodified control and thinner brush samples.

Combined with previous work from our group, these results demonstrate that using donor-type polymer brushes as interfacial layers present an interesting opportunity to influence BHJ morphology and possibly enhance device performance.<sup>57</sup> However, the sensitivity of BHJ morphology, and therefore device performance, to thermal annealing processes has proven to lead to substantial phase separation of PCBM within the films studied herein. Perhaps morphological states more suitable for OPV device performance and lifetime can be realized using other BHJ-film processing strategies, such as solvent-vapor annealing.

## 2.5 Experimental

### 2.5.1 Synthesis of silane-terminated P3HTs

Chlorosilane-terminated P3HT chains were synthesized according to the procedures outlined in Sections A.1 and A.2. Details specific to this experiment are summarized as follows. Allyl-functional end groups were installed at the chain ends by quenching the GRIM polymerization by addition of allyl magnesium bromide. After 5 min, P3HTs were precipitated into MeOH and were purified via Soxhlet washes using methanol and acetone. The P3HT product was recovered using chloroform. Size exclusion chromatography using a Tosoh EcoSEC GPC with HPLC grade THF as the mobile phase showed the allyl-terminated P3HT to be  $M_n=5,700 \text{ g mol}^{-1}$  with  $\mathcal{D}= 1.13$ . End-group composition was confirmed using a Voyager Matrix-Assisted Laser Desorption Ionization Time of Flight Mass Spectrometer in which THF

solutions of allyl-terminated P3HT with trans-2[3-(4-tert-butylphenyl)-2-methyl-2-propenyldiene]malononitrile were used to spot the MALDI target. The P3HT sample had an end-group composition of 90% Br/allyl, 3% di-allyl, and 7% Br/Br terminated. NMR measurements performed on a Varian 300 MHz NMR using deuterated chloroform confirmed P3HT tacticity to be 91% regioregular with a molecular weight of  $M_n=3,000 \text{ g mol}^{-1}$ . Differences of a factor of two between SEC- and NMR-measured molecular weights are well-known and understood. Supporting information including SEC elugrams and MALDI and NMR spectra can be found in Figures B.1, B.2, and B.3, respectively, of Appendix B. The allyl-terminated P3HT chains were hydrosilylated according to the procedure in Section A.2. After removal of the benzene and unreacted silanes, the functionalized polymer chains were dissolved in dry chloroform (Sigma 98%) at 0.5 wt. % (P3HT/CH<sub>3</sub>Cl).

### 2.5.2 Surface Preparation and Deposition

Each surface was cleaned using piranha acid according to the procedure outlined in Section A.3. After cleaning, each surface was immediately treated by UV-ozone cleaning (NovaScan PSD Series) for a minimum of 1 h to ensure complete oxidation of groups on the surface. Ellipsometry was used to verify that the surfaces were clean, marked by having only an oxide layer with a nominal thickness of 2 nm. Silane-terminated P3HTs were deposited onto the silicon substrates by spin casting the P3HT/CH<sub>3</sub>Cl solution at 1,000 rpm for 20 s. After spin casting, the substrates were immediately transferred to an argon-flushed oven and thermally annealed under vacuum for 18-24 h at temperatures of 120, 150, or 210 °C to promote attachment of P3HT chains to the substrate. After annealing, the oven was allowed to cool to room temperature under vacuum before samples were removed. The P3HT-brush modified substrates were then immersed in chloroform and sonicated for 1 h to remove any untethered P3HT chains from the surface. After sonication, the thickness of each brush was measured by laser ellipsometry at a minimum of 3 points on the surface.

### 2.5.3 Bulk Heterojunction Film Preparation

An o-dichlorobenzene solution of PCBM and P3HT at a total solids content of 20 mg/mL and a P3HT:PCBM composition of 0.7:1 by weight was prepared in advance and stirred for 24 h at 40 °C. BHJ thin films were deposited onto each substrate utilizing a two-stage spin-coating process consisting of spinning at 400 rpm for 180 s followed by spinning at 1400 rpm for 20 s. After spin casting, samples were immediately placed under vacuum (using a vacuum oven at room temperature) for 10 min to remove any residual solvent. After NR measurements on the as-cast samples, each sample was thermally annealed under vacuum at 150 °C for 30 min to replicate the procedure used in previous investigations of P3HT-brush ABLs.<sup>57</sup>

### 2.5.4 Neutron Reflectometry

Neutron reflectivity measurements were performed at Beam Line 4b (Liquids Reflectometer) at the Spallation Neutron Source. A series of six wavelengths and 3 angles were used to measure the reflectivity transfer vector range of  $0.002 \text{ \AA}^{-1} < q < 0.22 \text{ \AA}^{-1}$ . The reflectivity profiles were fitted iteratively using *Layers* software wherein multi-layer profiles were constructed and reflectivity calculated based on the Parratt formalism to replicate all major features of the data. Layer thicknesses, interfacial roughness, and SLD were chosen based on physical constraints and to minimize error according to a goodness-of-fit test based on the normalized sum of the square of the deviation between the experimental reflectivity,  $R_{q,exp}$ , and the calculated reflectivity  $R_{q,calc}$ , as shown in Equation 2.4.

$$\chi^2 = \sum_{n=1}^{layer} \frac{(R_{q,calc} - R_{q,exp})^2}{R_{q,exp}} \quad (2.4)$$

The scattering length densities (SLDs) used in the fitting software were based on previous reports of neat films and equal  $0.68 \times 10^{-6} \text{ \AA}^{-2}$  and  $4.3 \times 10^{-6} \text{ \AA}^{-2}$  for P3HT and PCBM, respectively.<sup>33</sup> A mass balance was implemented to aid in data

interpretation and ensure consistency of the total PCBM content between as-cast and annealed NR measurements. For brevity, a complete derivation is presented in Appendix A.4.

### 2.5.5 Multiangle Ellipsometry

Multiangle ellipsometry measurements were made using a Beaglehole 1000 Picometer Ellipsometer featuring a NeHe laser (632.2 nm) outfitted with a photomultiplier detector. Measurements were made in 2° increments from 60-80°. Film thicknesses were determined by fitting a slab-layer model while assuming a constant refractive index of 1.8 for the P3HT brushes. This value was assumed based on previous spectroscopic ellipsometry measurements.<sup>138</sup> Finally, and as noted previously, the cleanliness of the silicon substrates was ensured by confirming the oxide layer thickness to be  $\approx 1.5$  nm after substrate cleaning but before deposition of the functionalized P3HTs.

### 2.5.6 Spectroscopic Ellipsometry

The total thickness of annealed BHJ films atop P3HT brushes was measured using a spectroscopic ellipsometer (J.A. Woollam Co., Inc.). The instrument was outfitted with an XLS-100 light source and an M-2000U detector. A wavelength range from 700-900 nm was used in order to avoid absorbance by the film. Scans from 65-75° at 5° increments were used to determine parameters for the Cauchy model, which describes the wavelength dependence of the refractive index,  $\lambda(\eta)$ , shown in Equation 2.5. 1.9.

$$\eta = A + \frac{B}{\lambda^2} \quad (2.5)$$

Cofitting the data yielded  $A_n = 1.7129$  and  $B_n = 0.10976$ , which is consistent with reports on similar P3HT:PCBM films.<sup>74</sup> This model was subsequently used to determine the combined thickness of the BHJ and brush layers. A total of 11 measurements were made across the center of each neutron sample ( $\approx 50$  mm

diameter) at a spacing of 0.2 cm, which approximately covers the surface area illuminated by the neutron beam in NR measurements.

### 2.5.7 Cross-Sectional Transmission Electron Microscopy

Electron micrographs were collected using a Zeiss Libra 200 MC monochromated transmission electron microscope (TEM) equipped with an energy filter. Micrographs were recorded using an accelerating voltage of 200 kV. Lamellae suitable for cross-sectional TEM imaging were prepared via the lift-out method using a Zeiss Auriga Crossbeam Ga focused ion beam (FIB) scanning electron microscope (SEM).<sup>73</sup> To prevent e-beam damage during lamella preparation, each sample was coated with a sputtered with a Au layer (approximately 50 nm thick) before being inserted into the microscope. Once in the SEM, additional protective layers of Pt were deposited atop the work area of the lamella using the Ga-ion beam. After completing the fabrication (cutting, lift out, mounting, and thinning) of the lamella, each lamella face was briefly exposed to a 20 pA beam with a 5 kV accelerating voltage as a final polishing step.<sup>139</sup> To have consistency between information obtained by NR and EF-TEM imaging, each lamella was extracted from the same surfaces used in the NR studies. Because of this, only thermally annealed samples were imaged for EF-TEM analysis. EF-TEM measurements were recorded using a slit width of 4 eV centered at either 22 eV or at 30 eV to illuminate the P3HT and PCBM phases, respectively. These images were then artificially colored blue (P3HT) and yellow (PCBM) and then superimposed, thereby highlighting any distinct differences in phase separation between P3HT and PCBM. An illustrated, step-by-step procedure of the lift-out method used to prepare these samples is presented in Section A.6.



## Chapter 3

### Low Molecular Weight P3HT

### Chains as BHJ Additives

## 3.1 Abstract

Despite tremendous progress in using additives to enhance the power conversion efficiency of organic photovoltaic devices, significant challenges remain in controlling elements of the active layer microstructure, such as the morphology at the donor-acceptor interface. At these interfaces, additives incorporating a range of functional groups have proven their potential for enhancing the morphology and electronic efficiency. In this chapter, the inclusion of low molecular weight poly(3-hexylthiophene) (low MW P3HT) additives to P3HT/fullerene active layers is investigated to identify links between additive size and loading level and the behavior in a BHJ solar cell. Low MW P3HT chains ranging from 1.6 to 8.0 kg/mol are blended with 70 kg/mol P3HT chains at loading levels ranging from 0.1-10 wt.% of the low-P3HT while keeping total mass ratio of P3HT to PCBM constant. Small-angle X-ray scattering and energy-filtered TEM reveal that domain sizes are approximately invariant at low loading levels of the low MW additives, and wide-angle X-ray scattering suggests that P3HT crystallinity is unaffected by these additives. Neutron reflectivity, and water-contact angle measurements are used to examine whether the low MW P3HTs reduce vertical phase separation in PCBM in BHJ films. Recent atomistic and MD simulations show that low MW P3HT can modify interfaces between P3HT and PCBM domains, suggesting that oligomeric P3HTs compatibilize donor/acceptor interfaces and provide a new opportunity for improving device performance and operating lifetimes.

## 3.2 Introduction

There is a significant demand to develop materials and processing strategies that avoid phase separation between donor and acceptor materials that limit lifetimes and power conversion efficiencies (PCEs) of OPV devices.<sup>28–30,32</sup> As early as 2005, it was discovered that optimal performance in single cell devices is achieved at blend compositions that are 1:1 (by wt.) P3HT:PCBM.<sup>17</sup> However, the fact that numerous studies show phase separation readily occurs suggests that the miscibility of PCBM in P3HT is far lower 50% by wt.<sup>18,20–24,75,136</sup> It is well known that crystallization of P3HT drives this phase separation: PCBM fullerenes are expunged from growing crystallites, forcing PCBM into the amorphous domains and regions near the electrode/BHJ interfaces.<sup>18,25,27</sup> One popular approach to eliminate the phase separation is to introduce a third component in the active layer that acts as a compatibilizer between P3HT and PCBM.

Historically, polymer additives have been successfully used to inhibit macrophase separation in thermoplastic blends, with loading levels up to 10% by weight.<sup>140–143</sup> In OPV devices, polymeric or copolymeric additives are generally selected or designed to increase OPV device performance by altering BHJ film morphology or by tuning the device’s electronic properties, including the work function or conductivity. A variety of polymer<sup>56,144–149</sup> and copolymer<sup>146,150–155</sup> additives have been used to improve the morphology and performance of P3HT-PCBM BHJ films. A complete summary of the additive structures and corresponding PCEs is presented Table S1 (Appendix B.3.1).

A pioneering demonstration of the ability of additives to enhance performance of BHJ solar cells was reported by Sivula and company in 2006, wherein copolymers were constructed from donor (thiophene containing) and acceptor (fullerene containing) macromonomers.<sup>153</sup> Incorporating these additives at  $\approx 17$  wt.% resulted in PCEs higher than control devices. Moreover these devices retained their higher performance even after annealing for 10 h. Because of being composed of both donor and acceptor materials, these types of block copolymers are attractive as additives because they

act as a surfactant capable of straddling donor-acceptor interfaces. Even in situations where the copolymer contains an inactive block, such as polystyrene-block-P3HT or poly(4-vinyltriphenylamine)-block-P3HT, the underlying mechanisms controlling morphology relies on miscibility of at least one of the blocks with either the donor and/or the acceptor materials of the BHJ.<sup>149,154</sup> Avoiding insulator functional groups in the chains that can reduce in electronic processes despite providing access to excellent BHJ morphological states is one challenge when using copolymer additives.<sup>56</sup> In addition to copolymers, the attachment of special functional groups to the side chains or end groups of donor polymers is another common strategy used to design BHJ additives. For P3HT-based additives in particular, pyridine, fluorine, and fullerene moieties have been included as functional groups in additives. These materials show an increase in performance.<sup>56,123,146</sup> In addition to chemical design, the loading level is another important factor governing the behavior of additives in BHJ films. A general trend exhibited in studies where additives are used is that there is an optimum loading level that maximizes performance, and any deviations from that optimal loading level result in decreases in performance. For example, optimum loading levels reported for additives used in P3HT-PCBM BHJ blends range from 1.5wt.% for poly(4-vinyltriphenylamine)-block-P3HT-blockpoly(4-vinyltriphenylamine),<sup>154</sup> 5wt.% for polystyrene-block-P3HTs,<sup>149</sup> to 8wt.% for P3HT-block-poly(4-vinylpyridine).<sup>151</sup>

From this overview of P3HT-PCBM BHJ additives, two significant traits emerge: 1) The thienyl-containing additives are generally smaller in size compared to the P3HT donor polymer used in the BHJ, and 2) PCE tends to increase at low additive loading, reach a maximum, and then decrease as additive loading level continues to increase. The fact that device performance improves despite significant differences in the chemical nature and molecular design of these additives is remarkable. Moreover, the similarity in the size of most of these additives and the sensitivity of PCE to loading level draws attention to the need to understand links between additive MW and optimum loading level. This recognition motivates questions as to whether

there is a common mechanism that drives the observed performance improvements, under what conditions they persist, and how those additives affect film morphology. Understanding these effects and trade-offs is crucial for advancing the development of OPV devices by gaining control over morphology or designing new high-performance additives that improve device performance.

Morphological investigations consistently demonstrate that electronic processes that give rise to functioning OPV devices are sensitively linked to structure at length scales spanning from the nanoscale, where molecular orientation at donor-acceptor interfaces and  $\pi$ -stacking interactions manifest, to the mesoscale, where domain connectivity and phase segregation effects come into play. For example, transmission electron microscopy (TEM) studies reveal the formation of smaller, purer crystalline phases interconnected by long polymer chains in P3HT-PCBM BHJs.<sup>156</sup> Although these crystalline domains are small, they feature increased planarity and  $\pi$ -stacking that enhance inter-chain charge transfer<sup>157</sup> at the expense of donor-acceptor interfacial area.<sup>158</sup> Increasing the MW of rrP3HT increases the conductivity of these crystalline regions until  $M_w \approx 70$  kDa, at which point the ability of long, semiflexible P3HT chains to crystallize is inhibited by chain entanglements.<sup>159</sup>

It is proposed that the addition of smaller chains of donor-type polymer to BHJ blends will provide entropic competition with similarly-sized fullerene nanoparticles within the amorphous regions of the thin film. More specifically, as matrix P3HT chains crystallize during thermal annealing, the low molecular-weight P3HTs will be expunged to the donor-acceptor interface and act as a compatibilizer between the P3HT and PCBM domains. This postulate is motivated by recent simulations that investigated low MW P3HTs as ternary additives in BHJ films of PCBM and high MW P3HT.<sup>160</sup> Their results suggest that the low MW P3HTs migrate to the interfacial area separating domains of high MW P3HTs and PCBM as illustrated in Figure 3.1, where the high MW P3HT, low MW P3HT, and PCBM are depicted as red, blue, and gray, respectively. This behavior is attributed to the smaller size of

the P3HT additives, which are shorter than the persistence length of P3HT and are, therefore, far less susceptible to intra-chain entanglements.

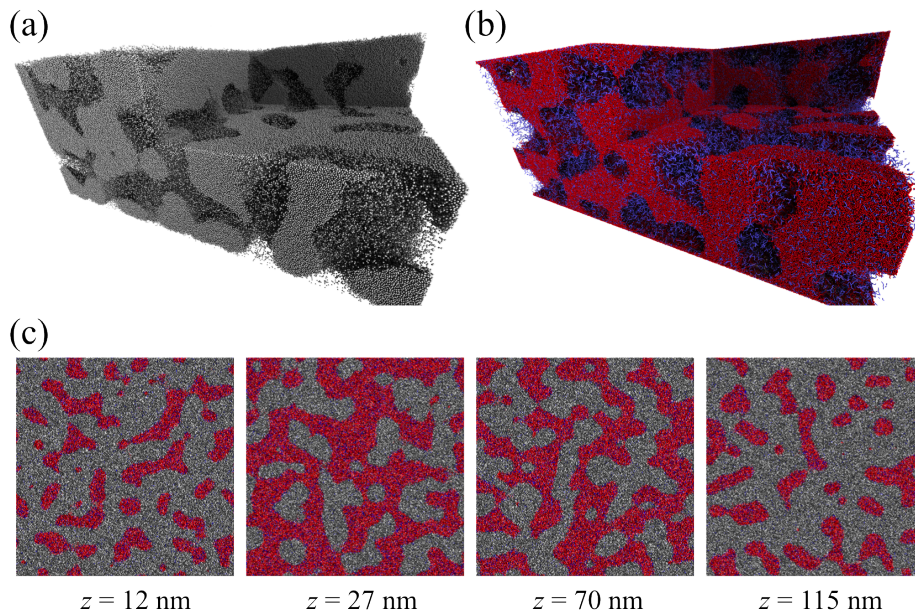


**Figure 3.1:** Illustration of MD simulations predicting the spatial distribution of PCBM (gray), low MW P3HT (blue), and high MW P3HT (red) throughout a BHJ film. Image (a) features only PCBM domains, (b) only P3HT domains, and (c) depicts slices taken near the air- ( $z=115$  nm) and substrate ( $z= 12$  nm) interfaces that contain increased concentrations of PCBM.

In this chapter of my dissertation, I examine the impact of low MW P3HT additives on morphology and photocurrent generation in P3HT/PCBM BHJ devices. Beyond the broad set of experimental studies showing that P3HT-containing additives improve device performance, this effort is motivated by recent results from large scale molecular dynamics (MD) simulations showing that BHJs comprising oligomeric P3HTs (degree of polymerization = 10) and PCBM fullerenes form a layered/smectic morphology after thermal annealing.<sup>161</sup> Because these oligomeric additives are chemically similar to the P3HT donor polymers, differing only in their MW, these studies provide insight into the impact of additive size and loading level on BHJ device performance and film morphology. My studies focused on low MW P3HT additives were completed in two stages. The first portion of this research effort was

performed to support petascale MD simulations demonstrating that small amounts of low MW P3HT modifies interfaces between donor- and acceptor-rich domains and alters PCBM distribution across the depth of the BHJ film as measured by NR.<sup>160</sup> The second part is a natural extension of this study: three different low MW P3HTs (1.6, 4.4, and 8.0 kg mol<sup>-1</sup>) are synthesized and incorporated into P3HT-PCBM films as additives at loading levels ranging from 0.1–10% by weight. Devices are fabricated and tested under simulated solar irradiation and the characteristic domain size and crystallinity of P3HT in each film is investigated by wide-angle and small-angle X-Ray scattering (WAXS and SAXS, respectively). Finally, energy filtered transmission electron microscopy (EFTEM) is used to qualitatively assess the intermixing and domain size of each sample. With this approach, I may be able to adjust BHJ film properties through controlling the lengths and mass ratios of the two P3HTs. This strategy of controlling BHJ film morphology is desirable for its straightforward synthesis and easy incorporation into scalable processing techniques via simple mixing.

### 3.3 Results & Discussion

The weight-average and number-average molecular weight,  $M_w$  and  $M_n$ , respectively, dispersity, and regioregularity of each low MW P3HT additive used in this study are listed in Table 3.1. Oligomers of three different MWs nominally referred to as 1.6k, 4.4k, and 8.0k were examined to understand how chain length of the polymer additive affects the behavior of the BHJ film. While the synthesis of the P3HT oligomers followed protocols known to give excellent control of end groups,<sup>55</sup> NMR spectroscopy shows that the regioregularity of these oligomers is slightly less than 98.5%, which is often obtained for P3HTs synthesized via the Kumada catalyst transfer poly condensation (KCTP). This lower regioregularity is due to the short chain lengths. Each chain contains a head-to-head coupling of the first two regiospecific monomers to start the KCTP cycle.<sup>162</sup> Because morphology and

electronic properties of additive-containing BHJ films vary with loading level, each of the oligomeric additives were incorporated into BHJ films at 0.1, 0.5, 1.0, 5.0, and 10.0% by weight while maintaining the ratio of (total) P3HT to PCBM constant at 1:1.

**Table 3.1:** Molecular characteristics of low MW P3HT additives used in this study where 1.6k, 4.4k, and 8.0k are the abbreviations used for each additive throughout this section.

Additive	GPC		NMR	
	Mn	PDI	Mn	% RR
<b>1.6k</b>	1,610	1.12	920	93.5
<b>4.4k</b>	4,460	1.15	2490	97.5
<b>8.0k</b>	8,090	1.11	3,590	92.0

### 3.3.1 Device Performance

Table 3.2 summarizes device performance characteristics for devices made with each of the low MW P3HT additive as a function of loading level. All values, including data for control samples containing no additives, represent the average of 6 identically prepared devices. Remarkably, an increase in power conversion efficiency (PCE) relative to control devices is observed except for devices having the 1.6k and 4.4k P3HT additives at 5 and 10% loading levels. These devices exhibit a significant decrease in PCE due to decreases in short circuit current ( $J_{sc}$ ) and fill factor (FF). The general behavior that PCE improves up to a certain loading level and decreases thereafter is a pattern that is consistent with several studies using different P3HT-containing additives that reportedly act through different mechanisms.<sup>149,151</sup> In addition to this general behavior, all of the devices featuring BHJ blends containing low MW P3HT additives show open circuit voltages,  $V_{oc}$ , that are equal to or greater than that exhibited by the control devices.

Current density-voltage curves for the best performing device from each additive and the control under illuminated and dark conditions are shown in Figure 3.2. The



**Table 3.2:** Performance characteristics for BHJ devices containing low MW P3HT additives at different levels and control devices.

Additive	Loading	$J_{sc}$	$V_{oc}$	FF	PCE
	wt. %	$mA/cm^2$	V		%
<b>Control</b>	–	$7.83\pm 0.25$	$0.58\pm 0.01$	$0.54\pm 0.01$	$2.54\pm 0.10$
<b>1.6k</b>	0.1	$8.70\pm 0.28$	$0.59\pm 0.01$	$0.59\pm 0.02$	$3.18\pm 0.18$
	0.5	$8.49\pm 0.31$	$0.60\pm 0.01$	$0.59\pm 0.02$	$3.14\pm 0.26$
	1.0	$8.37\pm 0.43$	$0.59\pm 0.01$	$0.60\pm 0.03$	$3.16\pm 0.11$
	5.0	$8.03\pm 0.15$	$0.58\pm 0.01$	$0.48\pm 0.03$	$2.37\pm 0.17$
	10.0	$7.58\pm 0.29$	$0.59\pm 0.01$	$0.42\pm 0.02$	$1.94\pm 0.17$
<b>4.4k</b>	0.1	$7.90\pm 0.10$	$0.59\pm 0.01$	$0.55\pm 0.02$	$2.67\pm 0.14$
	0.5	$9.53\pm 0.26$	$0.61\pm 0.01$	$0.56\pm 0.01$	$3.40\pm 0.11$
	1.0	$9.34\pm 0.66$	$0.58\pm 0.01$	$0.50\pm 0.03$	$2.91\pm 0.22$
	5.0	$8.09\pm 0.31$	$0.59\pm 0.01$	$0.49\pm 0.07$	$2.36\pm 0.32$
	10.0	$8.40\pm 0.43$	$0.59\pm 0.01$	$0.41\pm 0.02$	$2.12\pm 0.18$
<b>8.0k</b>	0.1	$8.45\pm 0.14$	$0.61\pm 0.01$	$0.57\pm 0.01$	$3.03\pm 0.08$
	0.5	$7.80\pm 0.27$	$0.61\pm 0.01$	$0.53\pm 0.01$	$2.61\pm 0.19$
	1.0	$8.30\pm 0.13$	$0.61\pm 0.01$	$0.57\pm 0.01$	$3.02\pm 0.13$
	5.0	$8.98\pm 0.21$	$0.62\pm 0.01$	$0.57\pm 0.02$	$3.26\pm 0.16$
	10.0	$9.42\pm 0.92$	$0.60\pm 0.01$	$0.57\pm 0.04$	$3.37\pm 0.17$

shallower, more rounded profile of the dark curves indicates that BHJ films containing the oligomeric additive have a lower overall shunt resistance compared to the control devices. Particularly noteworthy is the  $0.01 \text{ mA cm}^{-2}$  diode current of the device having the 4.4k additive at 0.5% loading level. Among the additive-modified devices tested, this device features the highest average PCE of 3.40%, which is driven, at least in part, by its low resistance. This performance is followed closely by the devices made with the 8.0k P3HT additive at 10wt.%, which have an average PCE of 3.37%. The control devices having no additive show PCE of 2.54%, which is typical and consistent with benchmark devices tested in the laboratory at Pennsylvania State University.<sup>163,164</sup> The differences in PCE between the device containing 4.4k P3HT at 0.5wt.% represent PCE improvements of  $\approx 33\%$  due to incorporation the low MW P3HT additives. While I refrain from speculating as to whether these performance

improvements are linked to beneficial morphological changes until results of film metrology are presented, previously reported petascale simulations of Carrillo et al. demonstrate that low MW P3HT chains effectively migrate to donor-acceptor interfaces, increasing interfacial area and altering domain sizes.<sup>160,161</sup>

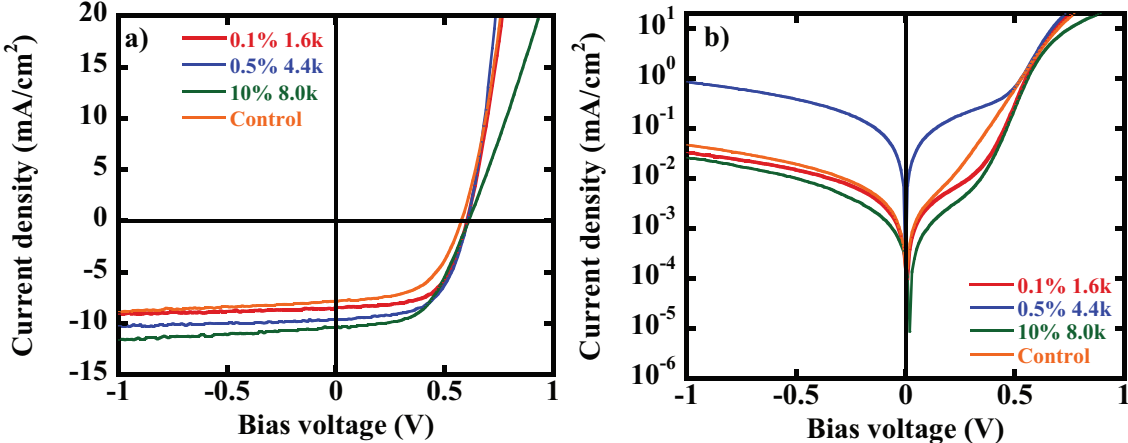


**Figure 3.2:** J-V curves under simulated light (left) and dark conditions (right) of devices made without low MW P3HT additives (control) and the best performing devices for each additive.

### 3.3.2 GI-SAXS

GI-SAXS measurements were used to gain insight into whether the low MW P3HT additives affect domain sizes or bring about changes in donor-acceptor phase separation upon thermal annealing. As seen in Figure 3.3, line-cuts along  $q_y$  show two features, the first being a broad shoulder at  $q_y \approx 0.02 \text{ \AA}^{-1}$  and the second being a smaller shoulder at  $q_y \approx 0.06 \text{ \AA}^{-1}$ , where  $q_y$  is the momentum transfer vector as defined in Equation 3.1. These features can be linked to characteristic length scales of the phase separation structure of the BHJ thin films.<sup>75,165,166</sup>

$$q_y = \frac{4\pi \sin(\theta)}{\lambda} \tag{3.1}$$

The characteristic domain sizes,  $d$ , are calculated from the local maxima of each feature by Equation 3.2.

$$d = \frac{2\pi}{q} \quad (3.2)$$

Using this analysis, the shoulders at  $q = 0.021 \text{ \AA}^{-1}$  and at  $q = 0.062 \text{ \AA}^{-1}$  in the control films (no additives) corresponds to PCBM domain sizes of 30 nm and 10 nm, respectively. A size of 30 nm in P3HT/PCBM BHJs is consistent with the size of crystalline P3HT domains,<sup>32,163,167</sup> while the scattering feature representing a size of 10 nm has not been indexed conclusively; it is speculated that it corresponds to the size or separation distance associated with fullerene clusters.<sup>168,169</sup> Although the features at 30 nm and 10 nm are obvious in all samples, clear changes in the intensities at low  $q$  are apparent with the addition of low MW PHT. These changes correspond to a coarsening of BHJ film morphology. When the MW of the additive is 1.6k, a higher slope at low  $q$  is visible in the sample with 10wt.% additive loading. At an additive MW of 4.4k, however, the upturn at low  $q$  is apparent at a lower concentration of additive, 5wt.%; with an additive of 8.0k the upturn is visible starting at 0.5wt.% additive.

Figure 3.4 captures a correlation between the MW of the additive and the concentration at which the low- $q$  upturn is apparent: the loading limit exhibits an inverse relationship with the size of the low MW P3HT. The strong upturns in the intensity at low  $q$  seen in many of the GI-SAXS measurements is attributed to coarsening of donor and acceptor domain structure. This change in behavior was observed when additive concentration exceeded 10%, 5%, and 0.5% for the 1.6k, 4.4k, and 8.0k additives, respectively. These results indicate that at low loading levels, the low MW P3HT additives do not alter the domain size or induce phase separation. At higher concentrations, BHJ morphology appears to coarsen, which could be attributed to the growth of pure PCBM clusters or from the additives migrating into and swelling the PCBM domains. These two possibilities are considered when discussing GI-WAXS data in Section 3.3.3.

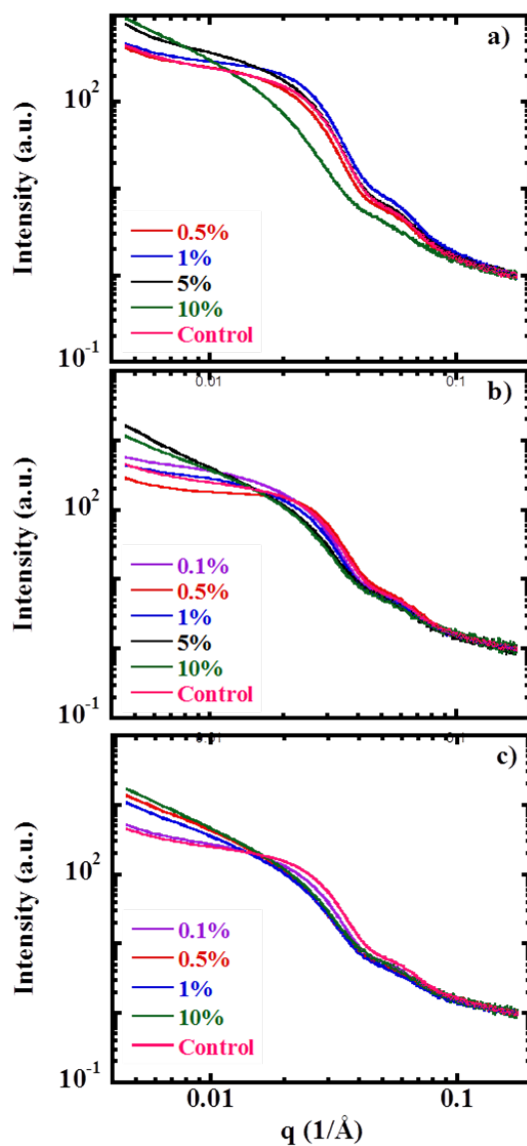


**Figure 3.3:** GI-SAXS results for annealed spin cast films of P3HT and PCBM featuring 0.1-10wt% loading levels of 1.6k (a), 4.4k (b), and 8.0k (c) P3HT additives. For comparison purposes, the scattering from an unmodified (control, pink line) BHJ blend is shown in each figure.

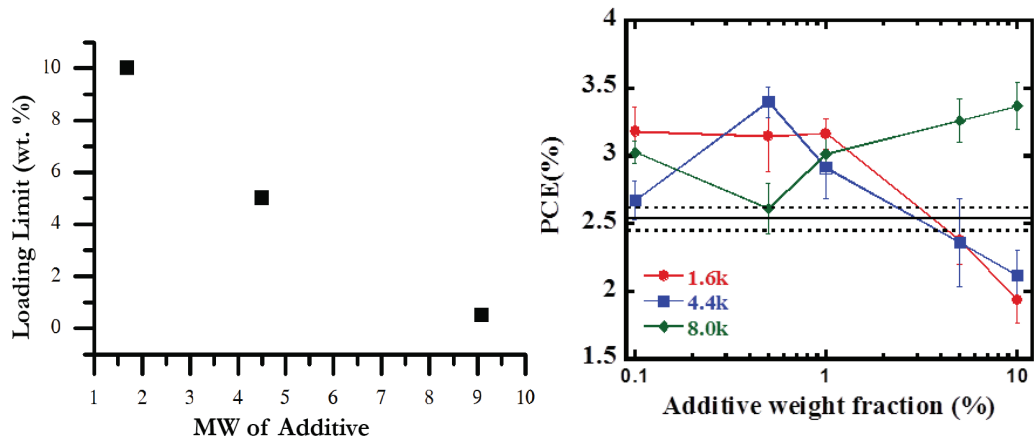


**Figure 3.4:** The loading level at which low MW P3HT additives coarsen morphology, as determined by GI-SAXS, decreases as the MW of the additive increases (left). The average PCE for devices made with each P3HT additive as a function of additive loading level. The horizontal lines indicate the PCE of the control device featuring no additives (right).

As seen in Figure 3.4, the loading levels where domain structures coarsen appear to correspond to the maximum average PCE recorded for devices featuring the 1.6k and 4.4k P3HT additives. Surpassing this limit adversely affects the PCE of low MW P3HT modified devices, ostensibly due to the increase in phase separation. This dependence of PCE on domain size is consistent with reports of P3HT-PCBM BHJ films.<sup>15,75,166,170,171</sup> The devices featuring the 8.0k P3HT additive, on the other hand, exhibit a different trend: despite having the most significant changes in domain size, the performance of the devices made with this additive initially diminished to a level expected for a control BHJ active layer, but then increased with the loading level of the additive. The origin of this behavior is unclear at this point.

### 3.3.3 GI-WAXS

To examine whether the addition of low MW P3HT affects crystallization of P3HT or PCBM in the BHJ films, a series of grazing incidence wide angle X-ray scattering (GI-WAXS) measurements was performed on films mimicking BHJ architectures used

in PCE measurements. Figure 3.5 displays a matrix of 2D images recorded for the thermally annealed films containing low MW P3HT additives at different loading levels and a control film. All of the images collected feature broad halos typically observed for P3HT-PCBM BHJs that indicate an abundance of amorphous material. Each image features an amorphous halo at  $q \approx 1.39 \text{ \AA}^{-1}$ , which corresponds to a pure PCBM phase that is seen consistently in X-ray studies.<sup>172,173</sup>

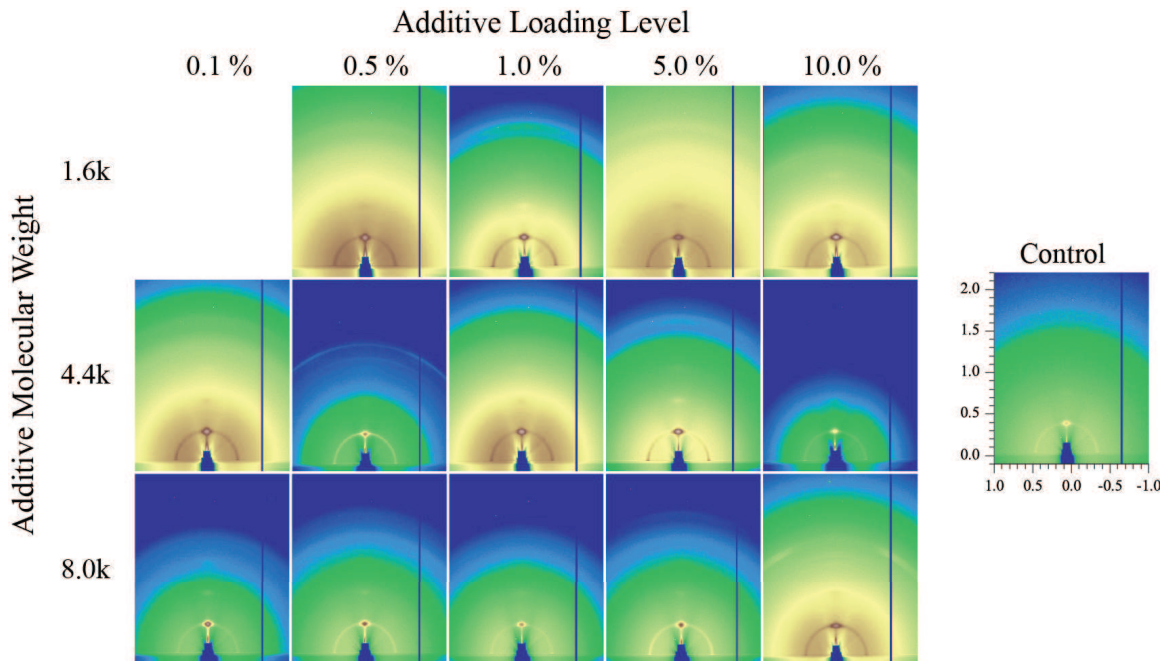


**Figure 3.5:** 2D GI-WAXS detector images for BHJ films featuring the 1.6k (top), 4.4k (middle), and 8.0k (bottom) P3HT additives is shown as a function of additive loading level (increasing from left to right, according to labels along the top edge of the images). The scattering from an unmodified control sample is shown at the right.

Figure 3.6 shows plots of the 1D intensity versus scattering wavevector,  $q$ , which is obtained by radially averaging the collected intensity about the center of the beam. As expected, strong peaks at  $q \approx 0.4 \text{ \AA}^{-1}$  corresponding to the (100) diffraction peak of P3HT chains are observed, indicating that P3HT crystallization occurs in each of the films. There appears to be no difference in the extent (intensity) between the control sample and those containing low MW P3HTs, suggesting their

presence does not affect donor phase crystallization. None of the diffraction patterns feature peaks corresponding to PCBM crystallites, which suggests that while PCBM aggregates, it does not crystallize. The lack of changes in the crystallization of P3HT or aggregation behavior of PCBM suggests that the upturn in low  $q$  intensities at high additive loading levels observed in Figure 3.3 is due to low MW P3HTs migrating into the PCBM-rich domains.<sup>173</sup> Upon migrating into the PCBM domains, the low MW P3HTs coarsen morphology as seen in the SAXS measurements and prevent the crystallization of PCBM, which is also consistent with my measurements.

### 3.3.4 TEM

EF-TEM was used to examine the morphology of the best performing P3HT:PCBM films made with the 4.4k and 8.0k low MW P3HT additives. Figure 3.7 shows the sulfur elemental maps of a neat P3HT:PCBM film and films with the 4.4k low MW P3HT additive at a loading level of 0.5% and with the 8.0k low MW P3HT additive at 0.5% and 10% loading. Sulfur map image intensities are proportional to the sulfur concentration, and the light regions indicate P3HT-rich domains. The white worm-like features containing the most S are representative of P3HT-rich regions of the BHJ film. All samples exhibit similar morphology, suggesting the addition of low MW P3HT has little to no impact on the overall morphology of P3HT:PCBM films.

### 3.3.5 Neutron Reflectivity

NR measurements were also performed to understand the potential for low MW P3HTs to arrest vertical PCBM segregation. These studies we designed to parallel MD simulations of BHJ systems that were conducted by collaborators at Oak Ridge National Laboratory. Because these studies were performed in the earlier stages of this investigation, the spirit of this study was to quantitatively confirm the unique additive behaviors predicted by MD simulations.<sup>160,161</sup> Therefore, only P3HTs having molecular weight of  $4.4 \text{ kg mol}^{-1}$  were incorporated into BHJ films at a loading of

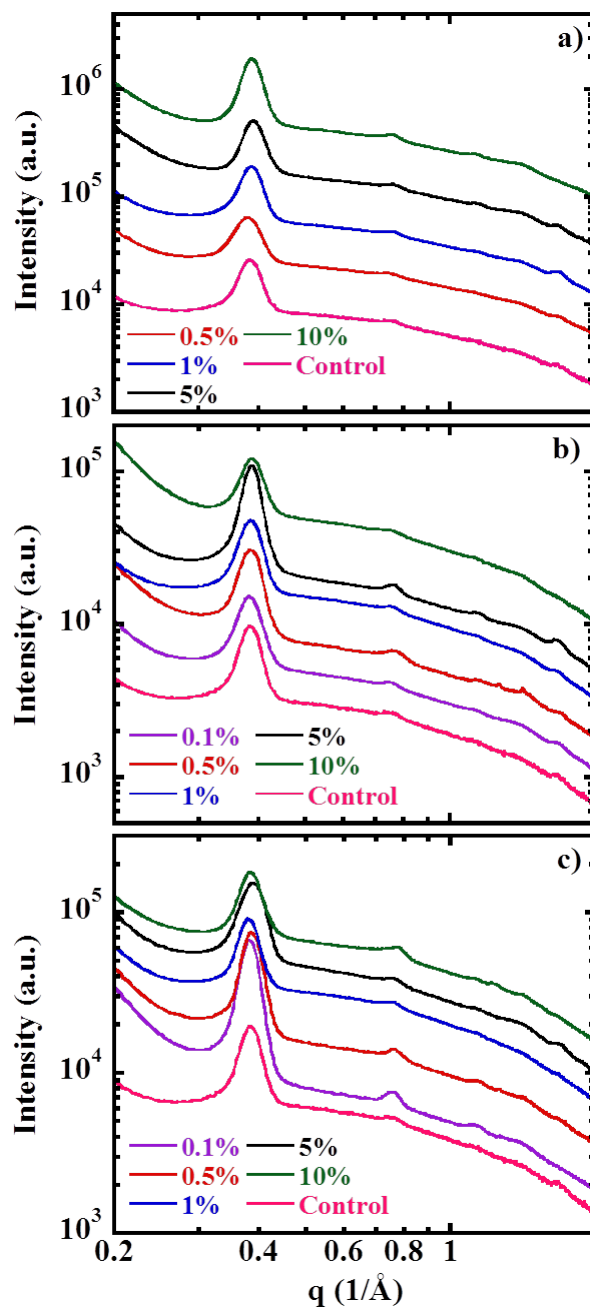


**Figure 3.6:** 1D GI-WAXS diffraction patterns for films containing the 1.6k (a), 4.4k (b), and 8.0k (c) additives at different loading levels. The color scheme used for the additive loading levels is consistently applied and traces have been vertically offset for clarity and to facilitate comparison.



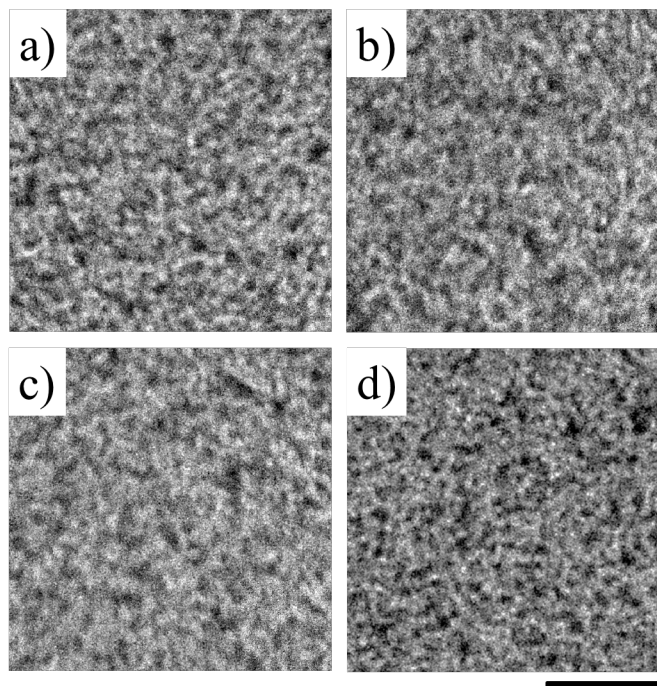


**Figure 3.7:** Sulfur elemental maps of (a) control sample and films containing (b) 4.4k at 0.5%, (c) 8.0k at 10% and (d) 8.0k at 0.5% (d). The scale bar, which is common to all images, is 200 nm.

10wt.% and compared to a control BHJ film cast on Si. The measured and predicted reflectivity profiles for the thermally annealed BHJ films are shown in Figure 3.8, where the film containing the additive is indicated by the blue line. When comparing the profiles from simulations and experiments, it is immediately apparent that there are significant differences in the Keissig fringes observed from each. In the NR profile produced from simulations, there are relatively “tight” oscillations that are well defined. On the other hand, the experimentally measured system exhibits less intense Keissig fringes that dampen as  $q$  increases. This difference arises due to the degree of intermixing between P3HT and PCBM that occurs across the depth of the film, which is not easily replicated in the MD simulations. This “smearing” of domain interfaces is also responsible for the dampening of the Keissig fringes at higher  $q$  that is present in the experimentally measured samples.

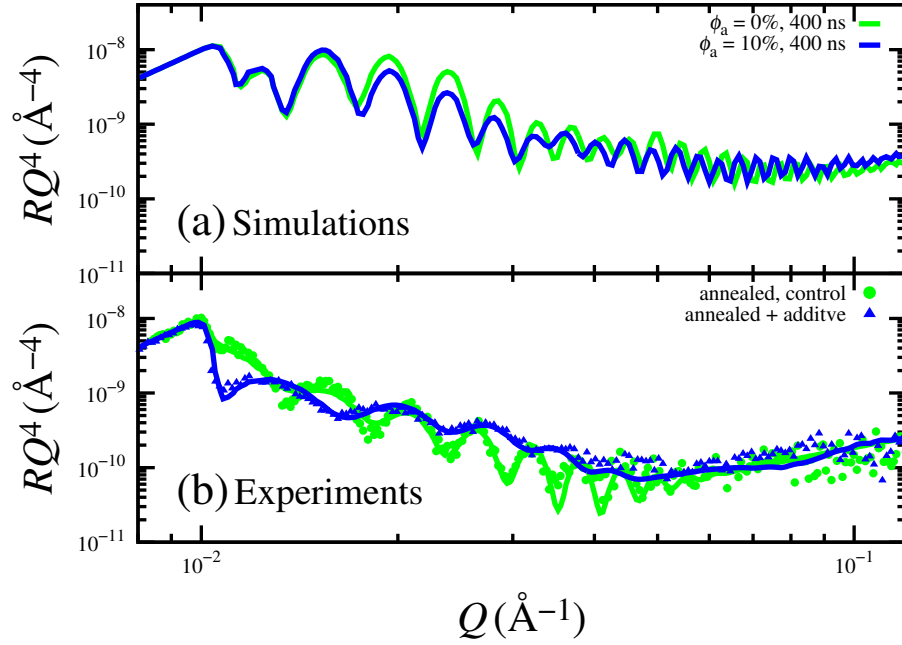


**Figure 3.8:** Comparison of the results for neutron reflectometry measurements between simulations (a) and experiments (b), represented by the relation of reflectivity multiplied by wavevector transfer to the fourth power,  $RQ^4$  versus wavevector transfer,  $Q$ . The lines in (b) are fits of the neutron reflectometry data.

The NR data was fitted using the *Layers* spreadsheet program that constructs reflectivity curves from model systems consisting of slabs (strata) based on the Parratt formalism. The SLD profiles used to generate the best-fit curve are shown in Figure 3.9a for the annealed control and additive-modified films. The Si-oxide interface is located at  $\approx 10$  nm as indicated by the sharp peaks that are aligned (at  $z \approx 10$  nm) for each sample. A more physically relevant data depiction is shown in Figure 3.9b, where the calculated SLDs are converted into PCBM volume fractions,  $\phi_{PCBM}$ , by Equation 1.8. The control film features slight increases in the SLD at the substrate-film and air-film interfaces, which correspond to 36% and 38% PCBM (by vol.), respectively. The additive-modified film features a similar SLD profile at these boundaries, as indicated by the blue line in Figure 3.9b, where volume fractions of 37 and 39% PCBM were obtained at the substrate- and air-film interfaces. Differences

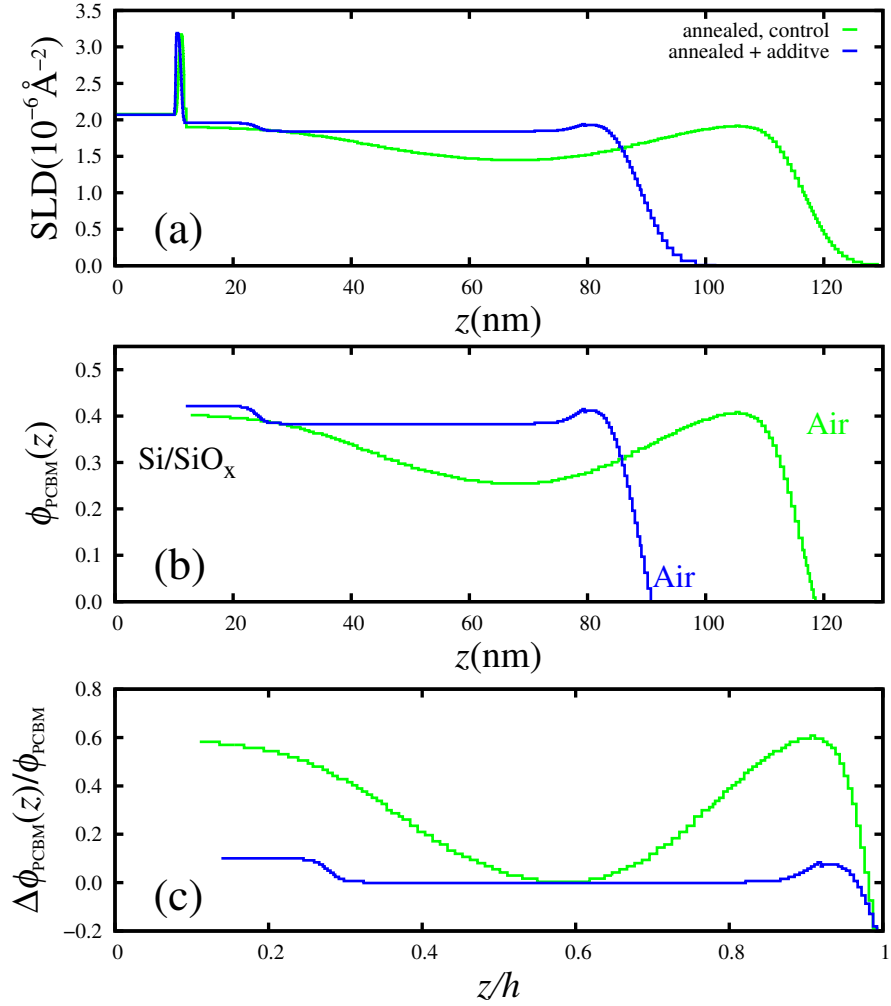


**Figure 3.9:** Analysis of the neutron reflectometry data: (a) Scattering length density (SLD) obtained from the fits in Figure 3.8 for the system with (blue) and without (green) additives; (b) PCBM volume fraction,  $\phi_{PCBM}(z)$ ; and (c) normalized change in vertical distribution of PCBM in the thickness dimension of the film,  $\Delta\phi_{PCBM}(z)/\phi_{PCBM}$ , where  $h$  denotes the thickness of the layer composed of Si, SiO<sub>x</sub>, P3HT and PCBM.

between the SLD profiles become more apparent throughout the bulk of the BHJ films. In this region the additive-modified film appears to dampen the severity of the PCBM segregation to the air-film or substrate-film interfaces as indicated by the absence of the “trough” in the experimentally measured SLD profiles.

From Figures 3.9a and 3.9b it is apparent that the control and additive-modified film thicknesses are not equal. To facilitate a better comparison of the difference in  $\phi_{PCBM}$  across the BHJ films, the SLD profiles are normalized as shown in Figure 3.9c. Here, the volume fractions of PCBM as a function of depth,  $\phi_{PCBM}(z)$ , were normalized to the bulk concentrations of the film,  $\phi_{PCBM}$ , as measured in the middle of the film. Additionally, depth was normalized by scaling the substrate-film and air-film interfaces to depths of 0 and 1, respectively. While both the control and the additive-modified films feature segregation of PCBM to the air and film interfaces, the additive-modified film’s relatively flat scaled SLD profile suggests that there is benefit to incorporating the additives. From Figure 3.9c, the  $\phi_{PCBM}$  at air/film and substrate/film interfaces of the control film featuring no additive is 60% higher than the bulk composition. On the other hand, the additive-modified BHJ film features interfacial  $\phi_{PCBM}$ s that are 10% higher than recorded in the bulk. While the collected NR profiles do not align perfectly with those predicted by MD simulations, the predictions of the simulations — that low MW P3HTs can potentially stabilize donor-acceptor interfaces and arrest transient PCBM morphology — appear to be validated by the experimentally measured NR profiles. A more detailed analysis of the simulations show diminished PCBM segregation due to the lower surface energies of the low MW P3HTs that are more aligned with that of PCBM.<sup>160</sup>

### 3.3.6 Contact Angle

In support of the predictions made via MD simulations about the underlying mechanisms driving the compatibilizing effects of low MW P3HTs, contact angle measurements were used to estimate the surface energies,  $\gamma_{sv}$ , of the materials

constituting the measured BHJ films. Numerous studies state the utility of surface energy in predicting the vertical distribution of binary blends across BHJ thin films.<sup>174–177</sup> These investigations are in agreement that the materials with the lower surface energy segregate to the air/film interfaces. Table 1 shows the average water-contact angle measurements of each pure material as well as BHJ films with and without the low MW P3HT additive. Surface energies were calculated using the Neumann Equation of State and Wu Harmonic Model, both of which are commonly used for these materials.<sup>176–179</sup>

**Table 3.3:** Contact angle measurements of water and ethylene glycol (E.G.) for thermally annealed materials and the BHJ films used in this study. The surface energies are calculated using the Wu Harmonic Model and the Neumann Equation of State. For the Neumann estimate, the water contact angle was used for the calculation.

Material	Contact Angle		Wu Harmonic			Neumann
	Water	E.G.	$\gamma_{sv}$	$\gamma_{sv}^d$	$\gamma_{sv}^p$	$\gamma_{sv}$
<b>5.6k P3HT</b>	92.1°	62.2°	35.0	28.2	6.8	28.0
<b>30k P3HT</b>	87.0°	61.8°	39.1	31.9	7.2	31.1
<b>PCBM</b>	93.4°	58.9°	35.2	28.4	6.8	27.1
<b>Modified</b>	104.1°	76.6°	23.5	18.2	5.3	20.6
<b>Control</b>	86.0°	68.8°	27.4	23.1	4.3	28.5

From an experimental perspective, the Neumann Equation of State is generally considered preferable for similar materials because it only requires the use of one liquid. On the contrary, the Wu Harmonic Model requires the use of at least two liquids that feature significantly different surface tensions. Using two liquids is advantageous as it provides a method by which the polar ( $\gamma_{sv}^p$ ) and dispersive ( $\gamma_{sv}^d$ ) components of a material’s surface energy can be calculated. Using water and ethylene glycol as the two liquids, surface energies calculated by the Wu Harmonic Model suggest that PCBM has the lowest surface energy of the three materials used in this study. In the absence of an additive, this lower surface energy could account for the PCBM segregation to the air-film interface, which is seen in the neutron reflectometry

results. The relatively lower surface energy of the shorter P3HT additives compared to the 30 kg/mol matrix P3HTs also explains the reduced segregation of PCBM to the air/film interface. Based on the contact angle measurements, the low MW P3HTs provide entropic competition with the PCBM that appears to have a stabilizing effect on the PCBM segregation processes.

### 3.4 Conclusions

In this two-part study, the effect of P3HT additives that differ from the donor polymer only in their MW was investigated at multiple loading levels. PCE improvements up to 33% were observed, suggesting that the molecular size of the additive has a significant impact on the morphology and performance of BHJ OPV devices. GI-SAXS studies identified critical loading limits for each P3HT additive that are inversely proportional to the MW of the additive. Exceeding this loading level induces phase separation, which is marked by a growth of large-scale structures in the active layer along with a decrease in PCE. GI-WAXS measurements show no significant changes in the crystallinity of the donor polymer phase in the additive-modified films. Based on NR measurements, the low MW P3HT additives show promise in that they appear to limit the phase separation of PCBM throughout the depth of the BHJ film. Peta-scale MD simulations reveal that low MW P3HT additives limit PCBM segregation due to a lower surface energy that is nearly equal to that of PCBM. This hypothesis is in agreement with conclusions/inferences drawn from contact angle measurements of PCBM as well as low and high MW P3HTs. In total, these findings demonstrate that the physical size and loading levels of an additive are just as important as chemical design, and must be taken into consideration when developing new additive materials for BHJ films.

## 3.5 Experimental

### 3.5.1 Device Fabrication & Performance

Photovoltaic devices were fabricated and tested as previously described.<sup>169,180</sup> Briefly, ITO-coated glass substrates were cleaned by sequential rinsing with 1% Aquet detergent solution, water, acetone, and isopropanol. They were then dried using filtered N<sub>2</sub> and then cleaned via UV ozonolysis for 30 min. After cleaning, anode buffer layers consisting of a 1:6 blend of poly(ethylenedioxythiophene:polystyrenesulphonate) (PEDOT/PSS) at 1.3wt% in H<sub>2</sub>O were spin-coated onto the indium tin-oxide coated glass at 1,000 rpm for 1 min. These substrates were then thermally annealed at 110 °C for 15 min to remove any residual water within the polymer thin film. The samples were transferred to a nitrogen-filled glove box where P3HT and PCBM were deposited by spin coating from a chlorobenzene solution at 1,000 rpm for 3 min. The ratio of P3HT and PCBM was held constant at 1:1 for all BHJ thin films. The low MW P3HT additives were added based on the total P3HT mass content. Device fabrication was completed by applying aluminum cathode layers of nominally 1 μm thick atop each active layer film via metal vapor deposition. While remaining in the N<sub>2</sub>-filled glove box, each device was annealed at 165 °C for 15 min and tested under AM 1.5 G 100 mW/cm<sup>2</sup> illumination. Current-voltage characteristics were measured and recorded using a Keithley 2636A source meter.

### 3.5.2 X-Ray Scattering

Prior to film deposition, all silicon substrates were cleaned by sequentially rinsing each substrate with chloroform, acetone, and methanol and then drying with a filtered stream of N<sub>2</sub>. Films mimicking BHJ blends were cast on silicon substrates in a N<sub>2</sub> filled glove box. After casting, films were annealed at 165 °C for 15 min and allowed to cool to room temperature. X-ray diffraction measurements were collected at Lawrence Berkeley National Laboratory using Beam Line 7.3.3.

### 3.5.3 Energy-Filtered Transmission Electron Microscopy

Samples for EF-TEM were prepared by first depositing PEDOT:PSS layers onto clean Si substrates following protocols outlined in the device fabrication process (Section 3.5.1). Although the PEDOT:PSS film is dried under vacuum, no heat is applied to facilitate easier solvation with water in later steps. Next, chlorobenzene solutions containing P3HT, PCBM, and the low MW P3HT additive are deposited on top of the PEDOT:PSS coated silicon substrates (Silicon Sense). The substrate was slowly lowered into distilled water at a slight angle, allowing the underlying PEDOT:PSS layer to dissolve. As the PEDOT:PSS layer dissolves, the insoluble BHJ film floats off the substrate. Finally, a clean TEM grid is carefully passed through the BHJ film sitting on the water surface, causing the film to adhere to the grid. These samples were vacuum dried overnight to ensure complete removal of any water. Thermal annealing of TEM samples was carried out in a N<sub>2</sub> glove box at 165 °C for 15 min. EF-TEM were conducted on an FEI TITAN G2 at the Materials Research Institute, at Pennsylvania State University. The standard three-window method was employed to obtain sulfur elemental maps.

### 3.5.4 Neutron Reflectivity

Neutron reflectivity measurements were performed at Beam Line 4b (Liquids Reflectometer) at the Spallation Neutron Source. A series of six wavelengths and 3 angles were used to measure the reflectivity over the momentum transfer vector range of  $0.002 < q < 0.26 \text{ \AA}^{-1}$ . The reflectivity profiles were fitted iteratively using *Layers* software in which multilayer profiles were constructed and reflectivity calculated based on the Parratt formalism to replicate all major features of the data and minimize error according to a goodness-of-fit test based on the normalized sum of the square of the deviation. The scattering length densities (SLDs) used in the fitting software were based on previous reports of neat films:<sup>18</sup>  $SLD_{P3HT} = 0.68 \times 10^{-6} \text{ \AA}^{-2}$  and



$SLD_{PCBM} = 4.3 \times 10^{-6} \text{ \AA}^{-2}$ . NR measurements used BHJ films cast on 2" polished Si wafers.

### 3.5.5 Contact Angle

Films used in each contact angle measurement were prepared by dissolving the material to be measured component in chloroform at  $10 \text{ mg mL}^{-1}$  followed by spin coating at 800 rpm for 30 s. After casting, each film was thermally annealed at  $150 \text{ }^\circ\text{C}$  for 15 min under vacuum. Surface energies for each film were estimated from the water contact angle by implementing one of two commonly-used methods to calculate the surface free energy (SFE). The first relationship used was the Neumann Equation of State,<sup>181</sup> shown in Equation 3.3, where  $\theta$  is the liquid contact angle and  $\gamma_{sv}$  and  $\gamma_{lv}$  are the surface and liquid surface energies, respectively.

$$\cos(\theta) = -1 + 2\sqrt{\frac{\gamma_{sv}}{\gamma_{lv}}}e^{-\beta(\gamma_{sv}-\gamma_{lv})^2} \quad (3.3)$$

While used in numerous sources, much debate exists surrounding the appropriate value of the coefficient  $\beta$  to use in these calculations. 0.0001247 was used for  $\beta$ . The Wu Harmonic Model<sup>176,178</sup> also was used to calculate the polar and dispersive components,  $\gamma_{sv}^p$  and  $\gamma_{sv}^d$ , respectively, of the surface free energy. The fact that this model contains two unknowns demands that contact angles be measured two different liquids, which allow simultaneous solving of two different expressions. For these measurements, water and ethylene glycol were used and the appropriate equations are shown in Equations 3.4 and 3.5.

$$\frac{\gamma_{lv,w}^d \gamma_{sv}^d}{\gamma_{lv,w}^d + \gamma_{sv}^d} + \frac{\gamma_{lv,w}^p \gamma_{sv}^p}{\gamma_{lv,w}^p + \gamma_{sv}^p} = 0.25\gamma_{lv,w}(1 + \cos(\theta_w)) \quad (3.4)$$

$$\frac{\gamma_{lv,eg}^d \gamma_{sv}^d}{\gamma_{lv,eg}^d + \gamma_{sv}^d} + \frac{\gamma_{lv,eg}^p \gamma_{sv}^p}{\gamma_{lv,eg}^p + \gamma_{sv}^p} = 0.25\gamma_{lv,eg}(1 + \cos(\theta_{eg})) \quad (3.5)$$

The parameters for water and ethylene glycol used in this analysis are given in Table 3.4. These polar and dispersive components of the surface energy were used in the Fowkes relationship,<sup>182</sup> shown in Equation 3.6, to calculate the average surface energies,  $\gamma_{sv}$ .

$$\gamma_{sv} = \gamma_{sv}^d + \gamma_{sv}^p \quad (3.6)$$

**Table 3.4:** Summary of the total surface tension and the polar and disperse components of the liquids used for Wu Harmonic Model.

Liquid	$\gamma_{lv}$	$\gamma_{lv,pol}$	$\gamma_{lv,dis}$	
	mN/m	mN/m	mN/m	
<b>Water</b> <sup>183–185</sup>	72.8	51.0	21.8	93.5
<b>Ethylene Glycol</b> <sup>186</sup>	4,460	1.15	2490	97.5

## Chapter 4

# Porphyrin-Capped P3HTs as Additives

## 4.1 Abstract

The morphology of the bulk heterojunction (BHJ) active layer has been repeatedly linked to the performance and longevity of organic photovoltaic (OPV) devices. Through investigations to control the morphology, non-covalent interactions have proven to be a facile way to reduce fullerene migration in an active layer. This work presents the first synthesis of porphyrin-capped poly(3-hexylthiophene)s (PP-P3HT)s designed to take advantage of strong porphyrin:fullerene intermolecular interactions to improve control over BHJ morphology. The impact of PP-P3HTs on BHJ morphology is optimized by adjusting the loading level of the additive. The synthetic protocols for those new materials are discussed, and detailed characterization results confirming the coupling of the two macromolecules are presented. Finally, basic optical and thermal measurements that offer insight into the viability of porphyrin-P3HTs as performance enhancers for OPV applications are presented and described.

## 4.2 Introduction

Porphyrins are intriguing as additives in BHJs due to their favorable absorption properties and their tendency to coordinate with fullerene-based acceptors.<sup>187,188</sup> The formation of porphyrin-PCBM complexes is thought to arise due to relatively strong electrostatic attractions between the electron-rich (6:6) ring-juncture bond of the fullerene and the electropositive center of the porphyrin.<sup>165,187</sup> Given the strong, directional nature of the porphyrin-fullerene interactions, it is believed that porphyrins present an opportunity to influence the morphological structure of BHJ films, especially at the donor/acceptor interface where exciton dissociation occurs. From a processing standpoint, porphyrins are known to be compatible with materials and solvents used in typical solution-based OPV device fabrication protocols. Despite these benefits, integrating porphyrins into OPV systems is complicated by their strong propensity to crystallize, leading to small recombination centers or phase separation.

These drastically reduce electronic performance.<sup>189–191</sup> In response to these pitfalls that sap performance, many efforts to overcome these problems have been pursued in recent years.

Many investigations demonstrate that the addition of functional groups on the porphyrin ring can be tailored to increase<sup>192</sup> or decrease<sup>193–196</sup> crystallization tendencies. One very successful method of suppressing porphyrin crystallization has been through the strategic addition of bulky substituents that sterically limit the ability of porphyrins to stack.<sup>195</sup> Substituents ranging in size from phenyl groups<sup>195</sup> to larger carbo-alkoxy<sup>197</sup> groups have been used to affect porphyrin crystallization in BHJ films. More recently, porphyrin pendants have evolved into larger macromolecules, including donor polymers or acceptor nanoparticles such as fullerenes.<sup>80,198,199</sup> In most cases, the incorporation of porphyrin structures into BHJ films, as additives or donor replacements, results in an increase in the PCE and lifetime of the device. The observed performance increases arise due to a variety of factors, including increased solar absorption, refinement of BHJ morphology, and enhancement of electronic processes at the donor/acceptor interfaces within the films.

The attachment of bulky substituents to porphyrin additives have shown little to no influence on their optical properties or the resulting BHJ films. This is important as the broader absorption band is important for enhanced solar absorption, which is a major driving factor of the  $J_{SC}$ .<sup>200</sup> The design of the porphyrin does, however, maintain a large influence over the electronic processes occurring between the porphyrin ring and fullerene acceptors. For example, the addition of carboalkoxy groups to phenyl pendants of porphyrin rings significantly impact molecular-assembly processes and result in increased charge diffusion lengths of 20–25 nm, which is significantly longer than the diffusion length in many state-of-the-art donor polymers.<sup>197</sup> Interestingly, this same study found that the charge diffusion rate decreased for longer alkyl substituents, such as octyl chains compared to hexyl chains, due to increases in crystallinity with increasing alkyl chain-length.<sup>197</sup> These findings

suggest there is a balance between generating stable charges and providing a favorable pathway by which the charges can move throughout the BHJ film.

From a morphological perspective, the inclusion of porphyrins, even as small molecules, has resulted in increased thermal stability and long-term PCE. In BHJ films of polycyclohexane (PCHE) and PCBM, it was shown that tetra-(2-naphthyl)porphyrin could be added to form donor/acceptor complexes that would reside near PCHE-PCBM interfaces.<sup>201</sup> These donor/acceptor complexes stem from the strong porphyrin-PCBM interactions that prevent large aggregate formation of PCBM, as indicated by DSC and optical microscopy.<sup>80</sup> PCBM crystallization (measured by DSC) shifts to higher temperature with increasing additive suggesting that the porphyrin is interacting with PCBM and limiting its ability to crystallize.<sup>80</sup> These results also agree with a more recent study by Wang and coworkers that extended the porphyrin-additive concept by synthesizing porphyrin-capped donor/acceptor copolymers that increased OPV device performance and extended operating lifetimes.<sup>202</sup> More novel structures, such as porphyrinfullerene dyads, have unambiguously demonstrated their ability to self-assemble into a well-defined 3D structures with alternating arrangements of separate domains of porphyrin and  $C_{60}$  fullerenes in the solid state.<sup>198</sup> One notable caveat to the incorporation of porphyrins was recognized by Chevrier et al., who demonstrated that porphyrins attached at the end of P3HT chains disrupt the red-shift observed for annealed P3HT films.<sup>203</sup> Although device performance measurements were not reported, these results suggest that films containing high loading levels of porphyrin-capped P3HTs feature less  $\pi$ - $\pi$  stacking between P3HT chains, and would, therefore, be less electronically efficient.

Investigations of porphyrin-polythiophene copolymers have suggested an inverse correlation between the thiophene length and charge extraction of the resulting BHJ film.<sup>204</sup> Specifically, zinc porphyrin-terthiophene and zinc porphyrin-oligothiophenes having  $M_n=4100$  g/mol polythiophene blocks decrease electron charge mobility compared to shorter tertthiophene copolymers. The first example of P3HT-porphyrin structures used in OPV devices was reported by Sessler and company in 2012.<sup>193</sup>

They achieved a 63% increase in PCE when oligothiophenes ( $M_n \approx 800$  g/mol) were coupled onto porphyrins; however, no morphological studies were performed.<sup>193</sup> Replacing P3HTs with P3HT-porphyrin copolymers in BHJ films resulted in decreased PCBM aggregation at the air-film interface.<sup>205</sup> Even more beneficial is that BHJ film morphology and PCE improvements remained after extended thermal annealing treatments. These performance increases were attributed to the generation of more stable charge carriers, as suggested by the higher hole mobilities from analogous field-effect transistor measurements. Wang used quinoxalino[2,3-b]porphyrinatozinc-capped poly(2,2-bithiophene-diketopyrrolopyrrole)s as donor/acceptor copolymer and achieved PCEs of 4.4%, which were ascribed to increased solar absorption and a finer BHJ morphological structure.<sup>202</sup> Andernach and company synthesized 4- and 2-armed porphyrin-P3HT macrostructures via Stille coupling reactions, and showed that BHJ containing porphyrins had lower PCEs than devices without the porphyrins. This decrease in PCE is presumably due to the lower regioregularity of the P3HTs synthesized via the Stille coupling reaction, which reduces the mobility of charges through the P3HT domains.<sup>205</sup> While the design of porphyrins is important, these findings underscore the sensitivity of BHJ electronic processes to the molecular properties of the donor polymer to which the porphyrin is attached.

In this chapter, these efforts are built upon by developing a robust route for synthesis of well-defined phenylporphyrin-functionalized poly(3-hexylthiophene)s (PP-P3HT)s via a post-polymerization modification strategy. This approach allows for exhaustive characterization of the P3HT polymer and porphyrin macrocycle before coupling, thereby affording detailed information regarding size, regioregularity (of the P3HT), and chemical functionality. Utilizing the robust hydrosilylation reaction strategy, this synthetic process is also amenable to a range of different donor polymers and porphyrins, allowing more exotic materials to be realized. In the sections that follow, the synthesis of these end-functionalized polymers is presented and their molecular and optoelectronic properties are investigated and discussed in detail. X-ray diffraction and differential scanning calorimetry (DSC) measurements are used

to examine the potential of PP-P3HTs to form crystalline structures. Additional DSC measurements are performed to understand how the PP-P3HTs affect thermal properties when incorporated in P3HT/PCBM blends. Finally, PP-P3HT additives are incorporated into OPV devices at various loading levels to examine their influence on device performance.

Throughout these measurements, PP-P3HTs were incorporated into P3HT:PCBM BHJ blends at loading levels ranging from 1-20% by wt. of the total P3HT. These samples are referred to as PP-P3HTX, where X is the loading level. This convention is used consistently throughout this chapter.

## 4.3 Results & Discussion

### 4.3.1 Synthesis

Allyl-terminated P3HTs were synthesized according to the procedure outlined in Appendix A.1. The MW and regioregularity of the allyl-terminated P3HTs (allyl-P3HT) and porphyrin-terminated P3HTs (PP-P3HT) are summarized in Table 4.1. MALDI-TOF mass spectroscopy measurement revealed end group compositions of 13% allyl/allyl, 71% Br/allyl, 9% H/allyl, 4% Br/Br, and 3% Br/isopropyl, and the full spectrum is shown in Figure B.4.3 of Appendix B. Numerous attempts were made to measure by MALDI-TOF MS the conversion of the allyl end groups to the chlorosilane and porphyrin functionalized products. In these experiments, dithranol, cyclohexanoic acid, and trans-2[3-(4-tert-butylphenyl)-2-methyl-2-propenyldiene]malononitrile were all used as the matrix materials, both with and without silver acetate salt, but none of these conditions allowed for analysis of the silane-functionalized P3HTs. It is, however, worth noting that no peaks corresponding to allyl-terminated P3HTs were present in MALDI-TOF-MS measurements of PP-P3HT or silane-terminated P3HT. In fact, only peaks corresponding to the Br/Br and Br/isopropyl end groups were observed.



Several attempts to attach the porphyrin at the end of P3HTs were examined, including various metal-catalyzed reactions and screening of multiple bases to facilitate the hydrosilylation coupling. In short, imidazole was found to be sufficiently basic to facilitate coupling between the -OH functional group of 5-(4-hydroxyphenyl)-10,15,20-tristolyldiporphyrin (THTP) and a chlorosilane located at the end of the P3HT chain. The product after coupling will be referred to as PP-P3HT throughout the remainder of this text. This approach, shown in Figure 4.1, uses the same strategy for synthesizing and post-polymerization modification of P3HT as described in Chapter 2. A major difficulty in this approach is ensuring complete removal of any free porphyrin that did not couple with P3HT. After exploring numerous purification strategies and solvents, soxhlet extractions with acetone and ethanol were found to successfully purify the PP-P3HT product, removing excess imidazole and unreacted porphyrin. Once purified, the PP-P3HT was recovered from the soxhlet thimble using chloroform and then characterized via size-exclusion chromatography, NMR spectroscopy, and MALDI-TOF spectroscopy.

In comparison to the allyl-P3HT, the elugram of the PP-P3HT (shown in Figure B.3.2) featured a slightly shorter retention time and a broadened molecular weight distribution. The collected  $^1\text{H-NMR}$  spectra of THTP and the PP-P3HT products are shown in Figure 4.2. The successful coupling is confirmed by  $^1\text{H-NMR}$  upfield shifts of the doublet peaks corresponding to the hydroxy-containing phenyl group (7.15 ppm to 7.8 ppm for the protons nearest the porphyrin inner ring and 8.05 ppm to 8.45 ppm for the protons adjacent to the hydroxy group). Also worth noting from the  $^1\text{H-NMR}$  is the absence of free THTP and imidazole, which indicates that acetone and ethanol rinses successfully removed these two starting materials. The  $^1\text{H-NMR}$  for allyl-P3HT is shown in Appendix B, Figure B.4.2.

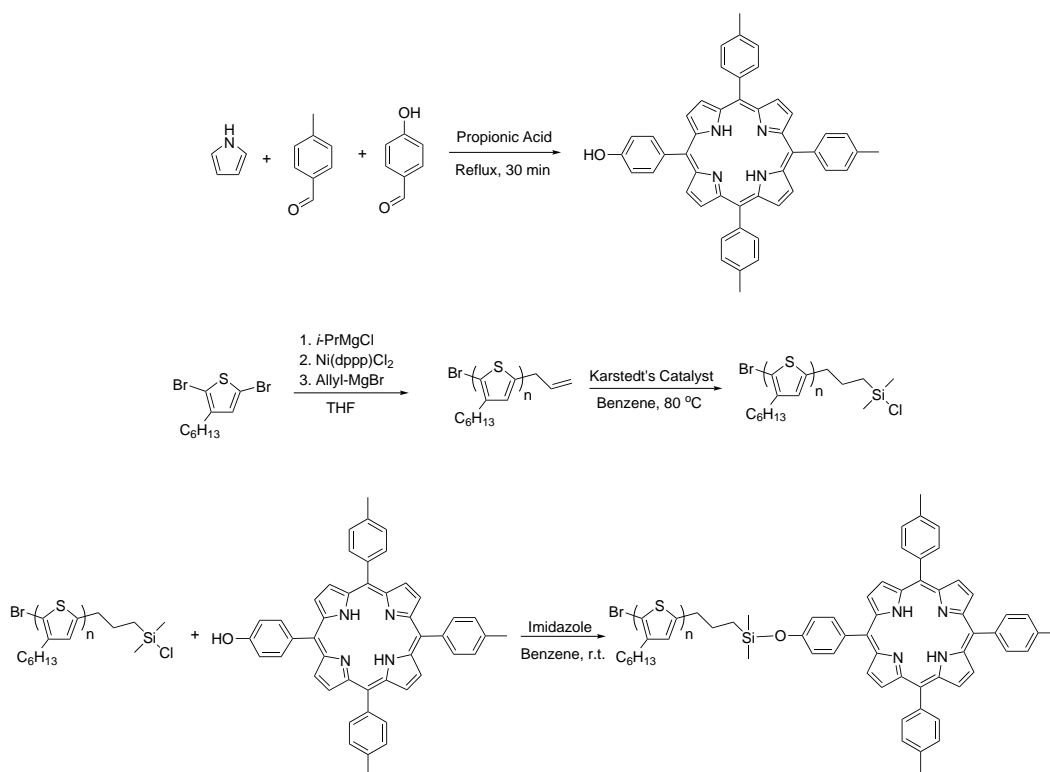


**Figure 4.1:** Reactions used to synthesize THTP (top), chlorosilane-terminated P3HTs (middle), and the final coupling reaction to form porphyrin-capped P3HTs (bottom).

### 4.3.2 UV-Vis Spectroscopy

UV-Vis spectroscopy was used to measure changes in absorbance brought about by introduction of the porphyrin at the end of the P3HT chain, with measurements made both in solution and in thin films. The UV-Vis solution spectra for THTP, allyl-terminated P3HT, and porphyrin-capped P3HTs are shown in Figure 4.3. P3HT absorbs across the 350–525 nm range and does not feature any significant shoulders or sharp peaks. The spectra of the THTP exhibits a Soret band at  $\approx 420$  nm as well as four distinct Q-bands starting at 500 nm. The porphyrin-capped P3HT exhibits traits of both the porphyrin and the P3HT UV-Vis profiles. Immediately apparent is the Soret band of the porphyrin at  $\approx 420$  nm in the PP-P3HT absorbance profile. This feature and the presence of Q-bands Q1 and Q2 located at  $\approx 600$  nm, which

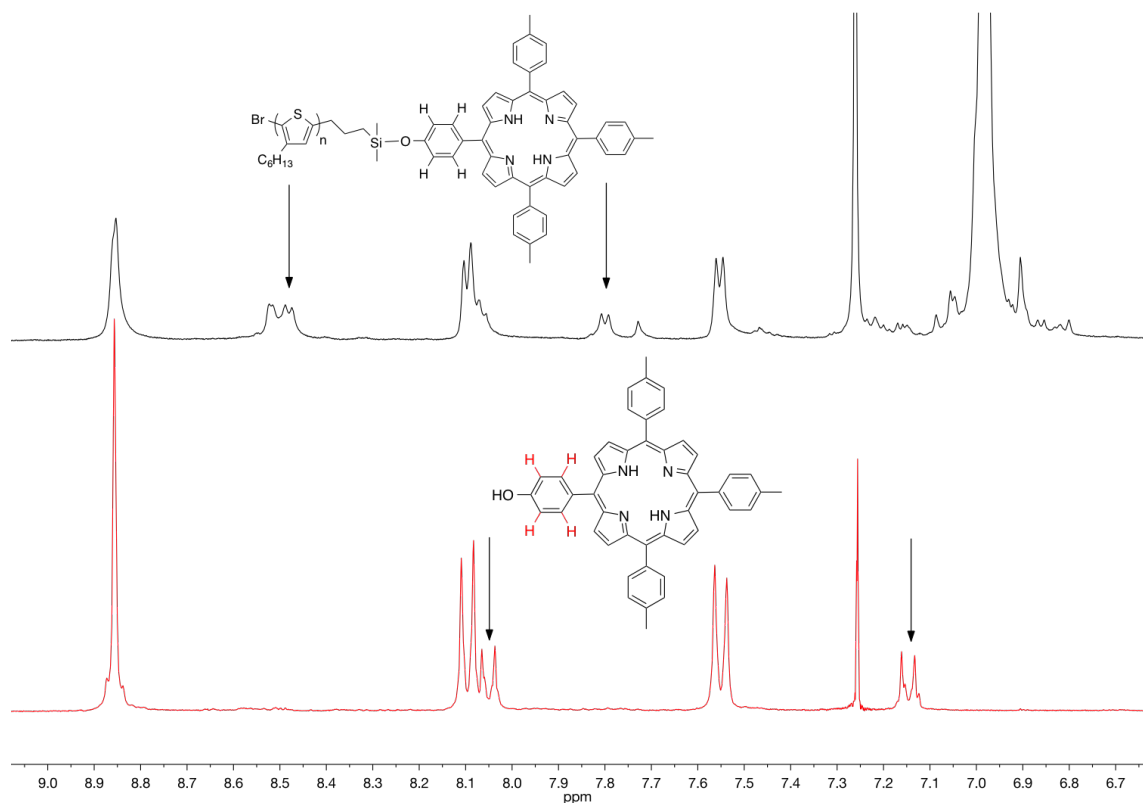


**Figure 4.2:** NMR spectra for THTP (bottom) and PP-P3HT (top). The arrows identify the peaks corresponding to the protons on the hydroxy-containing phenyl group. The shifts of these protons occur from 7.15 to 7.8 ppm for protons nearest the porphyrin inner ring and 8.05 ppm to 8.45 ppm for the protons adjacent to the hydroxy group .

are seen in the inset graph in Figure 4.3, offer further confirmation that the coupling reaction was successful. Figure 4.4 accentuates the difference between the PP-P3HT absorbance behavior in solution and as a thin film. Specifically, there is a distinct red-shift of 20 nm of the Soret band, likely due to an increase of  $\pi$ - $\pi$  interactions. Also, characteristics of P3HT crystallization appear as evidenced by the large red-shift from 450 nm to 550 nm of the UV-Vis spectrum for the PP-P3HT film, which is depicted as the red line in Figure 4.4. This sample also features shoulders appearing at  $\approx$  550 nm and 615 nm arising from the increased  $\pi$ - $\pi$  stacking between thiophene rings of the P3HT repeat units.

**Table 4.1:** Molecular characteristics of P3HTs before and after coupling of the THTP to the allyl-terminated P3HT.

Additive	GPC		NMR	
	$M_n$	PDI	$M_n$	% RR
<b>allyl-P3HT</b>	4,460	1.12	920	93.5
<b>PP-P3HT</b>	5,760	1.15	2490	97.5

UV-Vis spectra of the as-cast and annealed allyl- and porphyrin-capped P3HT films are shown in Figure 4.5. Compared to the as-cast film, the spectra of the annealed allyl-P3HT film is red-shifted and features shoulders at  $\approx 550$  and 615 nm. These red-shifts occur due to the overlapping of the  $\pi$ - $\pi$  orbitals of the thiophene rings of the crystallized P3HT chains, which is known to increase the charge carrier mobility in those domains.<sup>48,49</sup> The fact that the porphyrin-capped P3HT spectra shows a similar shift upon thermal annealing suggests that the porphyrin moiety at the chain end is not preventing crystallization of the P3HT chains. Interestingly, these results differ from a recent report that used UV-Vis spectra to show that porphyrin-capped P3HTs lacked these crystalline P3HT features. The lack of crystallinity was attributed to the bulkiness of the porphyrin functional group.<sup>203</sup> The differences between the spectra of Chevrier et al. and those presented herein remain unclear, since their report did not include extensive macromolecular characterization of their PP-P3HT product.

The photophysical properties of PP-P3HT/PCBM BHJ blends were also investigated by UV-Vis spectroscopy and the results are shown in Figure 4.6. As the interest in incorporating the porphyrin-capped P3HT is driven by the idea of using the strong interactions between porphyrin centers and PCBM, it is encouraging to see a further red-shift in the Soret band of the PP-P3HT:PCBM blend in comparison to a pristine PP-P3HT film. This shift is a manifestation of the strong  $\pi$ - $\pi$  interactions between PCBM and the porphyrin macrocyclic ring that effectively reduces the energy level of the Soret band of the macrocycle. The absorption band of the amorphous P3HT

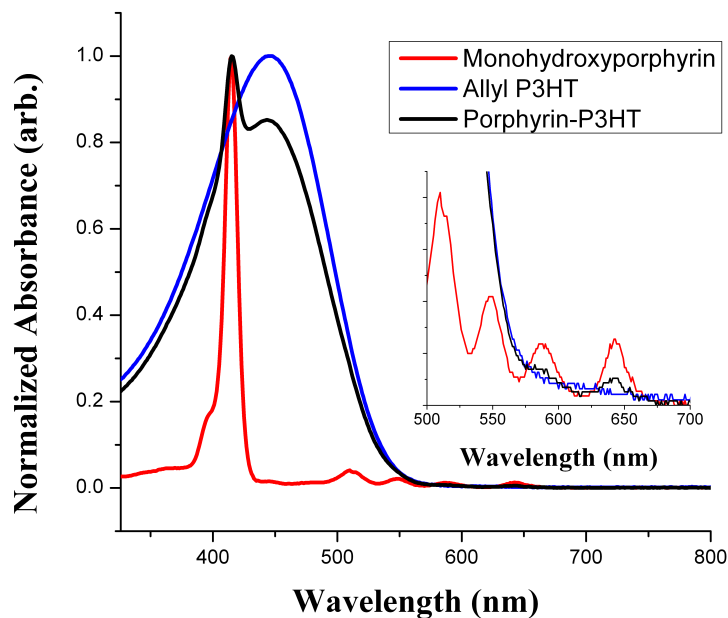


**Figure 4.3:** Solution UV-Vis spectra of THTP (red), allyl-terminated P3HT (blue), and porphyrin-capped P3HT (black). The inset features a zoomed-in view of the region containing the Q-bands of the THTP and porphyrin-capped P3HTs.

is slightly blue-shifted in the presence of PCBM compared to neat films due to the miscibility of PCBM and amorphous P3HT, which decreases the intra- and inter-chain organization of P3HT.<sup>206</sup> On the other hand, bands corresponding to crystallization of P3HT at 555 nm and 605 nm remain unaffected as the crystalline regions contain no PCBM. The absence of PCBM in crystalline P3HT domains is in agreement with other reports of BHJ blends.<sup>207</sup> The strong peak at  $\approx 335$  nm results from the strong absorption of PCBM aggregates.<sup>206,208,209</sup>

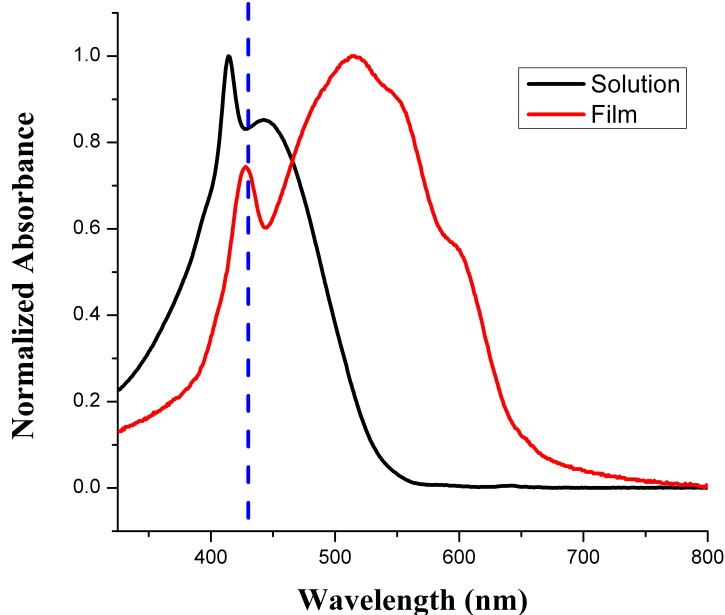


**Figure 4.4:** Comparison of UV-Vis spectra of solution (black) and pristine film (red) of the PP-P3HT additive.

### 4.3.3 Fluorescence Quenching

Fluorescence spectra of PP-P3HT were measured as a function of the concentrations of PCBM in solution to monitor the interactions between porphyrins and PCBM nanoparticles. A graph containing fluorescence spectra for concentrations measured over a PCBM concentration range of 0 M to  $3.16 \times 10^{-8}$  M is presented in Figure 4.7. The PP-P3HT exhibits a strong emission at  $\approx 560$  nm. A reduction in the intensity of this emission is observed as the concentration of PCBM increases, which is a consequence of intermolecular charge transfer from PP-P3HT to PCBM. Being an electron acceptor, the PCBM absorbs the excited electron to its lowest unoccupied molecular orbital, which prevents emission of a fluorescent photon and results in a reduction of the emission seen by the detector.

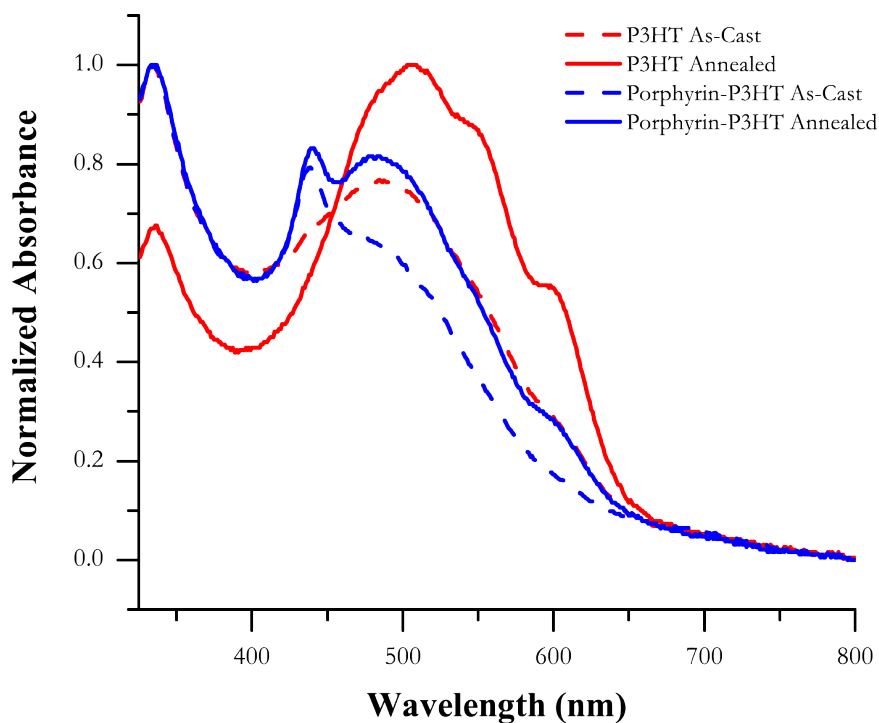


**Figure 4.5:** UV-Vis spectra of as-cast (dashed) and thermally annealed (solid) thin films of P3HT (red) and porphyrin-capped P3HTs (blue).

#### 4.3.4 X-Ray Diffraction

As previously stated, one of the major problems when incorporating porphyrins into BHJ films is that porphyrin crystals tend to form. Porphyrin crystals are problematic since they act as recombination centers that decrease the PCE of the resulting device. X-ray diffraction measurements were performed to examine the extent to which porphyrin-crystals formed. The diffraction patterns for thermally annealed films of 5k allyl-P3HT, 5k PP-P3HT, 50k P3HT, mono hydroxyporphyrin, and a representative BHJ blend is shown in Figure 4.8. As expected, the measurements of the THTP exhibit a strong peak at  $9.5^\circ$  that corresponds to diffraction angle of stacking between the porphyrin macrocycles. The absence of this diffraction peak in the neat PP-P3HT and BHJ film confirms that the P3HT chain is successfully preventing any porphyrin crystal formation.

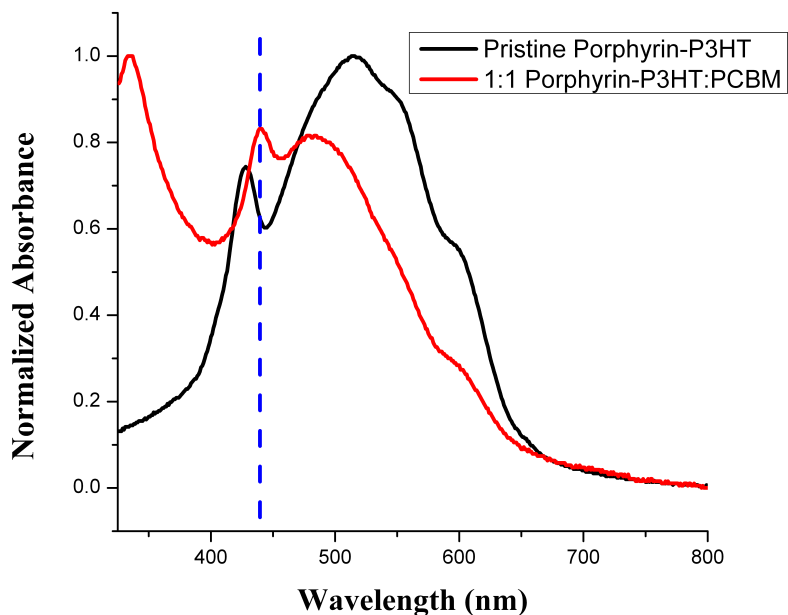


**Figure 4.6:** UV-Vis spectra for neat PP-P3HT (black) and PP-P3HT/PCBM (red) thin films after thermal annealing at 165 °C for 15 min.

The diffraction patterns of the P3HT-containing films exhibit peaks at 5.5° and 11.0° that correspond to reflections of the 100 crystal structure of P3HT, which occurs across the hexyl chains of P3HT lamella. The P3HT films also contain a strong peak at 27.5° corresponding to the reflection of the 010 crystal structure of P3HT between the thiophene repeat units of adjacent chains. The diffraction peaks of the BHJ blend and the neat 50k P3HT are slightly offset in the x-direction from the allyl- and PP-P3HT films due to the high regioregularity and increased crystallinity of the 50k P3HT. The presence of the peak at 5.5° in the PP-P3HT film corresponding to the 100 crystal structure of P3HT suggests that the porphyrin end group is not hindering the crystallization of the P3HT chains. This is advantageous because the PP-P3HTs are designed to straddle donor/acceptor interfaces, rather than phase separate or crystallize. Therefore, these conjugates offer promise to increase charge separation from the PP-P3HT/PCBM interface to the domains of larger matrix P3HTs.



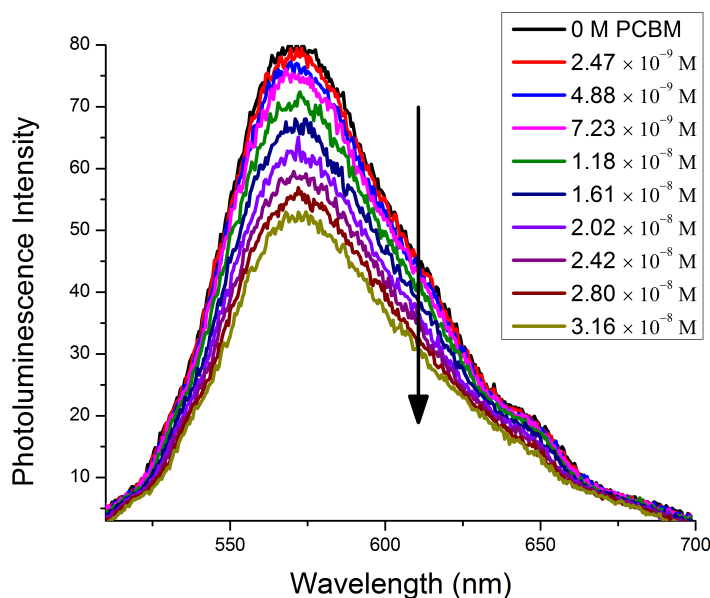


**Figure 4.7:** Fluorescence spectra for solutions of porphyrin-capped P3HT shown in black and solutions having increasing amounts of PCBM. The arrow indicates increasing PCBM concentration.

### 4.3.5 Differential Scanning Calorimetry

Differential scanning calorimetry (DSC) was used to investigate the effect of porphyrin-functionalization of P3HT on the thermal properties. The allyl-P3HT was analyzed as a benchmark, and it shows a  $T_m$  of 189.4 °C. This is consistent with reports of  $T_m$  of other low molecular weight P3HTs.<sup>75</sup> After porphyrin functionalization, the  $T_m$  decreases to 181.8 °C, which suggests that the porphyrin macrocycle disrupts the ability of P3HT chains to crystallize. DSC measurements of P3HT/PCBM blends containing different levels of the allyl- and porphyrin-terminated P3HTs also were made, which allow the effects of the PP-P3HT additive to be compared. The allyl- and porphyrin-terminated P3HTs were incorporated into BHJ films at loading levels up to 20% by wt. while maintaining a 1:1 ratio of total P3HT:PCBM. Table 4.2 summarizes the  $T_m$  values extracted from the DSC measurements. The crystalline fraction of P3HT,  $W_c$ , was calculated for each sample

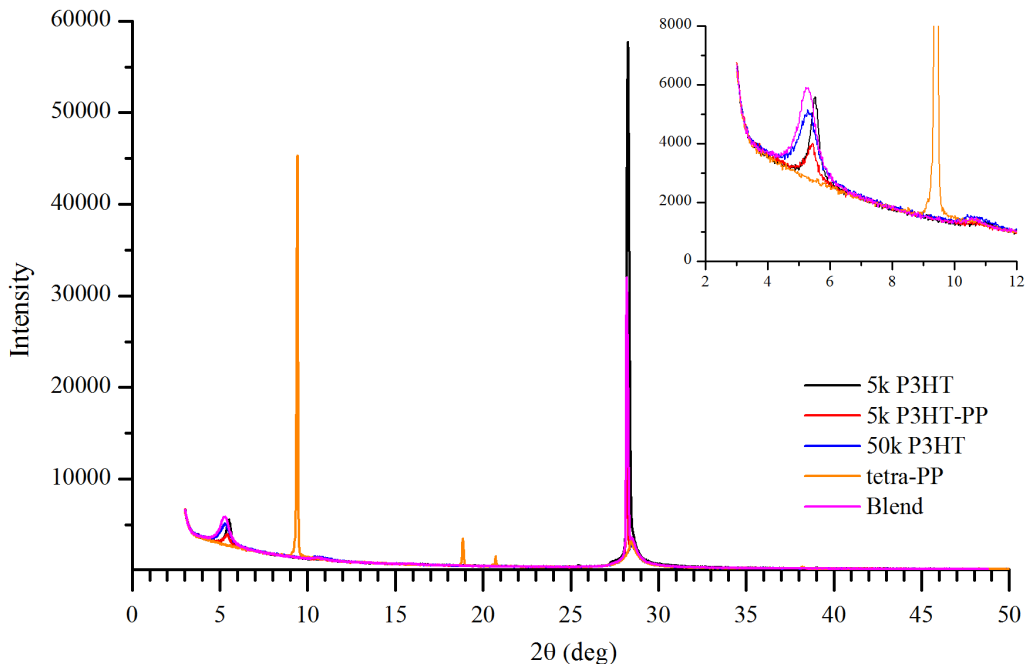


**Figure 4.8:** 1-D diffraction patterns for 5k allyl-P3HT (black), 5k PP-P3HT (red), 50k P3HT (blue), THTP (orange), and a representative BHJ blend (magenta). The inset is zoomed-in to show the 2–12 ° angles where crystallization peaks of P3HT and porphyrin rings are observed at 5.5° and 9.5°, respectively.

using Equation 1.10, where values of 37 and 99 J/g for  $\Delta H_m$ . These values bracket values often reported in literature,<sup>82,84</sup> and results are reported as  $W_{c,37}$  and  $W_{c,99}$ , respectively, in Table 4.2.

The control blend containing no PP-P3HT or allyl-P3HT additive featured 22.5% P3HT crystallinity and an average  $T_m$  of 186 °C. Interestingly, the sample containing 1% of the allyl-terminated P3HT had the highest  $T_m$  of the additive-containing samples. Any further increase in the loading level of the allyl-P3HT additive resulted in slight decreases in  $T_m$  compared to the control sample. For the porphyrin-terminated P3HTs, slight decreases in P3HT crystallinity are observed when PP-P3HTs are incorporated at all loading levels, except for the 10% loading, where a slight increase occurs. Admittedly, after multiple measurements of BHJ blends containing the allyl- and PP-P3HT additives, the recorded  $T_m$ s correspond to a change of at most

**Table 4.2:** Thermal properties obtained via DSC measurements of various BHJ blends as a function of allyl-P3HT and PP-P3HT loading level. Specifically, melting temperature ( $T_m$ ) and fraction of crystalline P3HT,  $W_{c,37}$  and  $W_{c,99}$ , are reported using 37 and 99 J g<sup>-1</sup> for  $\Delta H_m$ , respectively.

Sample	Loading	$T_m$	$\Delta H_m$	$W_{c,37}$ <sup>82</sup>	$W_{c,99}$ <sup>84</sup>
	wt.%	°C	J/g	%	%
Control	–	186.1	8.34	22.5	8.43
allyl-P3HT	1	209.4	9.43	25.5	9.53
	5	183.4	8.05	21.8	8.13
	10	184.7	7.49	20.2	7.57
	20	182.1	8.15	22.0	8.23
	PP-P3HT	1	182.2	6.85	18.5
	5	181.1	7.18	19.4	6.92
	10	179.6	8.74	23.6	8.83
	15	180.8	7.80	21.1	7.88
	20	181.0	5.22	14.1	5.27

2% in the total crystalline P3HT in each sample. Despite reducing the crystallization of the low MW P3HT chains to which they are attached in pure samples as measured by XRD, when incorporated into BHJ films containing higher MW P3HT ( $\approx 50$  kg/mol), the PP-P3HTs appear to have a negligible effect on P3HT crystallinity. As discussed previously, this is critical for ensuring that the good charge mobility properties of P3HT are not disrupted. No evidence for melting of PCBM crystals was observed in any of the collected DSC thermograms.

DSC was used to examine the miscibility of the P3HT additives with PCBM before and after attachment of the porphyrin end groups. By adding small amounts of PCBM to allyl- and PP-P3HTs, it is possible to deduce the miscibility of each additive in PCBM by measuring changes in the  $T_m$ . The data collected from these measurements is summarized in Table 4.3. The pure allyl-terminated P3HT sample exhibited a  $T_m$  of 189.4 °C, which is significantly higher than the  $T_m$  of 181.8 °C that was measured for the pure PP-P3HT sample. This difference suggests that the PP-P3HTs are less ordered in the solid state than the allyl-P3HTs. Upon addition of PCBM, the melting

temperature of the allyl-P3HTs changes from 189.4 °C for the pure sample to 182.0 °C for the sample containing 20% PCBM. For samples with PP-P3HT additive, the melting temperature decreases from 181.8 °C for the pure sample to 160.7 °C at 20% loading of PCBM. The large differences in the  $T_m$  observed between the PP-P3HT and allyl-P3HT samples with increasing PCBM loading suggest that PCBM is interacting more strongly with PP-P3HTs. Since these two polymers only differ in end group composition, this increase in interaction is attributed to the porphyrin end group.

**Table 4.3:** Melting temperatures determined via DSC for pure allyl-P3HT and PP-P3HT, and as a function of increasing weight fractions ( $\phi_{PCBM}$ ) of PCBM.

Sample	$\phi_{PCBM}$	$T_m$ (°C)
allyl-P3HT	–	189.4
2%PCBM	0.0078	188.8
5%PCBM	0.0201	187.9
10%PCBM	0.0424	186.3
20%PCBM	0.0953	181.2
PP-P3HT	–	181.8
2%PCBM	0.0078	180.4
5%PCBM	0.0201	178.0
10%PCBM	0.0424	173.1
20%PCBM	0.0953	160.7

The Flory-Huggins interaction parameter was calculated for each blend to quantify the impact of these interactions on phase behavior. These calculations are based on melting-point depression theory and are discussed in more detail in Section 1.5.5. Plots of  $(1/T_m - 1/T_m^\circ)$  as a function of  $\phi$  are shown in Figure 4.9 for the allyl and porphyrin-terminated P3HTs. Fitting of this data using the relationship shown in Equation 4.1, where  $\chi$  is the only adjustable parameter.

$$\frac{1}{T_m} - \frac{1}{T_m^\circ} = \frac{R}{\Delta H_f} \frac{\nu_m}{\nu_s} [\phi_s - \chi\phi_s^2] \quad (4.1)$$

Using this analysis,  $\chi$  values of 0.68 and 0.38 describing the miscibility of allyl-P3HT and PP-P3HT, respectively, in PCBM were calculated. The results for the

allyl-P3HT are in the range with previous measurements of  $\chi$  for P3HTs.<sup>75,90</sup> The significant drop in  $\chi$  of the PP-P3HT indicates that the porphyrin end group is improving miscibility due to increasing interactions with PCBM compared to the allyl-P3HTs. This reduction in  $\chi$  is perhaps the most telling aspect of this study because it encapsulates the significant role that the porphyrin end group plays in determining the interaction with PCBM nanoparticles.

These calculations of  $\chi$  appear to align with the melting temperatures recorded by DSC measurements. However, it should be noted that the  $\chi$  values are extremely sensitive to small changes in the volume fraction of PCBM and the recorded  $T_m$ . Other investigations consistently report that accurate values of  $T_m$  for similar materials, i.e. various P3HTs with PCBM, can be obtained by using slow cooling rates of 1–2 °C/min. One limitation in our calculation of  $\chi$  is that the DSC used in my measurements was unable to perform consistently at these slower cooling rates, which were limited to 5 °C/min. As such, these values represent decent approximations of  $\chi$  for comparison purposes; however, their accuracy may be limited by the DSC instrument’s ability to approach the  $T_m$  using a slower cooling rate.

### 4.3.6 Device Performance

Current-voltage curves for PP-P3HT containing devices are shown in Figure 4.10 under light and dark conditions. The dark curves of the PP-P3HT containing devices are steeper than the control devices under positive bias, which is indicative of a higher shunt resistance. The diode currents measured at 0 V are lower for the PP-P3HT containing devices, which also suggests that the PP-P3HTs are increasing the resistance of the devices. Performance data extracted from six devices containing the PP-P3HT additives are shown in Table 4.4 for measurements made while illuminated. Two significant traits are immediately apparent for the illuminated current-voltage measurements: First, there is the significant increase in the  $J_{SC}$ , from 7.88  $mA/cm^2$  for the control to 10.48  $mA/cm^2$  of the device containing 1% loading of the PP-P3HT.

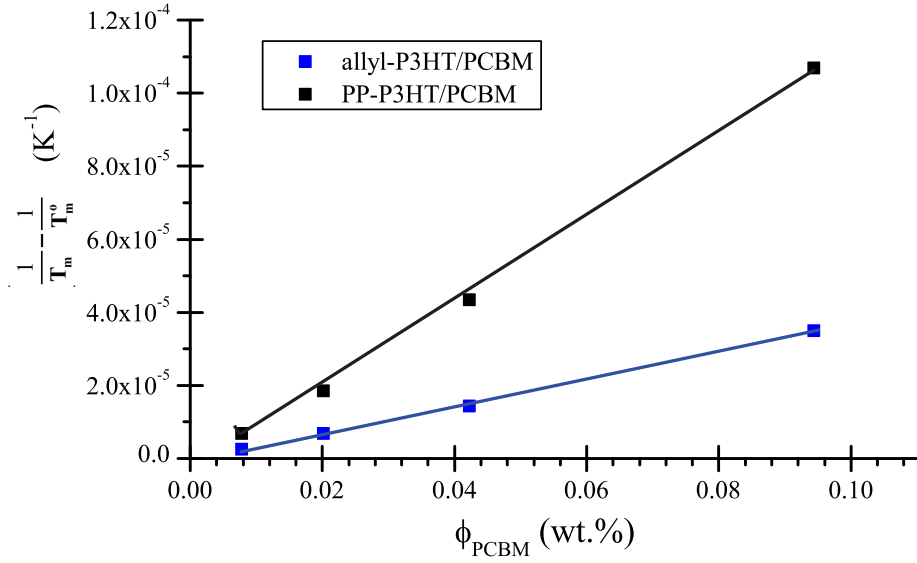


**Figure 4.9:** Plots of  $(1/T_m - 1/T_m^{\circ})$  as a function of  $\phi_{PCBM}$  used to calculate  $\chi$ , the Flory Huggins interaction parameter, for PP-P3HT (black) and allyl-P3HT (blue). The solid lines represent the fits used to describe the data by the model.

Second, the reduced “squareness” of the J-V curves indicate that the addition of PP-P3HTs drastically decreases the fill factor (FF) of the devices; furthermore, this effect becomes more severe with increasing loading level. The FF of the control device was measured as 0.47, whereas the FF for the PP-P3HT containing devices decreased to 0.19 at a loading level of 20% by wt. The  $V_{OC}$  values of the PP-P3HT containing devices remained consistent at  $\approx 0.55$ – $0.57$  V across all loading levels, however slight decreases occurred at loading levels of 10 and 20%. Plots of the  $V_{OC}$  and FF as a function of PP-P3HT loading level are shown in Figures B.9 and B.10 of Appendix B.4.4.

Scatter plots of the PCE and  $J_{SC}$  as a function of PP-P3HT loading level are presented Figure 4.11. Together, the resemblance of the two profiles highlight the similarity between the two performance characteristics. With the exception of the device containing 1% loading, all of the PP-P3HT containing devices featured a

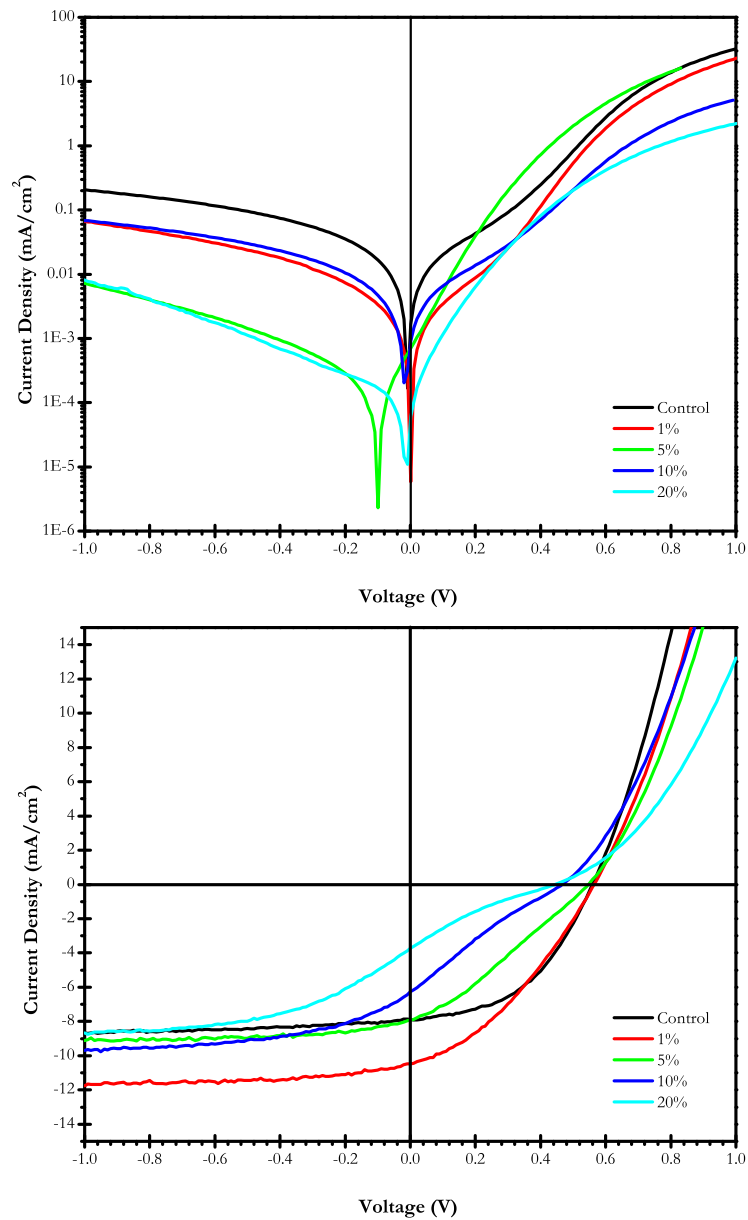


**Figure 4.10:** Current density versus voltage plots for devices containing increasing amounts of PP-P3HT additive under dark (top) and illuminated (bottom) conditions.

**Table 4.4:** Performance characteristics of BHJ devices containing porphyrin-capped P3HTs at different levels and a control device featuring no additive.

Additive	Loading	$J_{SC}$	$V_{OC}$	FF	PCE
	wt. %	$mA/cm^2$	$V$		%
<b>Control</b>	–	$7.88 \pm 0.03$	$0.57 \pm 0.01$	$0.47 \pm 0.01$	$2.07 \pm 0.01$
<b>PP-P3HT1</b>	1.0	$10.48 \pm 0.03$	$0.57 \pm 0.01$	$0.35 \pm 0.01$	$2.10 \pm 0.01$
<b>PP-P3HT5</b>	5.0	$7.93 \pm 0.04$	$0.55 \pm 0.01$	$0.29 \pm 0.01$	$1.25 \pm 0.01$
<b>PP-P3HT10</b>	10.0	$6.27 \pm 0.03$	$0.47 \pm 0.01$	$0.22 \pm 0.01$	$0.64 \pm 0.01$
<b>PP-P3HT20</b>	20.0	$3.85 \pm 0.03$	$0.45 \pm 0.01$	$0.19 \pm 0.01$	$0.33 \pm 0.01$

decreased PCE compared to the control. For the device containing 1% loading of PP-P3HTs, the performance was slightly improved over the control—the PCE increases from 2.07 to 2.1%. The increase in PCE at this loading level appears to be exclusively driven by an increase in the  $J_{SC}$ . Exceeding a loading level of 1% results in a decreased  $J_{SC}$ , which results in a similar trend in the PCE data.

The lackluster performance of these devices is currently attributed to the design of the linkage. Specifically, the presence of the Si atom and loss of conjugation in the linkages between the porphyrin end group and P3HT chain probably leads to the poor performance. It is known that Si by itself acts as an electronic insulator. Driven by the strong interactions between PCBM and PP-P3HTs, and the fact that low MW additives tend to migrate to the donor/acceptor interface as discussed in Chapter 3, it stands to reason that the PP-P3HT additives likely straddle the donor/acceptor interfaces. As the donor/acceptor interface is responsible for the separation of electrons and holes generated by the donor polymer, the device performance is extremely sensitive to the presence of these insulating Si atoms and loss of conjugation. This interpretation explains the increased resistance of the PP-P3HT containing devices under dark conditions and the reduction in FF and  $J_{SC}$  of the illuminated JV measurements. The increased performance of the sample containing a 1wt.% loading of the PP-P3HTs is currently explained as follows: The addition of a minor amount of PP-P3HT is sufficient to impose morphological changes at the



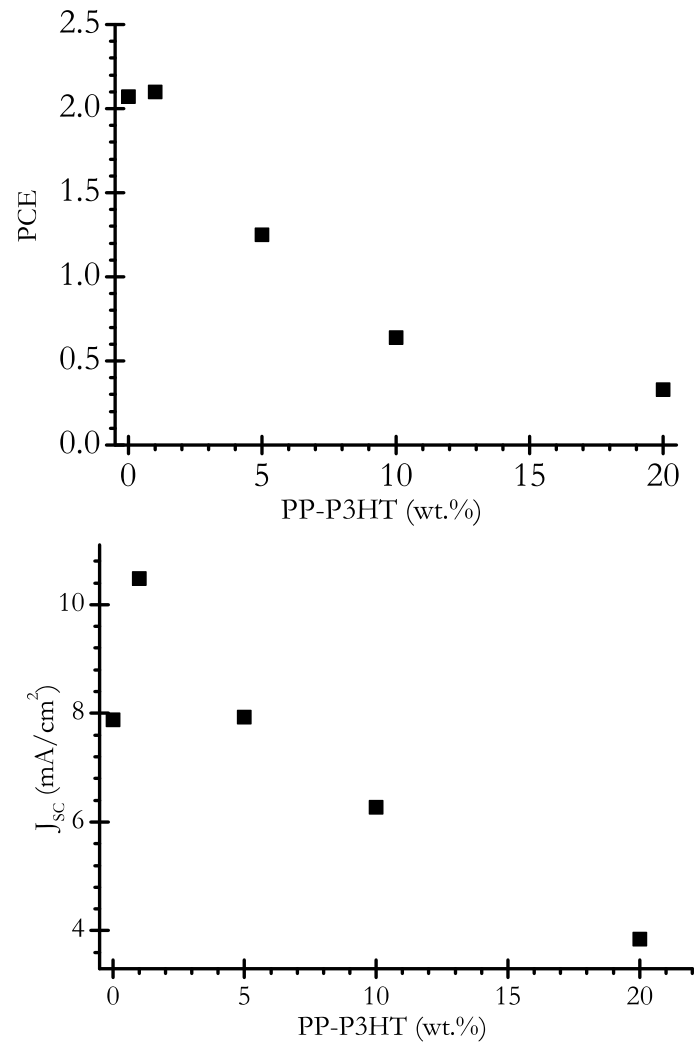


**Figure 4.11:** Plots for the PCE (top) and J<sub>sc</sub> (bottom) as a function of PP-P3HT additive loading level.

donor/acceptor interface, yet low enough that the interfaces are not overwhelmed by the Si recombination centers. The remarkably high  $J_{SC}$  offers a glimpse of the potential of porphyrins to increase photon absorption and impose beneficial morphological changes that will lead to improved device performances when present as a carefully designed surfactant-like additive.

## 4.4 Conclusions

This work presents a reliable post-polymerization modification strategy to install porphyrin macrocycles at the P3HT chain ends. Proton shifts in the  $^1\text{H-NMR}$  and a broadening of the SEC elugram offer strong evidence that the porphyrin was successfully coupled at the P3HT chain end. Coupling was also confirmed by the presence of the Soret and Q absorption bands due to the porphyrin in UV-Vis spectroscopy measurements performed on the purified PP-P3HTs in solution and thin film. UV-Vis spectroscopy and XRD measurements confirmed that the attachment of the porphyrin moiety at the chain end did not prevent the crystallization of the P3HT chains to which the porphyrin is attached. These outcomes are important as these crystalline structures increase the hole conductivity through the P3HT domains. Fortunately, the lack of reflections corresponding to porphyrin crystals in the PP-P3HT diffraction pattern confirm that the tethering and presence of the P3HT chain is sufficient to completely eliminate porphyrin crystallization.

DSC measurements of BHJ films containing the PP-P3HT additives resulted in negligible changes in the total amount of crystalline P3HT content. Additionally, reductions in melting temperature and fluorescence intensity indicate that the porphyrin centers interact strongly with PCBM in solution and thin films. These strong interactions resulted in a decrease in the Flory-Huggins interaction parameter,  $\chi$ , describing the miscibility with PCBM, from 0.68 for allyl-P3HT to 0.38 for the PP-terminated P3HTs. Despite these promising film properties, incorporating the PP-P3HTs into devices resulted in decreases in the device performance with the exception

of devices containing a 1% loading, which performed slightly better than the control. It is currently postulated that this increase in PCE is due to a slight increase in photon absorption and an enhancement in BHJ film morphology. Any further addition of the PP-P3HT lead to a significant drop in the  $J_{SC}$  and FF of the device, which suggest that the donor/acceptor interface is overwhelmed by the presence of PP-P3HTs acting as recombination centers. This may not be unexpected, as interfaces can be saturated by a small amount of surfactant.

Due to the aliphatic groups and Si atom, the PP-P3HTs in their current form possess a suboptimal design that limits their performance when incorporated into devices. Nevertheless, the presence of the porphyrin group at the P3HT chain end resulted in strong interactions between P3HT and PCBM, which points to their potential to modify internal interfaces of BHJ films. These results not only confirm the potential of porphyrins to affect BHJ morphology through strong electronic interactions, but also underscore the sensitive links between the chemical design of OPV materials and effect on OPV devices.

## 4.5 Experimental

### 4.5.1 Synthesis of THTP

5-(4-hydroxyphenyl)-10,15,20-tristolyloporphyrin (THTP) was synthesized following literature procedures. In short, and as shown in Figure 4.1, functionalized aldehydes were added to a 3-neck round bottom flask equipped with a Teflon stir bar and dissolved in propionic acid. The resulting solution was then heated to reflux and freshly distilled pyrrole (4 equiv.) was added dropwise. During the addition, the solution turned from clear to dark. After completing the addition of pyrrole, the solution was stirred at reflux for 30 min. The reaction mixture was then allowed to cool to room temperature, before filtering and washing with methanol. The crude purple solid was purified via column chromatography using DCM as the mobile phase,

and the THTP was collected in the second fraction. The THTP was further purified via recrystallization from a CH<sub>2</sub>Cl<sub>2</sub>/MeOH mixture. <sup>1</sup>H-NMR and UV-Vis spectra agreed with literature reports.

### 4.5.2 Synthesis of allyl-P3HT

Polymer molecular weight was measured as  $M_n = 5,800$  g/mol with a PDI = 1.13 using a Tosoh EcoSEC GPC and HPLC grade THF as the mobile phase. Allyl end-group composition was confirmed using a Voyager Matrix-Assisted Laser Desorption Ionization Time of Flight Mass Spectrometer (MALDI-TOF MS) in which THF solutions of P3HT and trans-2[3-(4-tert-butylphenyl)-2-methyl-2-propenylidene]malonitrile were used to spot the MALDI target. The P3HTs used in this work contained 90% mono-allyl, 3% di-allyl, and 7% Br/Br terminated end groups. NMR measurements were performed on a Varian Mercury Vx 300 MHz using deuterated chloroform to determine polymer regioregularity (91% rr) and molecular weight ( $M_w=3,000$  g/mol).

### 4.5.3 Synthesis of PP-P3HT

While maintaining inert conditions, a benzene solution containing imidazole and THTP (2:1 by mole THTP:P3HT) was added to dry monochlorosilane-functionalized P3HTs. After ensuring complete dissolution of the P3HT, the reaction was allowed to stir for 6 h. The reaction was terminated by precipitation into copious amounts of MeOH. The precipitated mixture was left at 2°C overnight. Then, the precipitate was collected and soxhlet extractions in MeOH and acetone were performed to remove any Karsteadts catalyst, imidazole, and untethered porphyrin. Finally, the purified product was extracted using CHCl<sub>3</sub>.

### 4.5.4 Uv-Vis and Fluorescence Spectroscopy

UV-Vis spectroscopy measurements were performed using a Thermo Scientific Evolution 600 spectrophotometer. A range of 325–800 nm was scanned. Fluorescence

spectroscopy measurements were made using a Perkin Elmer LS-55 fluorescence spectrophotometer. An excitation of 450 nm was used, and the emission scanned from 500-700 nm. Solutions used for UV-Vis and fluorescence studies were prepared using HPLC grade chloroform (Fisher Scientific). UV-Vis measurements of films were acquired using glass substrates that were cleaned via the piranha cleaning process outline in Section A.3. Allyl- and PP-P3HT films were cast from chloroform solution via spin-coating at 1,000 rpm for 30 s.

#### **4.5.5 Differential Scanning Calorimetry**

Measurements were performed using a TA Instruments (TA Q2000), and an Indium standard was used for temperature and heat flow calibration. Each heating and cooling cycle was performed at 5 °C/min over the temperature range of 0 to 280 °C. Samples mimicking BHJ thin films were prepared by drop-casting from chloroform solutions into warm DSC pans, which facilitates quick evaporation of solvent. Using this method, sample masses consistently ranged from 5 to 10 mg.

#### **4.5.6 X-Ray Diffraction**

All silicon substrates were cleaned prior to film preparation by immersing the silicon substrates in piranha acid solution, as described in Section A.3. Films were cast from chlorobenzene solution via spin coating at 1,000 rpm for 30 sec followed by spinning at 1,500 rpm for 2 min. After casting, films were annealed under vacuum at 165 °C for 15 min and then allowed to cool to room temperature. X-ray diffraction measurements were collected using an X'Pert Model 2000 X-ray diffractometer located in the Center for Nanophase Material Science at Oak Ridge National Laboratory.

#### **4.5.7 Device Performance**

Photovoltaic devices were fabricated and tested as previously described.<sup>169,180</sup> Briefly, indium tin-oxide (ITO) coated glass substrates were cleaned by sequential rinsing

with 1% Aquet detergent solution and water, acetone, and isopropanol, and dried using a stream of filtered N<sub>2</sub>. The substrates then were cleaned via UV ozonolysis for 30 min. After cleaning, anode buffer layers consisting of a 1:6 blend of polyethylenedioxythiophene:polystyrenesulphonate (PEDOT/PSS) at 1.3wt% in H<sub>2</sub>O were spin-coated onto the ITO coated glass at 1,000 rpm for 1 min. These substrates were then thermally annealed at 110 °C for 15 min to remove any residual water from the polymer thin film. The samples were transferred to a nitrogen-filled glove box where P3HT and PCBM were deposited by spin coating from a chlorobenzene solution at 1,000 rpm for 3 min. The ratio of P3HT and PCBM was held constant at 1:1 for all BHJ thin films, and in cases where low MW P3HT additives were used, their loading was based on the mass of the total P3HT content. Device fabrication was completed by applying aluminum cathode layers of nominally 1 μm thick atop each active layer film via metal vapor deposition. While remaining in the N<sub>2</sub>-filled glove box, each device was annealed at 165 °C for 15 min and tested under AM 1.5 G 100 mW/cm<sup>2</sup> illumination. Current-voltage characteristics were measured and recorded using a Keithley 2636A source meter. Devices were assembled at Pennsylvania State University.

## Chapter 5

# Summary, Conclusions, and Future Work

The fact that PCEs greater than 17% have been reported at single wavelengths for recently developed low band gap donor polymers is promising for realizing OPV devices exceeding 20% efficiency at the commercial scale.<sup>210</sup> As new donor polymers are designed, recognizing and understanding how to manipulate their properties will be critical for maximizing their performance in OPV devices. At its core, my dissertation focuses on applying synthetic techniques to tailor the design of donor polymers to increase control over BHJ morphology, and by extension, improve device performance.

The ability to efficiently extract charges at electrode interfaces is important for maximizing the performance of organic solar cells. Polymer brushes comprised of P3HT donor-type polymer as an ABL is attractive as it provides a pathway to extract charges in a way that is ohmically aligned with the donor polymer of the BHJ film. It also offers chemical stability. In morphological studies of P3HT brushes, I proved that these layers have a profound impact on the morphology of the BHJ film. NR shows that severe migration of PCBM occurred during thermal annealing, resulting in as much as 60% by volume of PCBM at the anode interface. The degree to which the vertical distribution of PCBM increased is dependent on the grafting density of the polymer brush, which was controlled by changing the annealing temperature used after deposition of the P3HT brushes. Although PCBM-rich domains are not ideal at the anode interface where holes are collected, these results exemplify the potential for polymer brushes to affect BHJ film morphology. Because the P3HT brushes are not miscible with the high molecular weight P3HT matrix chains, crystallization of P3HT occurs away from the anode interface, leaving an amorphous region at the interface into which PCBM can penetrate. Overcoming this thermodynamic incentive forming at the anode interface would require a donor-type polymer brush system capable of crystallizing, or at the very least, one that rejects PCBM more readily than the matrix donor polymer. An alternative, and in my opinion more interesting approach, is to use polymer brushes comprised of conjugated acceptor-type polymers at the cathode interface in an inverted device architecture. In this device structure, the



polymer brushes would provide the same thermodynamic incentives to establish BHJ film morphology except that the segregation of fullerenes could be directed to the more favorable cathode interface.

Despite the array of BHJ additives that have been investigated to enhance OPV device performance, little attention has been given to understanding the fundamental mechanisms that govern their behavior. My dissertation work addresses how the addition of low MW P3HTs affect P3HT/PCBM BHJ films. In these studies, I demonstrated that the simple addition of low MW P3HTs sharing identical monomer structure and end group functionality to the matrix P3HTs results in enhanced device performance. Increases in PCE up to 34% were achieved over an unmodified control for P3HT additives of 3 different molecular weights. Based on results from X-ray scattering and TEM measurements, these additives appear to increase performance by migrating to and stabilizing the donor-acceptor interface in the BHJ films. Contact angle measurements and molecular dynamics simulations suggest that these additives are able to interact with PCBM during thermal annealing due to the similar size between the low MW P3HTs and PCBM. Perhaps more important is the identification of critical loading levels for each additive that, when exceeded, resulted in coarsening of BHJ film morphology, as indicated by SAXS measurements. Recognizing that this critical loading level is inversely proportional to the size of the P3HT additive establishes a fundamental link between optimizing the size and loading level of new additives. Finally, this approach also is amenable for use with new low band gap donor polymers since it is based on the synthesis of low MW versions of the matrix donor polymer.

The inclusion of porphyrins as a means to enhance the performance of OPVs is an emerging trend in the field. Porphyrins strongly absorb light, have favorable electronic properties, and strongly interact with PCBM acceptors. Generally these strategies have focused on the addition of small molecule porphyrins with pendant groups decorating the macrocycle to prevent their crystallization, but this approach does not strategically influence the morphology of the BHJ film. Attaching phenylporphyrin

moieties at the end of low MW P3HT chains offers two primary advantages: First, the presence of the P3HT chains is sufficient to prevent the formation of porphyrin crystals that function as recombination centers. Second, and perhaps the unique feature of my effort, is that the porphyrin groups are added using a post-polymerization modification strategy that enables extensive characterization of the porphyrin and P3HT before coupling, as well as the conjugate. Building on the principles I learned from my investigations of low MW P3HT additives, the low MW of the porphyrin-capped P3HTs provides an entropic incentive for the porphyrin-P3HT conjugate to be present at donor/acceptor interfaces within the BHJ film where PCBM and porphyrin can interact. UV-Vis and fluorescence measurements revealed that the porphyrin readily coordinates with PCBM in solution and in films without inhibiting crystallization of the thiophene rings of P3HT, which is crucial for not degrading its desirable properties. XRD and DSC measurements confirmed the presence of P3HT crystals and a lack of porphyrin crystallization. The most convincing evidence of improved PCBM coordination with the PP-P3HTs was the reduction of the Flory Huggins interaction parameter  $\chi$ , from  $\approx 0.68$  to 0.38 as determined from melting temperatures measured by DSC. With the exception of the 1% loading of PP-P3HTs, the power conversion efficiencies of devices fabricated with P3HT-PP additives were lower than an unmodified control. For the 1% loading of PP-P3HTs, the improvements were minor compared to those obtained from the low MW P3HTs discussed in Chapter 3. This result is possibly explained by the presence of the Si atom between the porphyrin and the P3HT that acts as an insulator, which is why drastic decreases in the  $J_{SC}$  and FF are observed with higher loading levels of the additives. With this context in mind, one immediately apparent extension of this work would entail using a different coupling strategy. Ideally it would be important to maintain the  $\pi$  conjugation.

# Bibliography

- [1] Fu, R.; James, T.L.; Woodhouse, M. Economic Measurements of Polysilicon for the Photovoltaic Industry: Market Competition and Manufacturing Competitiveness. *IEEE Journal of Photovoltaics*. **2015**. *5*, 515–524.
- [2] King, R.R.; Law, D.C.; Edmondson, K.M.; Fetzer, C.M.; Kinsey, G.S.; Yoon, H.; Sherif, R.a.; Karam, N.H. 40% Efficient Metamorphic GaInPGaInAsGe Multijunction Solar Cells. *Applied Physics Letter*. **2007**. *90*.
- [3] Green, M.A.; Emery, K.; Hishikawa, Y.; Warta, W.; Dunlop, E.D. Solar cell efficiency tables (version 44). *Progress Photovoltaics Research Applications*. **2014**. *22*, 701–710.
- [4] Li, G.; Zhu, R.; Yang, Y. Polymer Solar Cells. *Nature Photonics*. **2012**. *6*, 153–161.
- [5] Zhao, J.; Li, Y.; Yang, G.; Jiang, K.; Lin, H.; Ade, H.; Ma, W.; Yan, H. Efficient Organic Solar Cells Processed from Hydrocarbon Solvents. *Nature Energy*. **2016**. *1*, 15027.
- [6] Horowitz, G. Organic Semiconductors for New Electronic Devices. *Advanced Materials*. **1990**. *2*, 287–292.
- [7] Minami, N.; Sasaki, K.; Tsuda, K. Improvement of the Performance of Particulate Phthalocyanine Photovoltaic Cells by the Use of Polar Polymer Binders. *Journal of Applied Physics*. **1983**. *54*, 6764–6766.
- [8] Karasz, F.; Capistran, J.; Gagnon, D.; Lenz, R. High Molecular Weight Polyphenylene Vinylene. *Molecular Crystals and Liquid Crystals*. **1985**. *118*, 327–332.
- [9] Sariciftci, N.; Smilowitz, L.; Heeger, A.J.; Wudl, F. Photoinduced Electron Transfer from a Conducting Polymer to Buckminsterfullerene. *Science*. **1992**. *258*, 1474–1476.

- [10] Yu, G.; Gao, J.; Hummelen, J.C.; Wudl, F.; Heeger, A.J. Polymer Photovoltaic Cells: Enhanced Efficiencies via a Network of Internal Donor-Acceptor Heterojunctions. *Science*. **1995**. *270*, 1789.
- [11] Yin, W.; Dadmun, M. A New Model for the Morphology of P3HT/PCBM Organic Photovoltaics from Small-Angle Neutron Scattering: Rivers and Streams. *ACS Nano*. **2011**. *5*, 4756–4768.
- [12] Zhang, F.L.; Gadisa, A.; Inganas, O.; Svensson, M.; Andersson, M.R. Influence of Buffer Layers on the Performance of Polymer Solar Cells. *Applied Physics Letters*. **2004**. *84*, 3906.
- [13] Po, R.; Carbonera, C.; Bernardi, A.; Camaioni, N. The Role of Buffer Layers in Polymer Solar Cells. *Energy Environ. Sci*. **2011**. *4*, 285.
- [14] Steim, R.; Kogler, F.R.; Brabec, C.J. Interface Materials for Organic Solar Cells. *Journal of Materials Chemistry*. **2010**. *20*, 2499.
- [15] Vanlaeke, P.; Swinnen, A.; Haeldermans, I.; Vanhoyland, G.; Aernouts, T.; Cheyns, D.; Deibel, C.; DHaen, J.; Heremans, P.; Poortmans, J.; et al. P3HT/PCBM Bulk Heterojunction Solar Cells: Relation Between Morphology and Electro-Optical Characteristics. *Solar Energy Materials & Solar Cells*. **2006**. *90*, 2150–2158.
- [16] Kim, Y.; Choulis, S.a.; Nelson, J.; Bradley, D.D.C.; Cook, S.; Durrant, J.R. Device Annealing Effect in Organic Solar Cells with Blends of Regioregular Poly(3-hexylthiophene) and Soluble Fullerene. *Applied Physics Letters*. **2005**. *86*, 1–3.
- [17] Kim, Y.; Choulis, S.a.; Nelson, J.; Bradley, D.D.C.; Cook, S.; Durrant, J.R. Composition and Annealing Effects in Polythiophene/Fullerene Solar Cells. *Journal of Materials Science*. **2005**. *40*, 1371–1376.

- [18] Chen, H.; Hegde, R.; Browning, J.; Dadmun, M.D. The Miscibility and Depth Profile of PCBM in P3HT: Thermodynamic Information to Improve Organic Photovoltaics. *Phys Chem Chem Phys.* **2012.** *14,* 5635–5641.
- [19] Liu, H.J.; Jeng, U.S.S.; Yamada, N.L.; Su, A.C.; Wu, W.R.; Su, C.J.; Lin, S.J.; Wei, K.H.; Chiu, M.Y. Surface and Interface Porosity of Polymer/Fullerene-Derivative Thin Films Revealed by Contrast Variation of Neutron and X-ray Reflectivity. *Soft Matter.* **2011.** *7,* 9276.
- [20] Parnell, a.J.; Dunbar, A.D.F.; Pearson, A.J.; Staniec, P.a.; Dennison, A.J.C.; Hamamatsu, H.; Skoda, M.W.a.; Lidzey, D.C.; Jones, R.a.L. Depletion of PCBM at the Cathode Interface in P3HT/ PCBM Thin Films as Quantified via Neutron Reflectivity Measurements. *Advanced Materials.* **2010.** *22,* 2444–2447.
- [21] Lee, K.H.; Zhang, Y.; Burn, P.L.; Gentle, I.R.; James, M.; Nelson, A.; Meredith, P. Correlation of Diffusion and Performance in Sequentially Processed P3HT/PCBM Heterojunction Films by Time-Resolved Neutron Reflectometry. *Journal of Material Chemistry C.* **2013.** *1,* 2593.
- [22] Guralnick, B.W.; Kirby, B.J.; Majkrzak, C.F.; MacKay, M.E. Morphological Characterization of Plastic Solar Cells Using Polarized Neutron Reflectivity. *Applied Physics Letters.* **2013.** *102,* 2011–2015.
- [23] Kiel, J.W.; Kirby, B.J.; Majkrzak, C.F.; Maranville, B.B.; Mackay, M.E. Nanoparticle Concentration Profile in Polymer-Based Solar Cells. *Soft Matter.* **2010.** *6,* 641–646.
- [24] Kiel, J.W.; Eberle, A.P.R.; Mackay, M.E. Nanoparticle Agglomeration in Polymer-Based Solar Cells. *Physical Review Letter.* **2010.** *105.*
- [25] Kohn, P.; Rong, Z.; Scherer, K.H.; Sepe, A.; Sommer, M.; Müller-Buschbaum, P.; Friend, R.H.; Steiner, U.; Hüttner, S. Crystallization-Induced 10-nm

- Structure Formation in P3HT/PCBM Blends. *Macromolecules*. **2013**. *46*, 4002–4013.
- [26] Chen, D.; Liu, F.; Wang, C.; Nakahara, A.; Russell, T.P. Bulk Heterojunction Photovoltaic Active Layers via Bilayer. *Nano Letters*. **2011**. *11*, 2071–2078.
- [27] Wu, W.R.; Jeng, U.S.; Su, C.J.C.H.J.; Wei, K.H.; Su, M.S.; Chiu, M.Y.; Chen, C.Y.; Su, W.B.; Su, C.J.C.H.J.; Su, A.C. Competition Between Fullerene Aggregation and Poly(3-hexylthiophene) Crystallization Upon Annealing of Bulk Heterojunction Solar Cells. *ACS Nano*. **2011**. *5*, 6233–6243.
- [28] Agostinelli, T.; Lilliu, S.; Labram, J.G.; Campoy-Quiles, M.; Hampton, M.; Pires, E.; Rawle, J.; Bikondoa, O.; Bradley, D.D.C.; Anthopoulos, T.D.; Nelson, J.; MacDonald, J.E. Real-Time Investigation of Crystallization and Phase-Segregation Dynamics in P3HT:PCBM Solar Cells During Thermal Annealing. *Advanced Functional Materials*. **2011**. *21*, 1701–1708.
- [29] Mauger, S.A.; Chang, L.L.; Friedrich, S.; Rochester, C.W.; Huang, D.M.; Wang, P.; Moule, A.J. Self-Assembly of Selective Interfaces in Organic Photovoltaics. *Advanced Functional Materials*. **2013**. *23*, 1935–1946. *Adv Funct Mater*.
- [30] Xue, B.; Vaughan, B.; Poh, C.h.; Burke, K.B.; Thomsen, L.; Stapleton, A.; Zhou, X.; Bryant, G.W.; Belcher, W.; Dastoor, P.C. Vertical Stratification and Interfacial Structure in P3HT:PCBM Organic Solar Cells. *Journal of Physical Chemistry C*. **2010**. *114*, 15797–15805. *J Phys Chem C*.
- [31] Germack, D.S.; Chan, C.K.; Hamadani, B.H.; Richter, L.J.; Fischer, D.a.; Gundlach, D.J.; DeLongchamp, D.M. Substrate-Dependent Interface Composition and Charge Transport in Films for Organic Photovoltaics. *Applied Physics Letters*. **2009**. *94*, 233303.
- [32] Germack, D.S.; Chan, C.K.; Kline, R.J.; Fischer, D.A.; Gundlach, D.J.; Toney, M.F.; Richter, L.J.; DeLongchamp, D.M. Interfacial Segregation in

- Polymer/Fullerene Blend Films for Photovoltaic Devices. *Macromolecules*. **2010**. *43*, 3828–3836. *Macromolecules*.
- [33] Keum, J.K.; Browning, J.F.; Xiao, K.; Shao, M.; Halbert, C.E.; Hong, K. Morphological Origin for the Stratification of P3HT: PCBM Blend Film Studied by Neutron Reflectometry. *Applied Physics Letters*. **2013**. *103*, 223301.
- [34] Orimo, A.; Masuda, K.; Honda, S.; Benten, H.; Ito, S.; Ohkita, H.; Tsuji, H. Surface Segregation at the Aluminum Interface of Poly(3-hexylthiophene)/Fullerene Solar Cells. *Applied Physics Letters*. **2010**. *96*, 9–12.
- [35] Pavlopoulou, E.; Fleury, G.; Deribew, D.; Cousin, F.; Geoghegan, M.; Hadziioannou, G. Phase Separation-Driven Stratification in Conventional and Inverted P3HT: PCBM Organic Solar Cells. *Orginal Electronics*. **2013**. *14*, 1249–1254.
- [36] Collins, B.a.; Tumbleston, J.R.; Ade, H. Miscibility, Crystallinity, and Phase Development in P3HT/PCBM Solar Cells: Toward an Enlightened Understanding of Device Morphology and Stability. *Journal of Physical Chemistry Letter*. **2011**. *2*, 3135–3145.
- [37] Chen, H.Y.; Yang, H.; Yang, G.; Sista, S.; Zadoyan, R.; Li, G.; Yang, Y. Fast-Grown Interpenetrating Network in Poly(3-hexylthiophene): Methanofullerenes Solar Cells Processed with Additive. *The Journal of Physical Chemistry C*. **2009**. *113*, 7946–7953.
- [38] Earmme, T.; Hwang, Y.J.; Subramaniyan, S.; Jenekhe, S.A. All-Polymer Bulk Heterojunction Solar Cells With 4.8% Achieved by Solution Processing From a Co-solvent. *Advanced Materials*. **2014**. *26*, 6080–5.
- [39] Kawano, K.; Sakai, J.; Yahiro, M.; Adachi, C. Effect of Solvent on Fabrication of Active Layers in Organic Solar Cells Based on Poly(3-hexylthiophene) and



- Fullerene Derivatives. *Solar Energy Materials and Solar Cells*. **2009**. *93*, 514–518.
- [40] Yao, Y.; Hou, J.; Xu, Z.; Li, G.; Yang, Y. Effects of Solvent Mixtures on the Nanoscale Phase Separation in Polymer Solar Cells. *Advanced Functional Materials*. **2008**. *18*, 1783–1789.
- [41] Miller, S.; Fanchini, G.; Lin, Y.Y.; Li, C.; Chen, C.W.; Su, W.F.; Chhowalla, M. Investigation of Nanoscale Morphological Changes in Organic Photovoltaics During Solvent Vapor Annealing. *Journal of Materials Chemistry*. **2008**. *18*, 306–312.
- [42] Tang, H.; Lu, G.; Li, L.; Li, J.; Wang, Y.; Yang, X. Precise Construction of PCBM Aggregates for Polymer Solar Cells via Multi-Step Controlled Solvent Vapor Annealing. *Journal of Materials Chemistry*. **2010**. *20*, 683–688.
- [43] Zhao, Y.; Xie, Z.; Qu, Y.; Geng, Y.; Wang, L. Solvent-Vapor Treatment Induced Performance Enhancement of Poly(3-hexylthiophene): Methanofullerene Bulk-Heterojunction Photovoltaic Cells. *Applied Physics Letters*. **2007**. *90*.
- [44] Lin, J.W.P.; Dudek, L.P. Synthesis and Properties of Poly (2, 5-thienylene). *Journal of Polymer Science: Polymer Chemistry Edition*. **1980**. *18*, 2869–2873.
- [45] Yamamoto, T.; Sanechika, K.; Yamamoto, A. Preparation of Thermostable and Electric-Conducting Poly (2, 5-thienylene). *Journal of Polymer Science: Polymer Letters Edition*. **1980**. *18*, 9–12.
- [46] Elsenbaumer, R.; Jen, K.Y.; Oboodi, R. Processible and Environmentally Stable Conducting Polymers. *Synthetic Metals*. **1986**. *15*, 169–174.
- [47] Maior, R.S.; Hinkelmann, K.; Eckert, H.; Wudl, F. Synthesis and Characterization of Two Regiochemically Defined Poly (Dialkylbithiophenes): A Comparative Study. *Macromolecules*. **1990**. *23*, 1268–1279.

- [48] Wei, Y.; Chan, C.C.; Tian, J.; Jang, G.W.; Hsueh, K.F. Electrochemical Polymerization of Thiophenes in the Presence of Bithiophene or Terthiophene: Kinetics and Mechanism of the Polymerization. *Chemistry of Materials*. **1991**. *3*, 888–897.
- [49] McCullough, R.D.; Lowe, R.D. Enhanced Electrical Conductivity in Regioselectively Synthesized Poly (3-alkylthiophenes). *Journal of the Chemical Society C*. **1992**, 70–72.
- [50] Chen, T.A.; Rieke, R.D. The First Regioregular Head-to-Tail Poly (3-hexylthiophene-2, 5-diyl) and a Regiorandom Isopolymer: Nickel Versus Palladium Catalysis of 2 (5)-bromo-5 (2)-(bromozincio)-3-Hexylthiophene Polymerization. *Journal of the American Chemical Society*. **1992**. *114*, 10087–10088.
- [51] Loewe, R.S.; Ewbank, P.C.; Liu, J.; Zhai, L.; McCullough, R.D. Regioregular, Head-to-Tail Coupled Poly (3-alkylthiophenes) Made Easy by the GRIM Method: Investigation of the Reaction and the Origin of Regioselectivity. *Macromolecules*. **2001**. *34*, 4324–4333.
- [52] Yokoyama, A.; Miyakoshi, R.; Yokozawa, T. Chain-Growth Polymerization for Poly (3-hexylthiophene) with a Defined Molecular Weight and a Low Polydispersity. *Macromolecules*. **2004**. *37*, 1169–1171.
- [53] Lohwasser, R.H.; Thelakkat, M. Toward Perfect Control of End Groups and Polydispersity in Poly (3-hexylthiophene) via Catalyst Transfer Polymerization. *Macromolecules*. **2011**. *44*, 3388–3397.
- [54] Jeffries-EL, M.; Sauvé, G.; McCullough, R.D. In-Situ End-Group Functionalization of Regioregular Poly (3-alkylthiophene) Using the Grignard Metathesis Polymerization Method. *Advanced materials*. **2004**. *16*, 1017–1019.

- [55] Kochemba, W.M.; Kilbey, S.M.; Pickel, D.L. End-Group Composition of Poly(3-hexylthiophene)s Prepared by in Situ Quenching of the Grignard Metathesis Polymerization: Influence of Additives and Reaction Conditions. *Journal of Polymer Science Part A: Polymer Chemistry*. **2012**. *50*, 2762–2769.
- [56] Chen, H.P.; Chen, J.H.; Yin, W.; Yu, X.; Shao, M.; Xiao, K.; Hong, K.L.; Pickel, D.L.; Kochemba, W.M.; Kilbey, S.M.; Dadmun, M. Correlation of Polymeric Compatibilizer Structure to its Impact on the Morphology and Function of P3HT:PCBM Bulk Heterojunctions. *Journal of Materials Chemistry A*. **2013**. *1*, 5309–5319. *J Mater Chem A*.
- [57] Alonzo, J.; Kochemba, W.M.; Pickel, D.L.; Ramanathan, M.; Sun, Z.; Li, D.; Chen, J.; Sumpter, B.G.; Heller, W.T.; Kilbey, S.M. Assembly and Organization of Poly(3-hexylthiophene) Brushes and Their Potential Use as Novel Anode Buffer Layers for Organic Photovoltaics. *Nanoscale*. **2013**. *5*, 9357–64.
- [58] Liu, J.; Loewe, R.S.; McCullough, R.D. Employing MALDI-MS on Poly(alkylthiophenes): Analysis of Molecular Weights, Molecular Weight Distributions, End-Group Structures, and End-Group Modifications. *Macromolecules*. **1999**. *32*, 5777–5785.
- [59] Liu, J.S.; McCullough, R.D. End Group Modification of Regioregular Polythiophene Through Postpolymerization Functionalization. *Macromolecules*. **2002**. *35*, 9882–9889.
- [60] Holdcroft, S. Determination of Molecular Weights and Mark–Houwink Constants for Soluble Electronically Conducting Polymers. *Journal of Polymer Science Part B: Polymer Physics*. **1991**. *29*, 1585–1588.
- [61] Montaudo, G.; Montaudo, M.S.; Puglisi, C.; Samperi, F. Characterization of Polymers by Matrix-Assisted Laser Desorption/Ionization Time-of-Flight

- Mass Spectrometry: Molecular Weight Estimates in Samples of Varying Polydispersity. *Rapid Communications in Mass Spectrometry*. **1995**. *9*, 453–460.
- [62] Montaudo, G.; Garozzo, D.; Montaudo, M.S.; Puglisi, C.; Samperi, F. Molecular and Structural Characterization of Polydisperse Polymers and Copolymers by Combining MALDI-TOF Mass Spectrometry with GPC Fractionation. *Macromolecules*. **1995**. *28*, 7983–7989.
- [63] Servaites, J.D.; Ratner, M.A.; Marks, T.J. Organic Solar Cells: A New Look at Traditional Models. *Energy & Environmental Science*. **2011**. *4*, 4410–4422.
- [64] Huang, Y.; Kramer, E.J.; Heeger, A.J.; Bazan, G.C. Bulk Heterojunction Solar Cells: Morphology and Performance Relationships. *Chemical Reviews*. **2014**. *114*, 7006–7043.
- [65] Ma, W.; Yang, C.; Gong, X.; Lee, K.; Heeger, A.J. Thermally Stable, Efficient Polymer Solar Cells with Nanoscale Control of the Interpenetrating Network Morphology. *Advanced Functional Materials*. **2005**. *15*, 1617–1622.
- [66] Chen, J.; Yu, X.; Hong, K.; Messman, J.M.; Pickel, D.L.; Xiao, K.; Dadmun, M.D.; Mays, J.W.; Rondinone, A.J.; Sumpter, B.G.; et al. Ternary Behavior and Systematic Nanoscale Manipulation of Domain Structures in P3HT/PCBM/P3HT-b-PEO Films. *Journal of Materials Chemistry*. **2012**. *22*, 13013–13022.
- [67] Herzing, A.A.; Ro, H.W.; Soles, C.L.; DeLongchamp, D.M. Visualization of Phase Evolution in Model Organic Photovoltaic Structures via Energy-Filtered Transmission Electron Microscopy. *Acs Nano*. **2013**. *7*, 7937–7944.
- [68] Schindler, W.; Wollgarten, M.; Fostiropoulos, K. Revealing Nanoscale Phase Separation in Small-Molecule Photovoltaic Blends by Plasmonic Contrast in the TEM. *Organic Electronics*. **2012**. *13*, 1100–1104.

- [69] Hu, S.; Dyck, O.; Chen, H.; Hsiao, Y.c.; Hu, B.; Duscher, G.; Dadmun, M.; Khomami, B. The Impact of Selective Solvents on the Evolution of Structure and Function in Solvent Annealed Organic Photovoltaics. *RSC Advances*. **2014**. *4*, 27931–27931.
- [70] Herzing, A.a.; Richter, L.J.; Anderson, I.M. 3D Nanoscale Characterization of Thin-Film Organic Photovoltaic Device Structures via Spectroscopic Contrast in the TEM. *Journal of Physical Chemistry C*. **2010**. *114*, 17501–17508.
- [71] Drummy, L.F.; Davis, R.J.; Moore, D.L.; Durstock, M.; Vaia, R.A.; Hsu, J.W.P. Molecular-Scale and Nanoscale Morphology of P3HT:PCBM Bulk Heterojunctions: Energy-Filtered TEM and Low-Dose HREM. *Chemistry of Materials*. **2011**. *23*, 907–912.
- [72] Loos, J.; van Duren, J.K.J.; Morrissey, F.; Janssen, R.A.J. The Use of the Focused Ion Beam Technique to Prepare Cross-Sectional Transmission Electron Microscopy Specimen of Polymer Solar Cells Deposited on GlassI. *Polymer*. **2002**. *43*, 7493–7496.
- [73] Mayer. TEM Sample Preparation and FIB Induced Damage. *Materials Research Society Bulletin*. **2007**. *32*, 400–407.
- [74] Wang, T.; Dunbar, A.D.F.; Staniec, P.a.; Pearson, A.J.; Hopkinson, P.E.; MacDonald, J.E.; Lilliu, S.; Pizzey, C.; Terrill, N.J.; Donald, A.M.; Ryan, A.J.; Jones, R.a.L.; Lidzey, D.G. The Development of Nanoscale Morphology in Polymer: Fullerene Photovoltaic Blends During Solvent Casting. *Soft Matter*. **2010**. *6*, 4128–4134.
- [75] Liu, F.; Chen, D.; Wang, C.; Luo, K.; Gu, W.; Briseno, A.L.; Hsu, J.W.P.; Russell, T.P. Molecular Weight Dependence of the Morphology in P3HT:PCBM Solar Cells. *ACS Applied Materials & Interfaces*. **2014**. *6*, 19876–19887.

- [76] Kim, J.Y.; Frisbie, C.D. Correlation of Phase Behavior and Charge Transport in Conjugated Polymer/Fullerene Blends. *The Journal of Physical Chemistry C*. **2008**. *112*, 17726–17736.
- [77] Zhao, J.; Swinnen, A.; Van Assche, G.; Manca, J.; Vanderzande, D.; Mele, B.V. Phase Diagram of P3HT/PCBM Blends and its Implication for the Stability of Morphology. *The Journal of Physical Chemistry B*. **2009**. *113*, 1587–1591.
- [78] Snyder, C.R.; Henry, J.S.; DeLongchamp, D.M. Effect of Regioregularity on the Semicrystalline Structure of Poly (3-hexylthiophene). *Macromolecules*. **2011**. *44*, 7088–7091.
- [79] Lai, Y.C.; Higashihara, T.; Hsu, J.C.; Ueda, M.; Chen, W.C. Enhancement of Power Conversion Efficiency and Long-Term Stability of P3HT/PCBM Solar Cells Using C 60 Derivatives with Thiophene Units as Surfactants. *Solar Energy Materials and Solar Cells*. **2012**. *97*, 164–170.
- [80] Wang, S.; Qu, Y.; Li, S.; Ye, F.; Chen, Z.; Yang, X. Improved Thermal Stability of Polymer Solar Cells by Incorporating Porphyrins. *Advanced Functional Materials*. **2015**. *25*, 748–757.
- [81] Snyder, C.R.; Kline, R.J.; DeLongchamp, D.M.; Nieuwendaal, R.C.; Richter, L.J.; Heeney, M.; McCulloch, I. Classification of Semiconducting Polymeric Mesophases to Optimize Device Postprocessing. *Journal of Polymer Science Part B: Polymer Physics*. **2015**. *53*, 1641–1653.
- [82] Pascui, O.F.; Lohwasser, R.; Sommer, M.; Thelakkat, M.; Thurn-Albrecht, T.; Saalwachter, K. High Crystallinity and Nature of Crystal- Crystal Phase Transformations in Regioregular Poly (3-hexylthiophene). *Macromolecules*. **2010**. *43*, 9401–9410.
- [83] Remy, R.; Weiss, E.D.; Nguyen, N.A.; Wei, S.; Campos, L.M.; Kowalewski, T.; Mackay, M.E. Enthalpy of Fusion of Poly (3-hexylthiophene) by Differential

- Scanning Calorimetry. *Journal of Polymer Science Part B: Polymer Physics*. **2014**. *52*, 1469–1475.
- [84] Malik, S.; Nandi, A.K. Crystallization Mechanism of Regioregular Poly (3-alkyl thiophene) s. *Journal of Polymer Science Part B: Polymer Physics*. **2002**. *40*, 2073–2085.
- [85] Lee, C.S.; Dadmun, M.D. Important Thermodynamic Characteristics of Poly (3-hexyl thiophene). *Polymer*. **2014**. *55*, 4–7.
- [86] Koch, F.P.V.; Heeney, M.; Smith, P. Thermal and Structural Characteristics of Oligo (3-hexylthiophene) s (3HT) n, n= 4–36. *Journal of the American Chemical Society*. **2013**. *135*, 13699–13709.
- [87] Koch, F.P.; Smith, P.; Heeney, M. Fibonacci Route to Regioregular Oligo (3-hexylthiophene) s. *Journal of the American Chemical Society*. **2013**. *135*, 13695–13698.
- [88] Bulle-Lieuwma, C.; Van Gennip, W.; Van Duren, J.; Jonkheijm, P.; Janssen, R.; Niemantsverdriet, J. Characterization of Polymer Solar Cells by TOF-SIMS Depth Profiling. *Applied surface science*. **2003**. *203*, 547–550.
- [89] Prosa, T.; Winokur, M.; Moulton, J.; Smith, P.; Heeger, A. X-ray Structural Studies of Poly (3-alkylthiophenes): An Example of An Inverse Comb. *Macromolecules*. **1992**. *25*, 4364–4372.
- [90] Kozub, D.R.; Vakhshouri, K.; Orme, L.M.; Wang, C.; Hexemer, A.; Gomez, E.D. Polymer Crystallization of Partially Miscible Polythiophene/Fullerene Mixtures Controls Morphology. *Macromolecules*. **2011**. *44*, 5722–5726.
- [91] Tao, C.; Ruan, S.; Zhang, X.; Xie, G.; Shen, L.; Kong, X.; Dong, W.; Liu, C.; Chen, W. Performance Improvement of Inverted Polymer Solar Cells with Different Top Electrodes by Introducing a MoO<sub>3</sub> Buffer Layer. *Applied Physics Letters*. **2008**. *93*, 193307–1.

- [92] Mihailetschi, V.; Blom, P.; Hummelen, J.; Rispen, M. Cathode Dependence of the Open-Circuit Voltage of Polymer: Fullerene Bulk Heterojunction Solar Cells. *Journal of Applied Physics*. **2003**. *94*, 6849–6854.
- [93] Scott, J.; Malliaras, G.; Chen, W.; Breach, J.C.; Salem, J.; Brock, P.; Sachs, S.; Chidsey, C. Hole Limited Recombination in Polymer Light-Emitting Diodes. *Applied Physics Letters*. **1999**. *74*, 1510–1512.
- [94] Guo, X.G.; Marks, T.J. Plastic Solar Cells with Engineered Interfaces. *Organic Photonic Materials and Devices Xv*. **2013**. *8622*, 86220K–86220K–10.
- [95] Hains, A.W.; Liu, J.; Martinson, A.B.; Irwin, M.D.; Marks, T.J. Anode Interfacial Tuning via Electron-Blocking/Hole-Transport Layers and Indium Tin Oxide Surface Treatment in Bulk-Heterojunction Organic Photovoltaic Cells. *Advanced Functional Materials*. **2010**. *20*, 595–606.
- [96] Gregg, B.A. Excitonic Solar Cells. *The Journal of Physical Chemistry B*. **2003**. *107*, 4688–4698.
- [97] Brown, T.; Kim, J.; Friend, R.; Cacialli, F.; Daik, R.; Feast, W. Built-in Field Electroabsorption Spectroscopy of Polymer Light-Emitting Diodes Incorporating a Doped Poly (3, 4-ethylene dioxythiophene) Hole Injection Layer. *Applied Physics Letters*. **1999**. *75*, 1679–1681.
- [98] Kemerink, M.; Timpanaro, S.; De Kok, M.; Meulenkaamp, E.; Touwslager, F. Three-Dimensional Inhomogeneities in PEDOT: PSS Films. *The Journal of Physical Chemistry B*. **2004**. *108*, 18820–18825.
- [99] Ionescu-Zanetti, C.; Mechler, A.; Carter, S.A.; Lal, R. Semiconductive Polymer Blends: Correlating Structure with Transport Properties at the Nanoscale. *Advanced Materials*. **2004**. *16*, 385–389.



- [100] Li, G.; Shrotriya, V.; Huang, J.; Yao, Y.; Moriarty, T.; Emery, K.; Yang, Y. High-Efficiency Solution Processable Polymer Photovoltaic Cells by Self-Organization of Polymer Blends. *Nature Materials*. **2005**. *4*, 864–868.
- [101] Peumans, P.; Forrest, S. Very-High-Efficiency Double-Heterostructure Copper Phthalocyanine/C60 Photovoltaic Cells. *Applied Physics Letters*. **2001**. *79*, 126–128.
- [102] Lee, T.W.; Chung, Y. Control of the Surface Composition of a Conducting-Polymer Complex Film to Tune the Work Function. *Advanced Functional Materials*. **2008**. *18*, 2246–2252.
- [103] De Kok, M.; Buechel, M.; Vulto, S.; Van de Weijer, P.; Meulenkamp, E.; De Winter, S.; Mank, A.; Vorstenbosch, H.; Weijtens, C.; Van Elsbergen, V. Modification of PEDOT: PSS as Hole Injection Layer in Polymer LEDs. *Physica Status Solidi (a)*. **2004**. *201*, 1342–1359.
- [104] Yan, H.; Lee, P.; Armstrong, N.R.; Graham, A.; Evmenenko, G.A.; Dutta, P.; Marks, T.J. High-Performance Hole-Transport Layers for Polymer Light-Emitting Diodes. Implementation of Organosiloxane Cross-Linking Chemistry in Polymeric Electroluminescent Devices. *Journal of the American Chemical Society*. **2005**. *127*, 3172–3183.
- [105] Kim, Y.H.; Lee, S.H.; Noh, J.; Han, S.H. Performance and Stability of Electroluminescent Device with Self-Assembled Layers of Poly (3, 4-ethylenedioxythiophene)–Poly (styrenesulfonate) and Polyelectrolytes. *Thin Solid Films*. **2006**. *510*, 305–310.
- [106] Huang, Q.; Evmenenko, G.; Dutta, P.; Marks, T.J. Molecularly Engineered Anode Adsorbates for Probing OLED Interfacial Structure-charge Injection/Luminance Relationships: Large, Structure-Dependent Effects. *Journal of the American Chemical Society*. **2003**. *125*, 14704–14705.

- [107] Huang, Q.; Evmenenko, G.A.; Dutta, P.; Lee, P.; Armstrong, N.R.; Marks, T.J. Covalently Bound Hole-Injecting Nanostructures. Systematics of Molecular Architecture, Thickness, Saturation, and Electron-Blocking Characteristics on Organic Light-Emitting Diode Luminance, Turn-on Voltage, and Quantum Efficiency. *Journal of the American Chemical Society*. **2005**. *127*, 10227–10242.
- [108] Nguyen, T.; De Vos, S. An Investigation into the Effect of Chemical and Thermal Treatments on the Structural Changes of Poly (3, 4-ethylenedioxythiophene)/Polystyrenesulfonate and Consequences on its Use on Indium Tin Oxide Substrates. *Applied Surface Science*. **2004**. *221*, 330–339.
- [109] Ni, J.; Yan, H.; Wang, A.; Yang, Y.; Stern, C.L.; Metz, A.W.; Jin, S.; Wang, L.; Marks, T.J.; Ireland, J.R.; et al. MOCVD-Derived Highly Transparent, Conductive Zinc-and Tin-Doped Indium Oxide Thin Films: Precursor Synthesis, Metastable Phase Film Growth and Characterization, and Application as Anodes in Polymer Light-Emitting Diodes. *Journal of the American Chemical Society*. **2005**. *127*, 5613–5624.
- [110] Jørgensen, M.; Norrman, K.; Krebs, F.C. Stability/Degradation of Polymer Solar Cells. *Solar Energy Materials and Solar Cells*. **2008**. *92*, 686–714.
- [111] Rider, D.A.; Harris, K.D.; Wang, D.; Bruce, J.; Fleischauer, M.D.; Tucker, R.T.; Brett, M.J.; Buriak, J.M. Thienylsilane-Modified Indium Tin Oxide as an Anodic Interface in Polymer/Fullerene Solar Cells. *ACS Applied Materials & Interfaces*. **2008**. *1*, 279–288.
- [112] Wong, K.W.; Yip, H.; Luo, Y.; Wong, K.; Lau, W.; Low, K.; Chow, H.; Gao, Z.; Yeung, W.; Chang, C. Blocking Reactions Between Indium-Tin Oxide and Poly (3, 4-ethylene dioxothiophene): Poly (styrene sulphonate) with a Self-Assembly Monolayer. *Applied physics letters*. **2002**. *80*, 2788–2790.

- [113] De Jong, M.; Van Ijzendoorn, L.; De Voigt, M. Stability of the Interface Between Indium-tin-oxide and Poly (3, 4-ethylenedioxythiophene)/poly (styrenesulfonate) in Polymer Light-Emitting Diodes. *Applied Physics Letters*. **2000**. *77*, 2255–2257.
- [114] Norrman, K.; Krebs, F.C. Lifetimes of Organic Photovoltaics: Using TOF-SIMS and <sup>18</sup>O Isotopic Labelling to Characterise Chemical Degradation Mechanisms. *Solar Energy Materials & Solar Cells*. **2006**. *90*, 213–227.
- [115] Hermenau, M.; Riede, M.; Leo, K.; Gevorgyan, S.A.; Krebs, F.C.; Norrman, K. Water and Oxygen Induced Degradation of Small Molecule Organic Solar Cells. *Solar Energy Materials & Solar Cells*. **2011**. *95*, 1268–1277.
- [116] Norrman, K.; Madsen, M.V.; Gevorgyan, S.a.; Krebs, F.C. Degradation Patterns in Water and Oxygen of an Inverted Polymer Solar Cell. *Journal of the American Chemical Society*. **2010**. *132*, 16883–16892.
- [117] Girtan, M.; Rusu, M. Role of ITO and PEDOT: PSS in Stability/Degradation of Polymer:Fullerene Bulk Heterojunctions Solar Cells. *Solar Energy Materials and Solar Cells*. **2010**. *94*, 446–450.
- [118] Kawano, K.; Pacios, R.; Poplavskyy, D.; Nelson, J.; Bradley, D.D.; Durrant, J.R. Degradation of Organic Solar Cells Due to Air Exposure. *Solar Energy Materials and Solar Cells*. **2006**. *90*, 3520–3530.
- [119] Winter, I.; Reese, C.; Hormes, J.; Heywang, G.; Jonas, F. The Thermal Ageing of Poly (3, 4-ethylenedioxythiophene). An investigation by X-ray Absorption and X-ray Photoelectron Spectroscopy. *Chemical Physics*. **1995**. *194*, 207–213.
- [120] Marciniak, S.; Crispin, X.; Uvdal, K.; Trzcinski, M.; Birgerson, J.; Groenendaal, L.; Louwet, F.; Salaneck, W.R. Light Induced Damage in Poly (3, 4-ethylenedioxythiophene) and its Derivatives Studied by Photoelectron Spectroscopy. *Synthetic Metals*. **2004**. *141*, 67–73.

- [121] Wu, J.L.; Chen, F.C.; Hsiao, Y.S.; Chien, F.C.; Chen, P.; Kuo, C.H.; Huang, M.H.; Hsu, C.S. Surface Plasmonic Effects of Metallic Nanoparticles on the Performance of Polymer Bulk Heterojunction Solar Cells. *ACS Nano*. **2011**. *5*, 959–67.
- [122] Chen, F.C.; Wu, J.L.; Lee, C.L.; Hong, Y.; Kuo, C.H.; Huang, M.H. Plasmonic-Enhanced Polymer Photovoltaic Devices Incorporating Solution-Processable Metal Nanoparticles. *Applied Physics Letters*. **2009**. *95*, 013305.
- [123] Lobez, J.M.; Andrew, T.L.; Bulovi, V.; Swager, T.M.; Bulovi, V. Improving the Performance of P3HT Fullerene Solar Cells with Side-Chain- Functionalized Poly ( thiophene ) Additives : A New Paradigm for Polymer Design. *ACS Nano*. **2012**.
- [124] Liu, F.; Page, Z.A.; Duzhko, V.V.; Russell, T.P.; Emrick, T. Conjugated Polymeric Zwitterions as Efficient Interlayers in Organic Solar Cells. *Advanced Materials*. **2013**. *25*, 6868–73.
- [125] Ma, H.; Yip, H.L.; Huang, F.; Jen, A.K.Y. Interface Engineering for Organic Electronics. *Advanced Functional Materials*. **2010**. *20*, 1371–1388.
- [126] Khodabakhsh, S.; Sanderson, B.M.; Nelson, J.; Jones, T.S. Using Self-Assembling Dipole Molecules to Improve Charge Collection in Molecular Solar Cells. *Advanced Functional Materials*. **2006**. *16*, 95–100.
- [127] Kim, J.S.; Park, J.H.; Lee, J.H.; Jo, J.; Kim, D.Y.; Cho, K. Control of the Electrode Work Function and Active Layer Morphology via Surface Modification of Indium Tin Oxide for High Efficiency Organic Photovoltaics. *Applied Physics Letters*. **2007**. *91*, 112111.
- [128] Whiting, G.L.; Snaith, H.J.; Khodabakhsh, S.; Andreasen, J.W.; Breiby, D.W.; Nielsen, M.M.; Greenham, N.C.; Friend, R.H.; Huck, W.T. Enhancement of

Charge-Transport Characteristics in Polymeric Films Using Polymer Brushes. *Nano Letters*. **2006**. *6*, 573–578.

- [129] Soto-Cantu, E.; Lokitz, B.S.; Hinestrosa, J.P.; Deodhar, C.; Messman, J.M.; Ankner, J.F.; Kilbey II, S.M. Versatility of Alkyne-Modified Poly (Glycidyl Methacrylate) Layers for Click Reactions. *Langmuir*. **2011**. *27*, 5986–5996.
- [130] Alonzo, J.; Mays, J.W.; Kilbey II, S.M. Forces of Interaction Between Surfaces Bearing Looped Polymer Brushes in Good Solvent. *Soft Matter*. **2009**. *5*, 1897–1904.
- [131] Kilbey, S.M.; Watanabe, H.; Tirrell, M. Structure and Scaling of Polymer Brushes near the  $\vartheta$  Condition. *Macromolecules*. **2001**. *34*, 5249–5259.
- [132] Heffner, G.W.; Pearson, D.S. Molecular Characterization of Poly (3-hexylthiophene). *Macromolecules*. **1991**. *24*, 6295–6299.
- [133] Iyer, K.S.; Luzinov, I. Effect of Macromolecular Anchoring Layer Thickness and Molecular Weight on Polymer Grafting. *Macromolecules*. **2004**. *37*, 9538–9545.
- [134] Pfannmüller, M.; Flgge, H.; Benner, G.; Wacker, I.; Sommer, C.; Hanselmann, M.; Schmale, S.; Schmidt, H.; Hamprecht, F.A.; Rabe, T.; Kowalsky, W.; Schröder, R.R. Visualizing a Homogeneous Blend in Bulk Heterojunction Polymer Solar Cells by Analytical Electron Microscopy. *Nano Letters*. **2011**. *11*, 3099–107.
- [135] Kohno, H.; Takeda, S.; Tanaka, K. Plasmon Loss Imaging of Chains of Crystalline Silicon Nanospheres and Silicon Nanowires. *Journal of Electron Microscopy*. **2000**. *49*, 275–280.
- [136] Kiel, J.W.; Mackay, M.E.; Kirby, B.J.; Maranville, B.B.; Majkrzak, C.F. Phase-Sensitive Neutron Reflectometry Measurements Applied in the Study of Photovoltaic Films. *Journal of Chemical Physics*. **2010**. *133*, 074902. The Journal of chemical physics.

- [137] Clarke, C.J.; Jones, R.A.L.; Edwards, J.L.; Shull, K.R.; Penfold, J. The Structure of Grafted Polystyrene Layers in a Range of Matrix Polymers. *Macromolecules*. **1995**. *28*, 2042–2049.
- [138] Motaung, D.E.; Malgas, G.F.; Arendse, C.J.; Mavundla, S.E. Determination of the Structure, Morphology and Complex Refractive Index in ZnO-Nanopencils/P3HT Hybrid Structures. *Materials Chemistry and Physics*. **2012**. *135*, 401–410.
- [139] Bassim, N.D.; De Gregorio, B.T.; Kilcoyne, A.L.D.; Scott, K.; Chou, T.; Wirick, S.; Cody, G.; Stroud, R.M. Minimizing Damage During FIB Sample Preparation of Soft Materials. *Journal of Microscopy*. **2012**. *245*, 288–301.
- [140] Chun, S.B.; Han, C.D. Morphology of Model A/B(C-block-D) Ternary Blends and Compatibilization of Two Immiscible Homopolymers A and B with a C-block-D Copolymer. *Macromolecules*. **2000**. *33*, 3409–3424. *Macromolecules*.
- [141] Jackson, C.L.; Sung, L.; Han, C.C. Evolution of Phase Morphology in Compatibilized Polymer Blends at Constant Quench Depths: Complementary Studies by Light Scattering and Transmission Electron Microscopy. *Polymer Engineering and Science*. **1997**. *37*, 1449–1458. *Polym Eng Sci*.
- [142] Thomas, S.; Prudhomme, R.E. Compatibilizing Effect of Block Copolymers in Heterogeneous Polystyrene Poly(Methyl Methacrylate) Blends. *Polymer*. **1992**. *33*, 4260–4268. *Polymer*.
- [143] Galloway, J.A.; Jeon, H.K.; Bell, J.R.; Macosko, C.W. Block Copolymer Compatibilization of Cocontinuous Polymer Blends. *Polymer*. **2005**. *46*, 183–191.

- [144] Bechara, R.; Leclerc, N.; Leveque, P.; Richard, F.; Heiser, T.; Hadziioannou, G. Efficiency Enhancement of Polymer Photovoltaic Devices Using Thieno-Thiophene Based Copolymers as Nucleating Agents for Polythiophene Crystallization. *Applied Physics Letters*. **2008**. *93*.
- [145] Graham, K.R.; Cabanetos, C.; Jahnke, J.P.; Idso, M.N.; El Labban, A.; Ngongang Ndjawa, G.O.; Heumueller, T.; Vandewal, K.; Salleo, A.; Chmelka, B.F.; Amassian, A.; Beaujuge, P.M.; McGehee, M.D. Importance of the donor:fullerene intermolecular arrangement for high-efficiency organic photovoltaics. *Journal of American Chemical Society*. **2014**. *136*, 9608–18.
- [146] Kim, J.B.; Allen, K.; Oh, S.J.; Lee, S.; Toney, M.F.; Kim, Y.S.; Kagan, C.R.; Nuckolls, C.; Loo, Y.L. Small-Molecule Thiophene-C-60 Dyads As Compatibilizers in Inverted Polymer Solar Cells. *Chemistry of Materials*. **2010**. *22*, 5762–5773. Chem Mater.
- [147] Lee, J.U.; Jung, J.W.; Emrick, T.; Russell, T.P.; Jo, W.H. Synthesis of C60-end Capped P3HT and its Application for High Performance of P3HT/PCBM Bulk Heterojunction Solar Cells. *Journal of Materials Chemistry*. **2010**. *20*, 3287.
- [148] Lin, Y.; Lim, J.A.; Wei, Q.S.; Mannsfeld, S.C.B.; Brisenno, A.L.; Watkins, J.J. Cooperative Assembly of Hydrogen-Bonded Diblock Copolythiophene/Fullerene Blends for Photovoltaic Devices with Well-Defined Morphologies and Enhanced Stability. *Chemistry of Materials*. **2012**. *24*, 622–632. Chem Mater.
- [149] Sun, Z.; Xiao, K.; Keum, J.K.; Yu, X.; Hong, K.; Browning, J.; Ivanov, I.N.; Chen, J.; Alonzo, J.; Li, D.; Sumpter, B.G.; Payzant, E.A.; Rouleau, C.M.; Geoghegan, D.B. PS-b-P3HT Copolymers as P3HT/PCBM Interfacial Compatibilizers for High Efficiency Photovoltaics. *Advanced Materials*. **2011**. *23*, 5529–35.

- [150] Lim, D.C.; Kim, K.D.; Park, S.Y.; Hong, E.M.; Seo, H.O.; Lim, J.H.; Lee, K.H.; Jeong, Y.; Song, C.; Lee, E.; Kim, Y.D.; Cho, S. Towards Fabrication of High-Performing Organic Photovoltaics: New Donor-Polymer, Atomic Layer Deposited Thin Buffer Layer and Plasmonic Effects. *Energy & Environmental Science*. **2012**. *5*, 9803–9807. Energ Environ Sci.
- [151] Renaud, C.; Mognier, S.J.; Pavlopoulou, E.; Brochon, C.; Fleury, G.; Deribew, D.; Portale, G.; Cloutet, E.; Chambon, S.; Vignau, L.; Hadziioannou, G. Block Copolymer as a Nanostructuring Agent for High-Efficiency and Annealing-Free Bulk Heterojunction Organic Solar Cells. *Advanced Materials*. **2012**. *24*, 2196–201.
- [152] Sary, N.; Richard, F.; Brochon, C.; Leclerc, N.; Leveque, P.; Audinot, J.N.; Berson, S.; Heiser, T.; Hadziioannou, G.; Mezzenga, R. A New Supramolecular Route for Using Rod-Coil Block Copolymers in Photovoltaic Applications. *Advanced Materials*. **2010**. *22*, 763–8.
- [153] Sivula, K.; Ball, Z.T.; Watanabe, N.; Frechet, J.M.J. Amphiphilic Diblock Copolymer Compatibilizers and Their Effect on the Morphology and Performance of Polythiophene: Fullerene Solar Cells. *Advanced Materials*. **2006**. *18*, 206–+. Adv Mater.
- [154] Tsai, J.H.; Lai, Y.C.; Higashihara, T.; Lin, C.J.; Ueda, M.; Chen, W.C. Enhancement of P3HT/PCBM Photovoltaic Efficiency Using the Surfactant of Triblock Copolymer Containing Poly(3-hexylthiophene) and Poly(4-vinyltriphenylamine) Segments. *Macromolecules*. **2010**. *43*, 6085–6091. Macromolecules.
- [155] Yuan, K.; Li, F.; Chen, L.; Wang, H.M.; Chen, Y.W. Understanding the Mechanism of Poly(3-hexylthiophene)-b-poly(4-vinylpyridine) as a Nanostructuring



- Compatibilizer for Improving the Performance of Poly(3-hexylthiophene)/ZnO-Based Hybrid Solar Cells. *Journal of Materials Chemistry A*. **2013**. *1*, 10881–10888. *J Mater Chem A*.
- [156] Brinkmann, M.; Rannou, P. Molecular Weight Dependence of Chain Packing and Semicrystalline Structure in Oriented Films of Regioregular Poly (3-hexylthiophene) Revealed by High-Resolution Transmission Electron Microscopy. *Macromolecules*. **2009**. *42*, 1125–1130.
- [157] Zen, A.; Pflaum, J.; Hirschmann, S.; Zhuang, W.; Jaiser, F.; Asawapirom, U.; Rabe, J.P.; Scherf, U.; Neher, D. Effect of Molecular Weight and Annealing of Poly(3-hexylthiophene)s on the Performance of Organic Field-Effect Transistors. *Advanced Functional Materials*. **2004**. *14*, 757–764.
- [158] Kline, R.J.; McGehee, M.D.; Kadnikova, E.N.; Liu, J.; Fréchet, J.M.J. Controlling the Field-Effect Mobility of Regioregular Polythiophene by Changing the Molecular Weight. *Advanced Materials*. **2003**. *15*, 1519–1522.
- [159] Brinkmann, M.; Rannou, P. Effect of Molecular Weight on the Structure and Morphology of Oriented Thin Films of Regioregular Poly(3-hexylthiophene) Grown by Directional Epitaxial Solidification. *Advanced Functional Materials*. **2007**. *17*, 101–108.
- [160] Carrillo, J.M.Y.; Seibers, Z.; Kumar, R.; Matheson, M.A.; Ankner, J.F.; Goswami, M.; Bhaskaran-Nair, K.; Shelton, W.A.; Sumpter, B.G.; Kilbey, S.M. Petascale Simulations of the Morphology and the Molecular Interface of Bulk Heterojunctions. *ACS Nano*. **2016**. *10*, 7008–7022.
- [161] Carrillo, J.M.; Kumar, R.; Goswami, M.; Sumpter, B.G.; Brown, W.M. New Insights Into the Dynamics and Morphology of P3HT:PCBM Active Layers in Bulk Heterojunctions. *Phys Chem Chem Phys*. **2013**. *15*, 17873–82.

- [162] Miyakoshi, R.; Yokoyama, A.; Yokozawa, T. Catalyst-Transfer Polycondensation. Mechanism of Ni-catalyzed Chain-Growth Polymerization Leading to Well-Defined Poly(3-hexylthiophene). *Journal of the American Chemical Society*. **2005**. *127*, 17542–7.
- [163] Vajjala Kesava, S.; Dhanker, R.; Kozub, D.R.; Vakhshouri, K.; Choi, U.H.; Colby, R.H.; Wang, C.; Hexemer, A.; Giebink, N.C.; Gomez, E.D. Mesoscopic Structural Length Scales in P3HT/PCBM Mixtures Remain Invariant for Various Processing Conditions. *Chemistry of Materials*. **2013**. *25*, 2812–2818.
- [164] Le, T.P.; Shang, Z.; Wang, L.; Li, N.; Vajjala Kesava, S.; OConnor, J.W.; Chang, Y.; Bae, C.; Zhu, C.; Hexemer, A.; et al. Miscibility and Acid Strength Govern Contact Doping of Organic Photovoltaics with Strong Polyelectrolytes. *Macromolecules*. **2015**. *48*, 5162–5171.
- [165] Liao, H.C.; Tsao, C.S.; Lin, T.H.; Chuang, C.M.; Chen, C.Y.; Jeng, U.S.; Su, C.H.; Chen, Y.F.; Su, W.F. Quantitative Nanoorganized Structural Evolution for a High Efficiency Bulk Heterojunction Polymer Solar Cell. *Journal of the American Chemical Society*. **2011**. *133*, 13064–13073.
- [166] Ophir, Z.; Wilkes, G.L. Saxs Analysis of a Linear Polyester and a Linear Polyether Urethane - Interfacial Thickness Determination. *Journal of Polymer Science Part B-Polymer Physics*. **1980**. *18*, 1469–1480. *J Polym Sci Pol Phys*.
- [167] Vakhshouri, K.; Kesava, S.V.; Kozub, D.R.; Gomez, E.D. Characterization of the Mesoscopic Structure in the Photoactive Layer of Organic Solar Cells: A Focused Review. *Materials Letters*. **2013**. *90*, 97–102.
- [168] Guo, C.; Kozub, D.R.; Vajjala Kesava, S.; Wang, C.; Hexemer, A.; Gomez, E.D. Signatures of Multiphase Formation in the Active Layer of Organic Solar Cells from Resonant Soft X-Ray Scattering. *ACS Macro Letters*. **2013**. *2*, 185–189.

- [169] Kesava, S.V.; Fei, Z.; Rimshaw, A.D.; Wang, C.; Hexemer, A.; Asbury, J.B.; Heeney, M.; Gomez, E.D. Domain Compositions and Fullerene Aggregation Govern Charge Photogeneration in Polymer/Fullerene Solar Cells. *Advanced Energy Materials*. **2014**. *4*.
- [170] Chen, D.; Nakahara, A.; Wei, D.; Nordlund, D.; Russell, T.P. P3HT/PCBM Bulk Heterojunction Organic Photovoltaics: Correlating Efficiency and Morphology. *Nano Letters*. **2011**. *11*, 561–567.
- [171] Chirvase, D.; Parisi, J.; Hummelen, J.C.; Dyakonov, V. Influence of Nanomorphology on the Photovoltaic Action of Polymer-Fullerene Composites. *Nanotechnology*. **2004**. *15*, 1317–1323. *Nanotechnology*.
- [172] Verploegen, E.; Mondal, R.; Bettinger, C.J.; Sok, S.; Toney, M.F.; Bao, Z.A. Effects of Thermal Annealing Upon the Morphology of Polymer-Fullerene Blends. *Advanced Functional Materials*. **2010**. *20*, 3519–3529. *Adv Funct Mater*.
- [173] Gomez, E.D.; Barteau, K.P.; Wang, H.; Toney, M.F.; Loo, Y.L. Correlating the Scattered Intensities of P3HT and PCBM to the Current Densities of Polymer Solar Cells. *Chemical Communications*. **2011**. *47*, 436–438.
- [174] Honda, S.; Ohkita, H.; Benten, H.; Ito, S. Selective Dye Loading at the Heterojunction in Polymer/Fullerene Solar Cells. *Advanced Energy Materials*. **2011**. *1*, 588–598.
- [175] Khlyabich, P.P.; Rudenko, A.E.; Street, R.A.; Thompson, B.C. Influence of Polymer Compatibility on the Open-Circuit Voltage in Ternary Blend Bulk Heterojunction Solar Cells. *ACS Applied Materials & Interfaces*. **2014**. *6*, 9913–9919.

- [176] Sun, Y.; Chien, S.C.; Yip, H.L.; Chen, K.S.; Zhang, Y.; Davies, J.A.; Chen, F.C.; Lin, B.; Jen, A.K.Y. Improved Thin Film Morphology and Bulk-Heterojunction Solar Cell Performance Through Systematic Tuning of the Surface Energy of Conjugated Polymers. *Journal of Materials Chemistry*. **2012**. *22*, 5587–5595.
- [177] Zhang, W.; Huang, J.K.; Chen, C.H.; Chang, Y.H.; Cheng, Y.J.; Li, L.J. High-Gain Phototransistors Based on a CVD MoS<sub>2</sub> Monolayer. *Advanced Materials*. **2013**. *25*, 3456–3461.
- [178] Bulliard, X.; Ihn, S.G.; Yun, S.; Kim, Y.; Choi, D.; Choi, J.Y.; Kim, M.; Sim, M.; Park, J.H.; Choi, W.; et al. Enhanced Performance in Polymer Solar Cells by Surface Energy Control. *Advanced Functional Materials*. **2010**. *20*, 4381–4387.
- [179] Kipp, D.; Mok, J.; Strzalka, J.; Darling, S.B.; Ganesan, V.; Verduzco, R. Rational Design of Thermally Stable, Bicontinuous Donor/Acceptor Morphologies with Conjugated Block Copolymer Additives. *ACS Macro Letters*. **2015**. *4*, 867–871.
- [180] Kozub, D.R.; Vakhshouri, K.; Kesava, S.V.; Wang, C.; Hexemer, A.; Gomez, E.D. Direct Measurements of Exciton Diffusion Length Limitations on Organic Solar Cell Performance. *Chemical Communications*. **2012**. *48*, 5859–5861.
- [181] Kwok, D.Y.; Neumann, A.W. Contact Angle Measurement and Contact Angle Interpretation. *Advances in Colloid and Interface Science*. **1999**. *81*, 167–249.
- [182] Fowkes, F.M. Attractive Forces at Interfaces. *Industrial & Engineering Chemistry*. **1964**. *56*, 40–52.
- [183] Angellier, H.; Molina-Boisseau, S.; Belgacem, M.N.; Dufresne, A. Surface chemical Modification of Waxy Maize Starch Nanocrystals. *Langmuir*. **2005**. *21*, 2425–2433.

- [184] Żenkiewicz, M. Effects of Electron-beam Irradiation on Wettability and Surface Free Energy of a Polypropylene Film. *International journal of adhesion and adhesives*. **2005**. *25*, 61–66.
- [185] Chibowski, E.; Terpilowski, K. Surface Free Energy of Sulfur Revisited: I. Yellow and Orange Samples Solidified Against Glass Surface. *Journal of Colloid and Interface Science*. **2008**. *319*, 505–513.
- [186] Jańczuk, B.; Białopiotrowicz, T.; Wójcik, W. The Components of Surface Tension of Liquids and Their Usefulness in Determinations of Surface Free Energy of Solids. *Journal of Colloid and Interface Science*. **1989**. *127*, 59–66.
- [187] Boyd, P.D.W.; Reed, C.A. Fullerene - Porphyrin Constructs. *Accounts of Chemical Research*. **2005**. *38*, 235–242.
- [188] Boyd, P.D.; Hodgson, M.C.; Rickard, C.E.; Oliver, A.G.; Chaker, L.; Brothers, P.J.; Bolskar, R.D.; Tham, F.S.; Reed, C.A. Selective Supramolecular Porphyrin/Fullerene Interactions<sup>1</sup>. *Journal of the American Chemical Society*. **1999**. *121*, 10487–10495.
- [189] Splan, K.E.; Hupp, J.T. Permeable Nonaggregating Porphyrin Thin Films that Display Enhanced Photophysical Properties. *Langmuir*. **2004**. *20*, 10560–10566.
- [190] Schenning, a.P.H.J.; Hubert, D.H.W.; Feiters, M.C.; Nolte, R.J.M. Control of Aggregation and Tuning of the Location of Porphyrins in Synthetic Membranes as Mimics for Cytochrome P450. *Langmuir*. **1996**. *12*, 1572–1577.
- [191] Burke, K.B.; Belcher, W.J.; Thomsen, L.; Watts, B.; McNeill, C.R.; Ade, H.; Dastoor, P.C. Role of Solvent Trapping Effects in Determining the Structure and Morphology of Ternary Blend Organic Devices. *Macromolecules*. **2009**. *42*, 3098–3103.

- [192] Balaban, T.S.; Eichhofer, A.; Lehn, J. Self-Assembly by Hydrogen Bonding and  $\pi$ - $\pi$  Interactions in the Crystal of a Porphyrin: Attempts to Mimic Bacteriochlorophyll *c*. *European Journal of Organic Chemistry*. **2000**, 4047–4057.
- [193] Lyons, D.M.; Ono, R.J.; Bielawski, C.W.; Sessler, J.L. Porphyrin–Oligothiophene Conjugates as Additives for P3HT/PCBM Solar Cells. *Journal of Materials*. **2012**. *22*, 18956.
- [194] Li, L.; Hollinger, J.; Guerin, G.; Seferos, D.S. Synthesis and Network-Like Self-Assembly of Porphyrin-Polyselenophene Complexes. *Chemphyschem*. **2012**. *13*, 4110–5.
- [195] Cooling, N.; Burke, K.B.; Zhou, X.; Lind, S.J.; Gordon, K.C.; Jones, T.W.; Dastoor, P.C.; Belcher, W.J. A Study of the Factors Influencing the Performance of Ternary MEH-PPV:Porphyrin:PCBM Heterojunction Devices: A Steric Approach to Controlling Charge Recombination. *Solar Energy Materials & Solar Cells*. **2011**. *95*, 1767–1774.
- [196] Belcher, W.; Wagner, K.; Dastoor, P. The Effect of Porphyrin Inclusion on the Spectral Response of Ternary P3HT:Porphyrin:PCBM Bulk Heterojunction Solar Cells. *Sol. Energy Mater. Sol. Cells*. **2007**. *91*, 447–452.
- [197] Kaushal, M.; Ortiz, A.L.; Kassel, J.A.; Hall, N.; Lee, T.D.; Singh, G.; Walter, M.G. Enhancing Exciton Diffusion in Porphyrin Thin Films Using Peripheral Carboalkoxy Groups to Influence Molecular Assembly. *Journal of Materials Chemistry C*. **2016**.
- [198] Wang, C.L.; Zhang, W.B.; Van Horn, R.M.; Tu, Y.; Gong, X.; Cheng, S.Z.; Sun, Y.; Tong, M.; Seo, J.; Hsu, B.B.; et al. A Porphyrin–Fullerene Dyad with a Supramolecular Double-Cable Structure as a Novel Electron Acceptor

- for Bulk Heterojunction Polymer Solar Cells. *Advanced Materials*. **2011**. *23*, 2951–2956.
- [199] Imahori, H. Porphyrin–Fullerene Linked Systems as Artificial Photosynthetic Mimics. *Organic & Biomolecular Chemistry*. **2004**. *2*, 1425–1433.
- [200] Ltaief, A.; Chaâbane, R.B.; Bouazizi, A.; Davenas, J. Photovoltaic Properties of Bulk Heterojunction Solar Cells with Improved Spectral Coverage. *Materials Science and Engineering: C*. **2006**. *26*, 344–347.
- [201] Natori, I.; Natori, S.; Hanawa, N.; Ogino, K. Controlled Self-Assembly of Porphyrin/Fullerene Donor–Acceptor Complex in a Polymer Thin Film. *Journal of Polymer Science Part B: Polymer Physics*. **2014**. *52*, 743–746.
- [202] Wang, L.; Qiao, Z.; Gao, C.; Liu, J.; Zhang, Z.G.; Li, X.; Li, Y.; Wang, H. End-Capping Effect of Quinoxalino [2, 3-b?] porphyrin on Donor–Acceptor Copolymer and Improved Performance of Polymer Solar Cells. *Macromolecules*. **2016**.
- [203] Chevrier, M.; Richeter, S.; Coulembier, O.; Surin, M.; Mehdi, A.; Lazzaroni, R.; Evans, R.C.; Dubois, P.; Clément, S. Expanding the Light Absorption of Poly (3-hexylthiophene) by End-Functionalization with  $\pi$ -Extended Porphyrins. *Chemical Communications*. **2016**. *52*, 171–174.
- [204] Xiang, N.; Liu, Y.; Zhou, W.; Huang, H.; Guo, X.; Tan, Z.; Zhao, B.; Shen, P.; Tan, S. Synthesis and Characterization of Porphyrin-Terthiophene and Oligothiophene  $\pi$ -Conjugated Copolymers for Polymer Solar Cells. *European Polymer Journal*. **2010**. *46*, 1084–1092.
- [205] Andernach, R.E.; Rossbauer, S.; Ashraf, R.S.; Faber, H.; Anthopoulos, T.D.; McCulloch, I.; Heeney, M.; Bronstein, H.A. Conjugated Polymer–Porphyrin Complexes for Organic Electronics. *ChemPhysChem*. **2015**. *16*, 1223–1230.

- [206] Woo, C.H.; Thompson, B.C.; Kim, B.J.; Toney, M.F.; Fréchet, J.M. The Influence of Poly (3-hexylthiophene) Regioregularity on Fullerene-Composite Solar Cell Performance. *Journal of the American Chemical Society*. **2008**. *130*, 16324–16329.
- [207] Clark, J.; Chang, J.F.; Spano, F.C.; Friend, R.H.; Silva, C. Determining Exciton Bandwidth and Film Microstructure in Polythiophene Films Using Linear Absorption Spectroscopy. *Applied Physics Letters*. **2009**. *94*, 163306.
- [208] Westacott, P.; Tumbleston, J.R.; Shoaee, S.; Fearn, S.; Bannock, J.H.; Gilchrist, J.B.; Heutz, S.; Heeney, M.; Ade, H.; Durrant, J.; et al. On the Role of Intermixed Phases in Organic Photovoltaic Blends. *Energy & Environmental Science*. **2013**. *6*, 2756–2764.
- [209] Zhang, Y.; Yip, H.L.; Acton, O.; Hau, S.K.; Huang, F.; Jen, A.K.Y. A Simple and Effective Way of Achieving Highly Efficient and Thermally Stable Bulk-Heterojunction Polymer Solar Cells Using Amorphous Fullerene Derivatives as Electron Acceptor. *Chemistry of Materials*. **2009**. *21*, 2598–2600.
- [210] Park, S.H.; Roy, A.; Beaupre, S.; Cho, S.; Coates, N.; Moon, J.S.; Moses, D.; Leclerc, M.; Lee, K.; Heeger, A.J. Bulk Heterojunction Solar Cells with Internal Quantum Efficiency Approaching 100&Percent. *Nature Photonics*. **2009**. *3*, 297–302.
- [211] Kato, N.I. Reducing Focused Ion Beam Damage to Transmission Electron Microscopy Samples. *Journal of Electron Microscopy*. **2004**. *53*, 451–458.
- [212] Graham, K.R.; Stalder, R.; Wieruszewski, P.M.; Patel, D.G.; Salazar, D.H.; Reynolds, J.R. Tailor-Made Additives for Morphology Control in Molecular Bulk-Heterojunction Photovoltaics. *ACS Applied Materials & Interfaces*. **2012**. *5*, 63–71.



- [213] Lobe, J.M.; Andrew, T.L.; Bulovic, V.; Swager, T.M. Improving the Performance of P3HT–Fullerene Solar Cells with Side-Chain-Functionalized Poly (Thiophene) Additives: a New Paradigm for Polymer Design. *ACS nano*. **2012**. *6*, 3044–3056.

# Appendices

# Appendix A

## Experimental Procedures and Techniques for Data Interpretation

## A.1 Synthesis of Poly(3-hexylthiophene)s

As discussed in Chapter 1, poly(3-hexylthiophene)s (P3HT) synthesized via the GRIM method are unique for the control provided by the nickel-catalyzed cross coupling mechanism that yields well-defined P3HTs with tuneable MW, end-group composition, and regioregularity. As the name suggests, the success of the GRIM method is dependent upon the careful handling of a highly reactive alkyl halomagnesio (MgX) reagent, which is extremely moisture sensitive. This section outlines the procedure for the synthesis of highly regio-regular P3HT used in this dissertation. Detail is given on how to synthesize a batch featuring 1.00 g DB3HT (monomer) and includes information on the post-processing techniques used to obtain well-defined P3HTs. **Note: Grignard reagents react violently upon exposure to moisture, and as such, proper PPE including safety glasses, lab coat, and gloves should be worn when handling the Grignard materials.**

Perhaps the most critical step determining the control over the growth of P3HTs is the conversion of 2,5-dibromo-3-hexylthiophene (DB3HT) to the active Grignard isomer 2-bromo-5-chloromagnesio-3-hexylthiophene. This isomer is desired as it exclusively participates in the growth of P3HTs when using [1,3-Bis(diphenylphosphino)propane]dichloronickel(II) (NidpppCl<sub>2</sub>) as the catalyst. Because the hexyl chain of the active isomer interacts with the phosphine ligand of the catalyst, the resulting P3HTs are assembled with a majority of head-to-tail couplings and a high degree of regioregularity. The two most common Grignard reagents used for the monomer conversion are isopropyl magnesiumchloride (i-PrMgCl) and tert-butyl magnesiumchloride (t-buMgCl). In the reactions performed in this dissertation, i-PrMgCl is used as it features a long shelf life and provides high yields of the active isomer (75-80%).

### A.1.1 Grignard Conversion to the Activated Monomer

To perform the Grignard conversion of DB3HT, start by allowing a hot, clean, 3-neck round bottom (RB) flask (250 mL) and stir bar to cool under argon flow. Once cooled, carefully add  $\approx 1.0$  g of DB3HT and record the amount added. Next, add a condenser to the middle-connector of the 3-neck RB flask and seal the remaining connectors and the connector atop the condenser with rubber septa. Next, pull vacuum on the entire assembly and heat the condenser and arms of the RB flask using a heat gun to remove any residual moisture. Once hot to the touch, allow argon to flow through the reactor flask until the reactor cools. Once cool,  $\approx 40$  mL of THF is added to the RB flask. Using a 6 in needle, allow argon to bubble through the solution for  $\approx 5$  min. After 5 min, i-PrMgCl is added at .98:1 (i-PrMgCl:DB3HT) by mole to the RB flask under argon flow. The RB flask is then heated to 74 °C and allowed to reflux overnight.

### A.1.2 Preparation of GC-MS Sample

The conversion of DB3HT to the active isomer is monitored by gas chromatography-mass spectroscopy and performed as follows: While maintaining inert conditions,  $\approx 1$  mL of the reactor solution is withdrawn and dispensed into a scintillation vial containing hexanes/4M HCl, which is shaken vigorously. The HCl will protonate the Grignard functional groups of the active, inactive, and di-converted monomers, which will dissolve in the hexanes layer. Aliquots from the hexanes layer can then be used to analyze in the GC-MS, an example of which is shown in Figure 1.5.

### A.1.3 Growth of P3HTs via the KCTP Mechanism

Once the fraction of active isomer is determined, the growth of P3HTs is initiated by addition of the Ni(dppp) catalyst to achieve the target MW according to Equation 1.1. After allowing the reactor solution to cool to room temperature, the powder catalyst is added to the reactor under argon flow and stirred vigorously. As the reaction proceeds, the color will change from a pale yellow color to a deep red, which

is indicative of P3HT chain growth. After 20 min of stirring, the reaction is quenched with 20 times excess of allylmagnesium bromide or HCl (4M) with respect to the catalyst to cap the P3HT chains with allyl- or H-functional groups, respectively. After addition of the capping agent, the reaction is stirred for 5 min and then precipitated into copious amounts of cold methanol (up to 400 mL for a 40 mL reactor volume). The MeOH should immediately turn cloudy and dark as the P3HT is precipitated, and this suspension is then moved to a refrigerator overnight. The P3HT products were purified via soxhlet extraction with MeOH and acetone, and the P3HTs were recovered using chloroform.

## A.2 Hydrosilylation of P3HTs

Chlorosilane-terminated P3HTs were prepared by adding 100 mg of allyl-terminated P3HTs in a clean, dry RB flask. The RB flask was then sealed with a rubber septa and allowed to purge with argon for 2-3 minutes to remove any ambient air from the system. Next, 40 mL of dry benzene was added to the RB flask and stirred until all of the product was completely dissolved. Argon was bubbled through the solution using a 6  $\in$  needle for  $\approx$  5 min. While the RB flask solution is purging, a freshly cleaned (via base bath and rinsed with DI water), dry Schlenk bomb flask is prepared by adding 2-3 mL of dimethyl chlorosilane under positive argon pressure. An example of an appropriate Schlenk flask is shown in Figure A.1. The flask is then sealed, heated, and stirred vigorously such that the chlorosilanes have adequate opportunity to react with the entirety of the inside of the Schlenk flask. After 2-3 min, the Schlenk flask is opened to vacuum to remove any unreacted silanes. From this point forward, it is critical that the Schlenk flask remains under vacuum or positive argon pressure.

The allyl-terminated P3HTs are transferred from the RB flask to the Schlenk flask via a cannula needle using argon to provide the backpressure to initiate flow of the benzene solution. Once the solution is transferred, argon pressure is maintained over Schlenk flask while  $\approx$  1 mL of Karstedt's catalyst is added to the benzene solution. Finally, 2 mL of dimethylmonochlorosilane is added and the Schlenk flask is sealed at the valve. Once sealed, the Schlenk flask is heated to 80  $^{\circ}$ C and stirred overnight, or for at least 18 h. Once the reaction is complete, the reactor's contents are frozen using liquid nitrogen and the benzene is removed via sublimation, which also removes any unreacted monochlorosilane. It is important at this point that the reactor remain air-free to ensure the reactivity of the chlorosilane-capped P3HTs. Any further processing is dependent upon the intended use for the chlorosilane-capped P3HTs.



**Figure A.1:** Schlenk flask used for hydrosilylation reactions that is fabricated from heavy boiling flasks.



## A.3 Piranha Cleansing Method

**Note: Piranha acid is both a strong acid and oxidizing agent and is, therefore, extremely dangerous! Heavy lab coats, gloves, and safety glasses should always be worn when handling piranha acid solutions.**

This section outlines a procedure for piranha solutions totaling 32 mL and can be scaled for larger volumes so long as the proper ratio of 3:1 v/v  $\text{H}_2\text{SO}_4:\text{H}_2\text{O}_2$  is maintained. First start by acquiring a clean 250 mL beaker *that lacks any cracks or signs of etching (from previous piranha cleanings) and that is at room temperature. Take careful note of the cleanliness of the beaker as piranha solution will react violently if any organic materials remain in the beaker, potentially resulting in an explosion.* Beakers with shallower profiles make it easier to remove the samples later on in the procedure. Next, place the wafers or glass substrates to be cleaned in the bottom of the beaker, taking care to ensure that surfaces are not overcrowded or stuck to one another. Using a clean graduated cylinder, carefully dispense 24 mL of sulfuric acid into the beaker containing the substrates. If not already done, place the beaker in a fume hood in near proximity to a hot plate that is preheated to 70 °C. Using a different graduated cylinder than was used to measure the acid, carefully measure 8 mL of  $\text{H}_2\text{O}_2$ . *Take extreme care not to exceed %50  $\text{H}_2\text{O}_2$  in the final solution as it may explode upon mixing.* Slowly add the  $\text{H}_2\text{O}_2$  to the beaker by pouring down the side of the beaker to slow down the initiation of the reaction and reduce the risk of splashing. The solution will begin to react immediately, which will result in rapid heating and the release of corrosive fumes and  $\text{O}_2$ . Once the solution has reached an equilibrium, the beaker should be transferred to the preheated hot plate, which will extend the lifetime of the piranha solution.

After 20-30 min, the substrates can be removed from the piranha solution. *Note: Piranha solution relies on boiling to help remove contaminants from the substrates being cleaned. Therefore, if the solution has neutralized and is no longer boiling, the addition of 1-2 mL of  $\text{H}_2\text{O}_2$  can be performed to reinvigorate the reaction.* Using

tweezers, remove each substrate from the piranha solution and immediately rinse with copious amounts DI water via a strong stream from a wash bottle. If properly cleaned, the substrates should be hydrophilic and therefore water should readily wet the entire surface. The presence of any dry spots on the substrates typically suggest that some hydrophobic contaminant resides on the surface and should be re cleaned. After rinsing, each substrate should be dried using a filtered stream of N<sub>2</sub>. Once all substrates have been cleaned, remove the beaker from the hotplate and allow it to cool to room temperature.

Make sure the piranha acid solution has completely cooled to room temperature before being disposed. Once cooled, the solution should be disposed into an acid waste container featuring a vent mechanism to release any gases that have yet to release from the solution. **Caution: Take extra caution to properly dispose piranha solution in containers that contain absolutely no organic materials as an explosion could occur!**

## A.4 Derivation of Mass Balance in Binary Films for NR Modeling

The mass balance presented herein assume the densities of each phase,  $\rho_i$ , remain constant. It is convenient here to represent the masses of each material,  $m_i$ , by an effective layer thickness  $\mu_i$ .

$$\mu_i = \frac{m_i}{\rho_i A} \quad (\text{A.1})$$

Here,  $A$  is the lateral area of the film. By adopting this convention, it follows that the overall composition of the PCBM within the film can be expressed as a volume fraction,  $\nu$ , as follows:

$$\mu = \nu(\mu_{PCBM} + \mu_{P3HT}) \quad (\text{A.2})$$

The total mass of PCBM present in the system can also be expressed as the sum of each of its volume fractions  $\phi_n$  of each layer. For example,

$$\mu_{PCBM} = \sum_{n=1}^{layer} \phi_n d_n \quad (\text{A.3})$$

and similarly, the total mass of P3HT can be calculated based on the PCBM volume fraction:

$$\mu_{P3HT} = \sum_{n=1}^{layer} (1 - \phi_n) d_n. \quad (\text{A.4})$$

The total mass present in the binary system is then equal to the sum of each of the total effective masses and the total thickness.

$$\mu_{P3HT} + \mu_{PCBM} = \sum_{n=1}^{layer} (1 - \phi_n) d_n + \sum_{n=1}^{layer} \phi_n d_n = \sum_{n=1}^{layer} d_n \quad (\text{A.5})$$

By substituting the LHS of Equation A.5 into A.2 a relationship is developed that constrains each layer's PCBM content to the volume fraction of the film.

$$\mu_{PCBM} = \nu \left( \sum_{n=1}^{layer} d_n \right) = \sum_{n=1}^{layer} \phi_n d_n \quad (\text{A.6})$$

This form represents a general mass balance for an  $n$  layer system providing a means of retaining realistic PCBM loadings between modeling schemes (different numbers of layers) or before and after annealing. Equations A.8-1.7 represent mass balances for cases involving 1-3 layers, respectively, and are the general forms for the fitting of the data collected in this dissertation work.

$$\mu_{PCBM} = \nu d = \phi_1 d_1 \quad (\text{A.7})$$

$$= \nu (d_1 + d_2) = \phi_1 d_1 + \phi_2 d_2 \quad (\text{A.8})$$

$$= \nu (d_1 + d_2 + d_3) = \phi_1 d_1 + \phi_2 d_2 + \phi_3 d_3 \quad (\text{A.9})$$

## A.5 MALDI Analysis of Polymer End-Groups

Matrix Assisted Laser Desorption Ionization Time of Flight Mass Spectroscopy measurements were performed on P3HTs to obtain the distribution of end groups. For each sample, regardless of end groups, the general procedure that was performed is outlined as follows. As a rule, polystyrene (PS) standards were made each time MALDI measurements were recorded. First, weight out the following materials:

- 1-2 mg per analyte
- 1-2 mg of matrix per sample
- 2-3 mg of Ag acetate
- 1-2 mg of appropriate PS standard

The MW of the PS standard is chosen to match that of the sample polymer as close as possible. For P3HT samples, trans-2[3-(4-tert-butylphenyl)-2-methyl-2-propenylidene was used as the choice of matrix for most of the measurements in this work. The only exception is in Chapter 4, in which dithranol and cyclohexanoic acid were also used as matrix materials in an attempt to measure the end groups of the PP-P3HTs. The analytes, Ag, and standard are dissolved in THF to 10 mg/mL, while the matrix is dissolved to 20 mg/mL. The final spotting solutions are mixed in ratios of 10:1 of matrix:analyte for the P3HT samples and 20:2:1 of matrix:analyte:Ag for the standard. These solutions were used to spot the MALDI target using a 10  $\mu$ L pipette. Clean spots were obtained by dispensing  $\approx 1$   $\mu$ L at a time on each spot, allowing them to dry, and then repeated until sufficient material is deposited for analyzing.

At the beginning of each set of MALDI measurements, the PS standard was used to calibrate the detector such that the  $m/z$  values were accurate. The collected spectra were analyzed manually using an Excel sheet to calculate the appropriate  $m/z$  values for each of the possible end group distributions. A simple example spectra is shown

for H/Br terminated P3HTs in Figure A.2, where only one distribution was obtained for the H/Br end group. The calculated values for the H/H and Br/Br groups are shown as the red dashed lines.

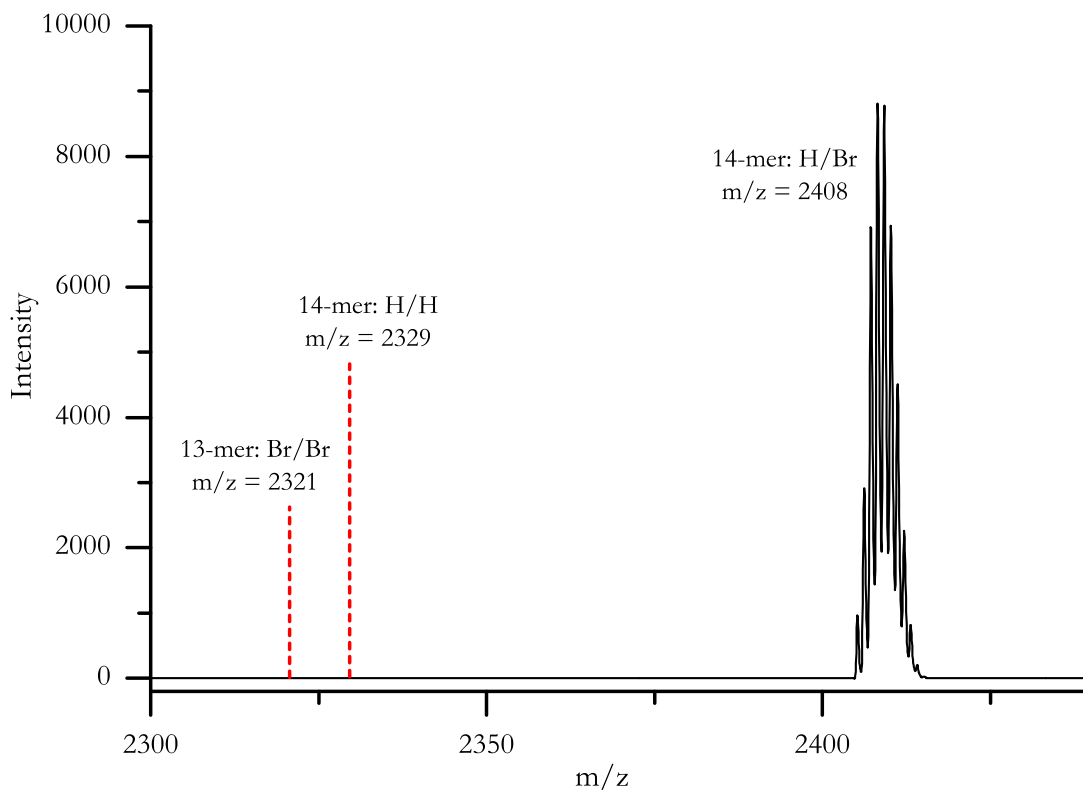


**Figure A.2:** Close up view of MALDI spectra of an ideal synthesis of H/Br terminated P3HT that features only one distribution of end groups that correspond to H/Br. The red dashed lines indicate the m/z values where Br/Br or H/H end groups would appear.

## A.6 Cross-Sectional TEM Sample Preparation via the Liftout Method

Lamella for TEM measurements were fabricated using a Ga focused ion beam (FIB) located within a scanning electron microscope (SEM). In this instrument, the SEM is used to navigate the sample while milling and welding processes are accomplished using the FIB. Milling lamella using the SEM/FIB microscope is particularly challenging for most organic materials as the beams can cause material damage or alter the morphology through thermal annealing processes. Therefore, to prevent milling-induced damage effects on the P3HT-PCBM films studied in Chapter 2 of this dissertation, many precautions were taken.

Before entering the SEM chamber, samples were sputter-coated with Au as shown in Figure A.3A. The Au coating is applied to prevent damage from the electron beam while focusing and aligning the electron and gallium beams, which is necessary before Pt protective layers can be applied. Once the beams are focused and the sample is located at the coherent point, where the  $e^-$  and Ga beams cross, a thin protective layer is applied using the  $e^-$  beam. This thin layer helps protect the future work area during the early stages of Pt deposition using the Ga beam that would otherwise alter morphology at the film/air interface. As a final protective measure, a rectangular region of approximately  $5 \times 20 \mu\text{m}$  is coated with Pt using the Ga beam at a relatively low beam current (30 kV, 100 pA). Figure A.3B illustrates the film after these coating processes, where the dark rectangle is the Pt coating atop the region that will become the lamella. The lighter gray color covering the left 90% of the image is the result of FIB damage occurring atop the thin Pt layer applied by the  $e^-$  beam.

The milling steps entail the use of an intense Ga beam (30 kV, 2 nA) to remove trenches on 3 sides of the lamella as shown in Figure A.3C-D. These trenches are milled to a depth of 10  $\mu\text{m}$  up to the edge of the Pt protective layer over the lamella. The trench at the end of the lamella is removed to provide room to maneuver the lift

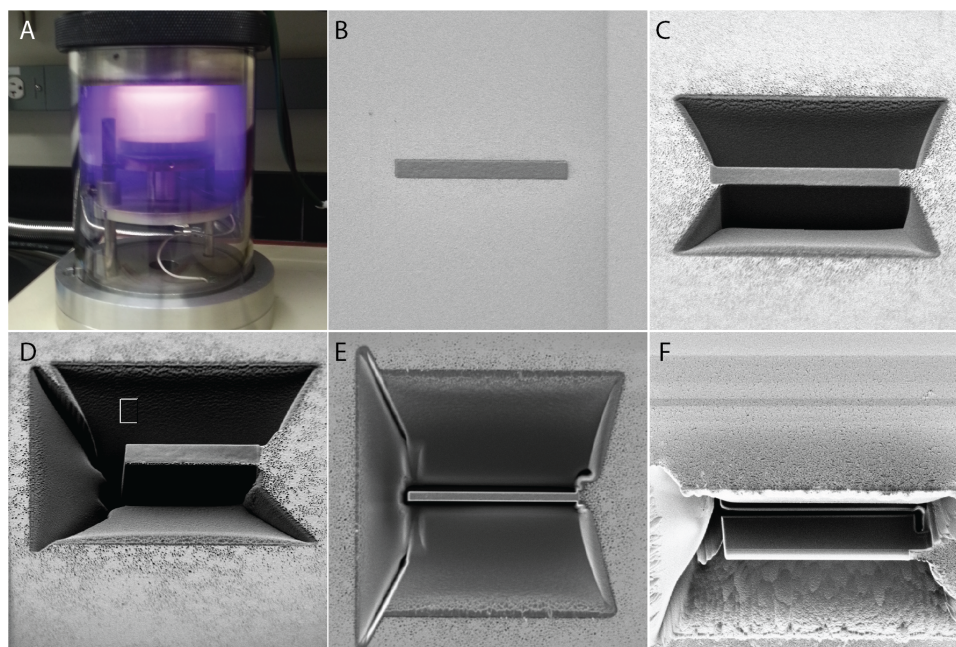


**Figure A.3:** Image sequence depicting the first stages of the lift out process: Au deposition (A), Pt lamella protective layer (B), front and rear trench milling (c), side-trench milling (D), lamella thinning (E), and side and bottom initial milling (E).

out needle once it is welded to the lamella in later steps. Because the larger beam used to mill the trenches induces severe sample damage, each face of the lamella must be refined using a smaller beam. To accomplish this process, a smaller beam of 30 kV, 200 pA is used to mill the lamella down to approximately  $2 \times 20 \mu\text{m}$  as shown in Figure A.3E. The last step to prepare the sample for the lift out process is to mill a line across the lamella at the bottom of the trench and partially up the attached side. At this point the lamella is only attached at the top right corner as it is presented in Figure A.3F.

After the trench-milling processes are complete, the next step is to carefully manipulate the lift out probe to the corner of the lamella. Once in position, the lift out probe is Pt-welded to the lamella using a low beam intensity of 30 kV, 100 pA. The lamella is extremely vulnerable at this stage because is attached to the lift out needle and the substrate at opposite corners. Therefore, the final bit of material holding the lamella to the substrate is removed as quickly as possible using a 30 kV,



100 pA Ga beam. Once the material is removed, the lamella is carefully lifted out of the trench as shown in Figures A.4A and A.4B. Once the lamella is clear of the trench area, the substrate is lowered away and a special TEM grid is installed into the SEM sample stage.

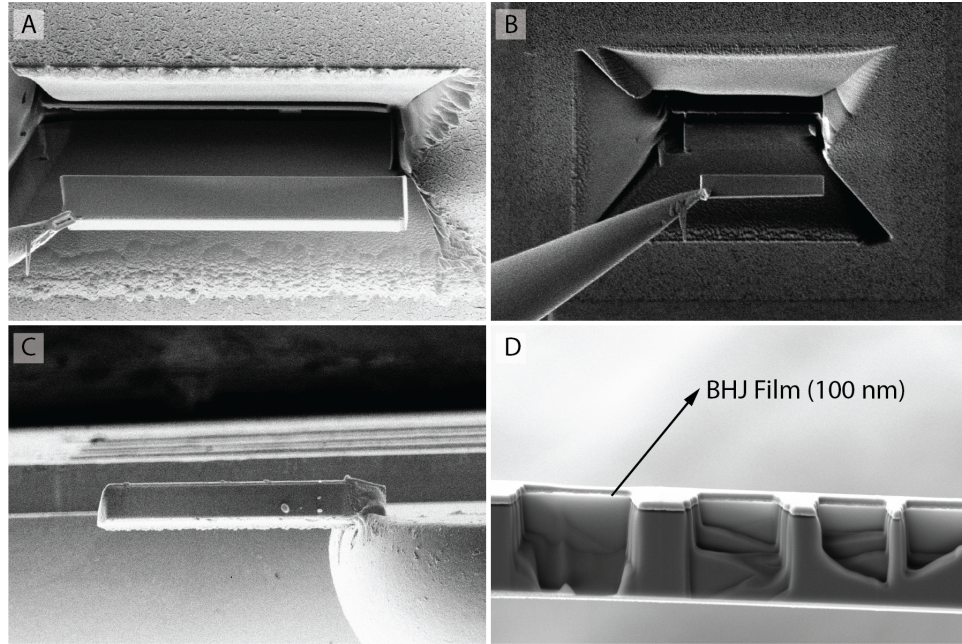


**Figure A.4:** Image sequence of the lift out process after welding the lift out needle to the lamella zoomed (A) and a wide angle view (B). The lamella welded to the post of the TEM sample grid (C) and finally the sample after final milling and polishing (D). Not the bright white line in image D corresponding to the BHJ film.

The lamella is attached to the TEM grid at one end by using a large beam (30 kV, 2 nA) in cutting mode while manually opening the Pt gas valve. This strategy allows for significant penetration of the Ga beam through the lamella and into the TEM grid and provides a robust full penetration weld as shown in Figure A.4C. The final thinning stages of the lamella preparation process entails thinning down small windows to  $\approx 60$  nm using a low beam current of 30 kV and 20 to 50 pA depending on the amount of material needing to be removed. These windows are not milled throughout the entire face of the lamella resulting in a trapezoidal profile from the side. The increased thickness along the bottom of the lamella provide strength

to prevent the it from breaking off during sample storage and handling. A final polishing step is performed by rastering an extremely light beam of 5 kV and 20 pA across the face of the lamella. An example lamella ready for TEM measurements is shown in Figure A.4D, where the thin BHJ layer is shown as a bright white line and is noticeably darker in the regions outside the milled windows.

The progressively lower Ga beam intensities are chosen to limit the damage to the faces of the lamella.<sup>139,211</sup> The final polishing beam parameters are specifically chosen to limit excessive heating of the lamella faces and therefore ensure that the remaining material is undamaged and representative of its state in the film prior to milling. The local heating due to an incident ion beam has been described by Bassim et al. and is shown in Equation A.10.<sup>139</sup>

$$\Delta T = \frac{JV}{2k}r_0 \quad (\text{A.10})$$

Here,  $\Delta T$  is change in temperature,  $J$  is the FIB current density,  $V$  is the accelerating voltage,  $k$  is the thermal conductivity of the material, and  $r_0$  is the radius of the beam. The current density is described by Equation A.11, where  $I$  is the beam current.

$$J = \frac{I}{\pi r_0^2} \quad (\text{A.11})$$

To summarize the analysis, beam currents  $\leq 50$  pA with accelerating voltages  $\leq 10$  kV are sufficient to limit heating of the sample during the final polishing step.

# Appendix B

## Supporting Information

## B.1 Chapter 1

Placeholder for organization so that appendix section numbers correspond to chapter numbers.

## B.2 Chapter 2

### B.2.1 SEC Elugrams

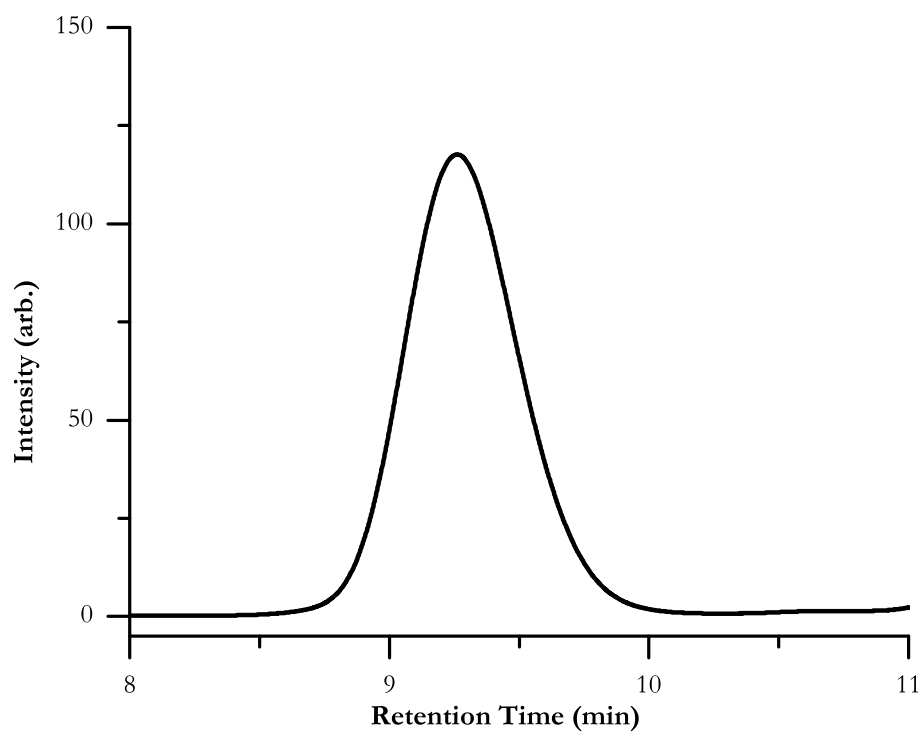


**Figure B.1:** SEC elugram for allyl-P3HTs used for all of the brushes in Chapter 2.

## B.2.2 NMR

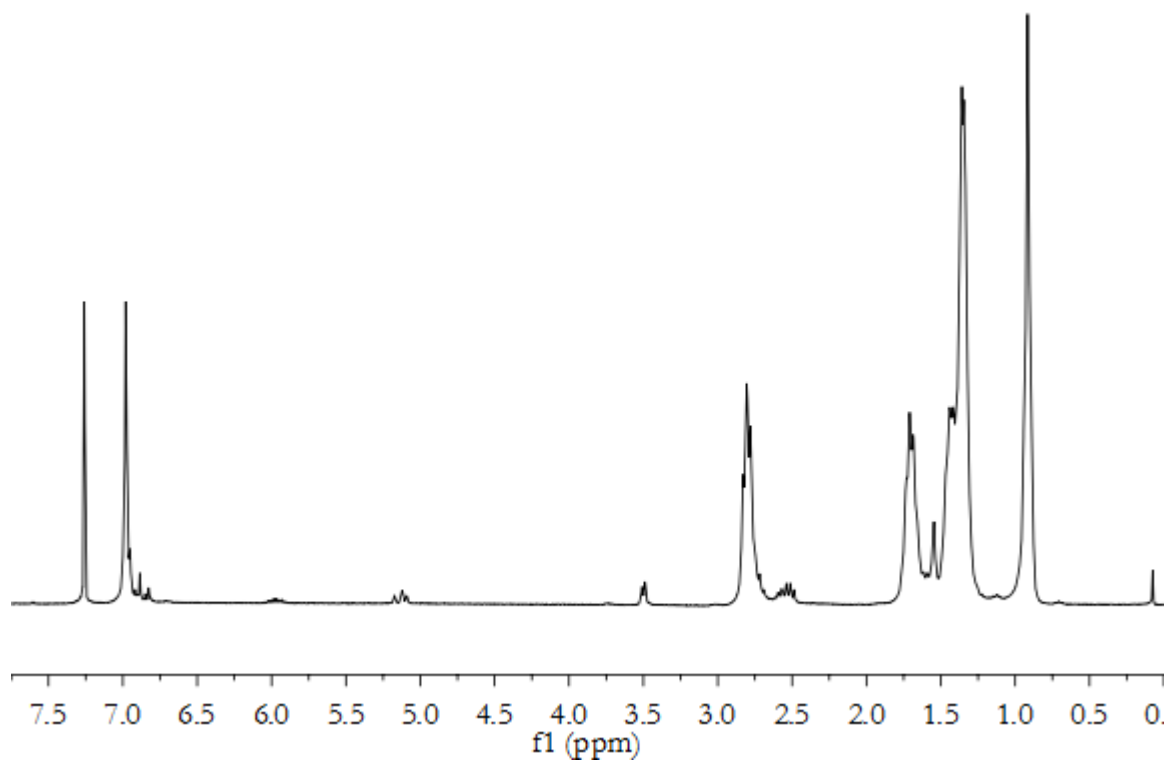


**Figure B.2:** Full  $^1\text{H}$ NMR spectra of allyl-P3HT in  $\text{CDCl}_3$  at 300 MHz. Peak List: 7.25, 7.24, 6.98, 6.97, 6.95, 6.94, 6.87, 6.81, 3.49, 3.47, 2.82, 2.79, 2.76, 2.73, 2.70, 2.56, 2.52, 2.50, 1.74, 1.72, 1.72, 1.69, 1.67, 1.64, 1.63, 1.60, 1.58, 1.53, 1.45, 1.42, 1.38, 1.37, 1.35, 1.34, 1.33, 1.32, 1.30, 1.28, 1.25, 1.24, 0.97, 0.95, 0.92, 0.90, 0.89, 0.88, 0.86, 0.06.

### B.2.3 MALDI

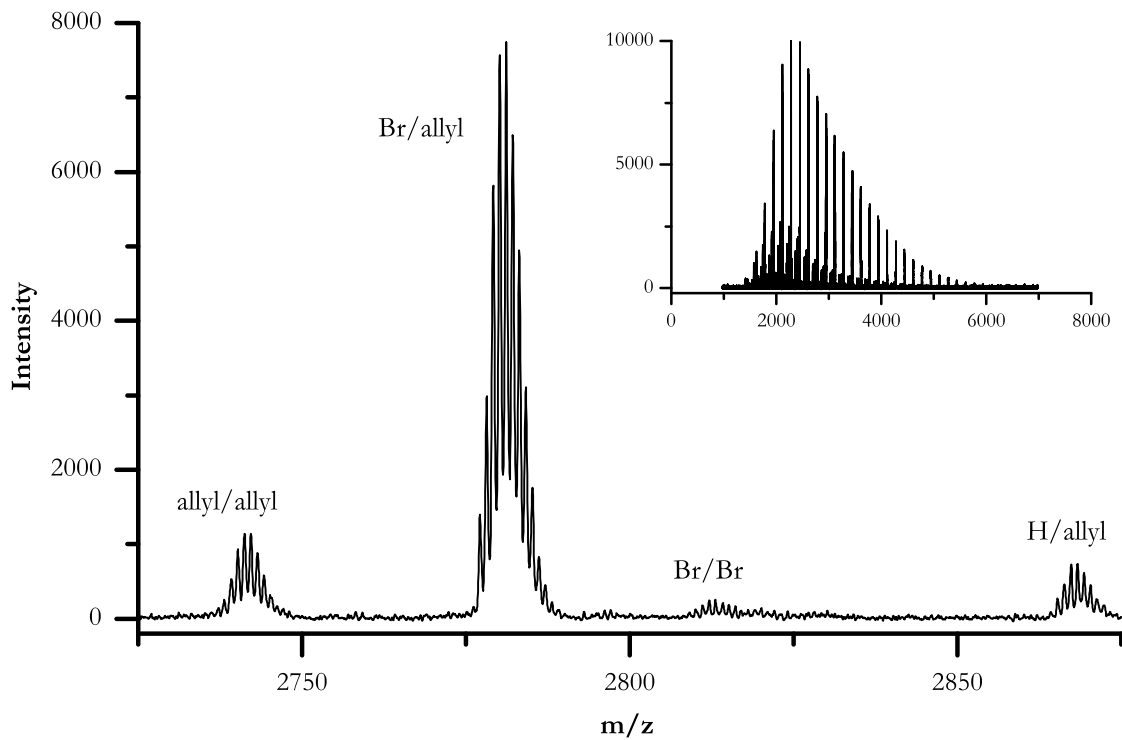


**Figure B.3:** Cropped MALDI-TOF spectrum of allyl-P3HT where the distributions for the end groups consisting of allyl/allyl, Br/allyl, Br/Br, and H/allyl are labeled respectively. The inset graph shows the full spectrum.

## B.3 Chapter 3 Supporting Information

### B.3.1 List of P3HT-PCBM BHJ Additives

**Table B.1:** Literature summary of relatively low MW additives used to modify BHJ films. Only the best performing device from each study is listed and the first PCE listed corresponds to the best performing additive-modified device from each report while the second refers to the control. To conserve space, many names have been abbreviated. See Table B.2 for a comprehensive list of these abbreviations names and chemical structures.

Additive	Size kDa	Loading wt. %	PCE	Device Architecture
P3HT-b-P4VP <sup>155</sup>	17	5.0	1.1/0.7	ITO/PEDOT:PSS/BHJ/LiF/Al
P3HT-b-PMMA <sup>56</sup>	21	1.0	3.6/3.9	ITO/PEDOT:PSS/BHJ/Ca/Al
P3HT-b-PEO <sup>56</sup>	13	1.0	3.7/3.9	ITO/PEDOT:PSS/BHJ/Ca/Al
P3HT-3Py <sup>56</sup>	8.0	1.0	4.3/3.9	ITO/PEDOT:PSS/BHJ/Ca/Al
8T-C60 <sup>146</sup>	21	5.0	2.5/1.9	ITO/TTIP/BHJ/Au
P3HT-b-C60 <sup>147</sup>	6.0	2.5	2.8/1.2	ITO/PEDOT:PSS/BHJ/Al
P3HT-b-P4VP <sup>151</sup>	7.5	8.0	4.1/2.8	ITO/TiOX/BHJ/MoO3/Ag
P3HT-b-PS <sup>149</sup>	13.3	5.0	3.8/3.3	ITO/PEDOT:PSS/BHJ/Ca/Al
PTPA-b-P3HT <sup>154</sup>	27.0	1.5	4.4/3.9	ITO/PEDOT:PSS/BHJ/Ca/Al
2-C6Si <sup>212</sup>	0.9	20.0	2.2/0.4	ITO/PEDOT:PSS/BHJ/Ca/Al
P(3HT-C6F5) <sup>213</sup>	15	0.25	3.8/2.9	ITO/PEDOT:PSS/BHJ/Ca/Al
ThPP <sup>193</sup>	12	1.0	1.1/0.9	ITO/PEDOT:PSS/BHJ/Al



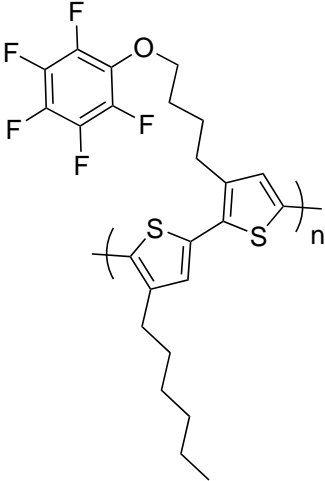
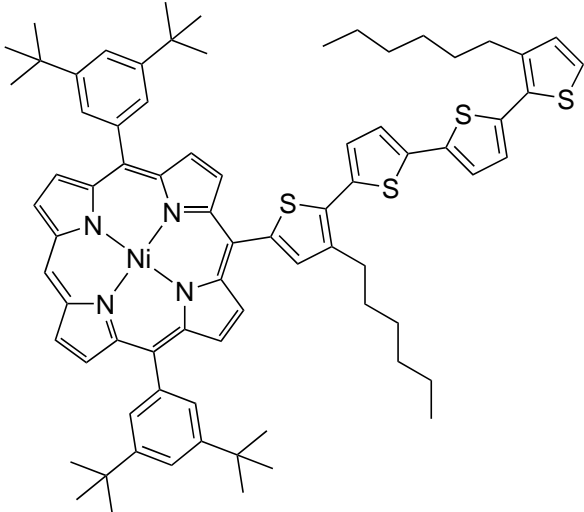
**Table B.2:** List of the chemical structures of additives that have been incorporated in P3HT-PCBM BHJ OPV devices as summarized in B.1.

Short Name	Chemical Structure
TTIP	
P3HT-b-P4VP	
P3HT-b-PMMA	
P3HT-b-PEO	
P3HT-b-PS	
P3HT-b-3Py	

Table B.2 Continued.

Short Name	Chemical Structure
8T-C60	
P3HT-b-C60	
PTPA-b-P3HT	
2-C6Si	

Table B.2 Continued.

Short Name	Chemical Structure
P3HT-C6F5	 <p>The structure shows a poly(3-hexylthiophene) backbone. One of the thiophene rings in the chain is substituted with a 2,3,4,5-tetrafluorophenoxy group. The group consists of a benzene ring with fluorine atoms at the 2, 3, 4, and 5 positions, and an oxygen atom at the 1 position that is linked to the 3-position of the thiophene ring.</p>
ThPP	 <p>The structure shows a nickel(II) complex coordinated by two terphenyl ligands and two thienyl ligands. The terphenyl ligands are substituted with tert-butyl groups at the 2 and 6 positions of the outer rings. The thienyl ligands are substituted with a hexyl chain and a 2,5-dithienyl group.</p>

### B.3.2 GPC Elugrams for different MW P3HTs

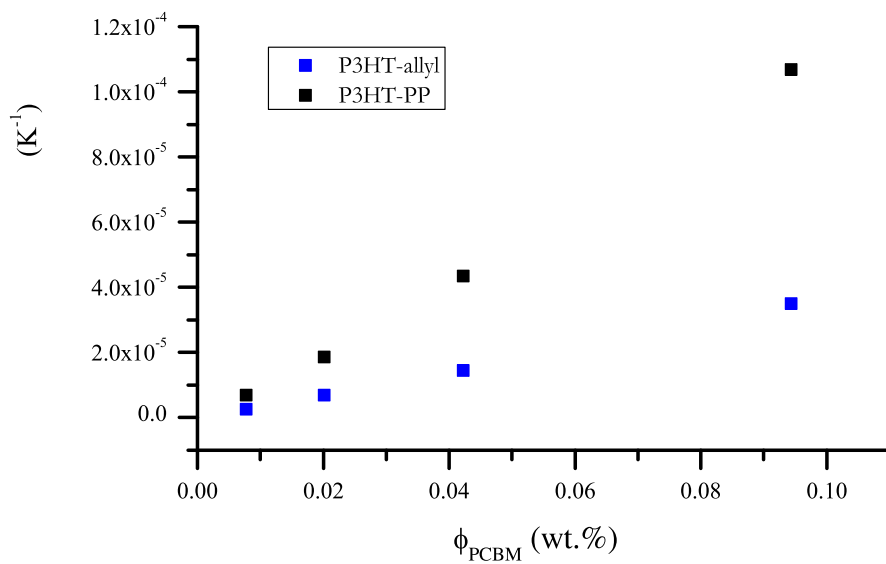


**Figure B.4:** SEC elugrams for 1.6k (blue), 4.4k (red), and 8.0k (black)P3HTs that were measured using polystyrene as the standard.

### B.3.3 NMR of Different Low MW P3HTs

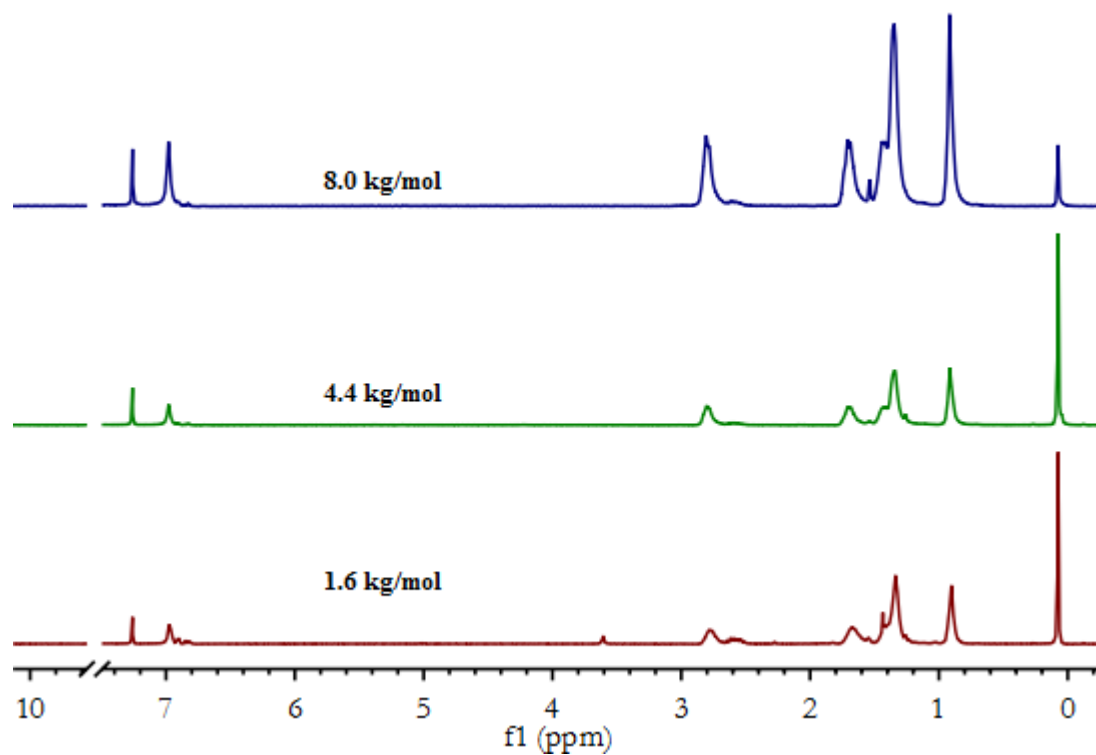


**Figure B.5:** NMR spectra used to estimate MW and regioregularity of the low MW P3HT additives used in Chapter 4.

## B.4 Chapter 4 Supporting Information

### B.4.1 GPC of P3HT-PPs

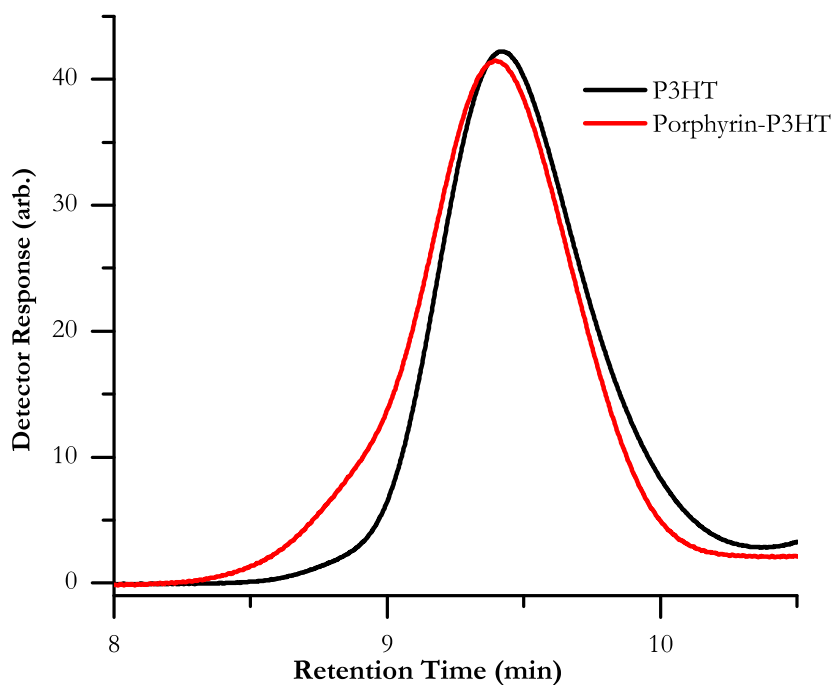


**Figure B.6:** SEC elugrams for allyl-terminated P3HT (black) and porphyrin-P3HT (red). The porphyrin-P3HT elutes earlier and broadens the MW distribution, suggesting that the coupling was successful.

## B.4.2 NMR of P3HT-allyl

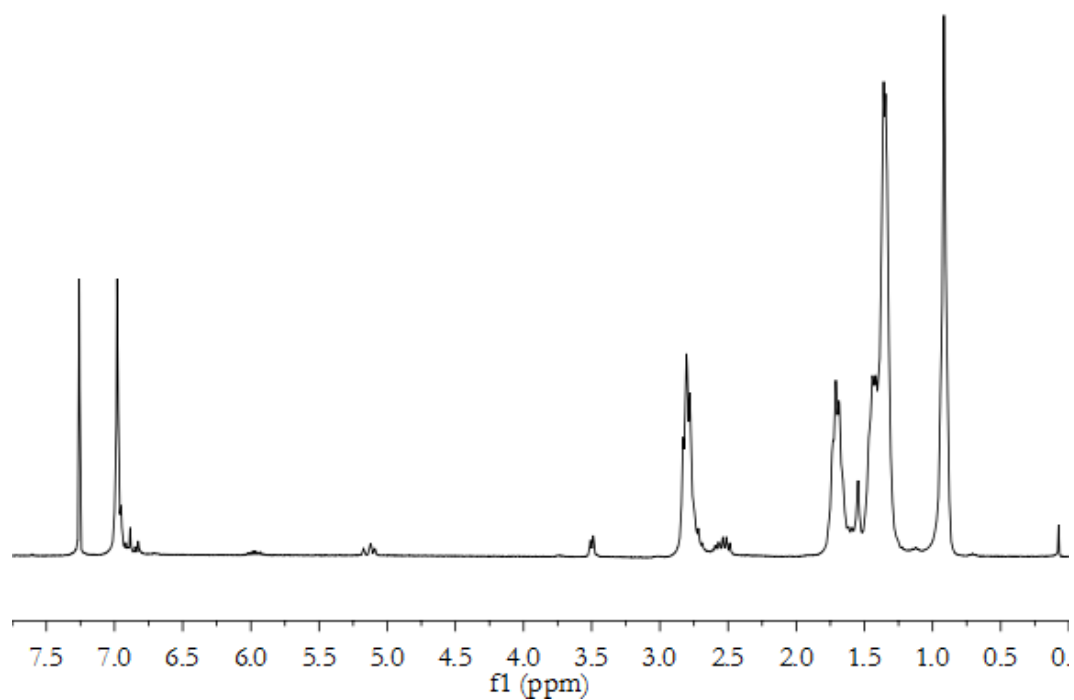


**Figure B.7:** NMR spectra for allyl-P3HT in  $\text{CDCl}_3$  at 300 MHz. Peak List: 7.25, 7.24, 6.98, 6.97, 6.95, 6.94, 6.87, 6.81, 3.49, 3.47, 2.82, 2.79, 2.76, 2.73, 2.70, 2.56, 2.52, 2.50, 1.74, 1.72, 1.72, 1.69, 1.67, 1.64, 1.63, 1.60, 1.58, 1.53, 1.45, 1.42, 1.38, 1.37, 1.35, 1.34, 1.33, 1.32, 1.30, 1.28, 1.25, 1.24, 0.97, 0.95, 0.92, 0.90, 0.89, 0.88, 0.86, 0.06.

### B.4.3 MALDI Spectra of P3HT-PP Intermediates

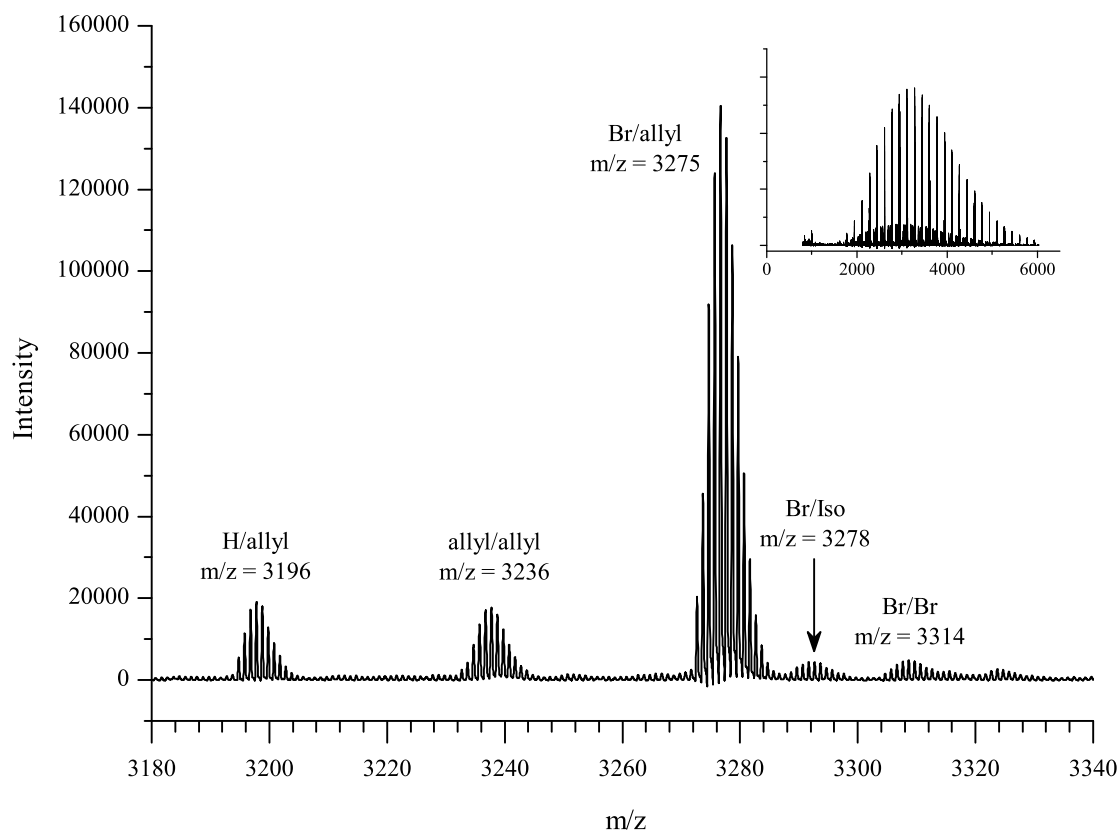


**Figure B.8:** Zoomed-in MALDI spectra for the 19-mer region of allyl-terminated P3HT used for the P3HT-PP coupling reactions. The inset graph shows the full spectrum.



#### B.4.4 Plots of $V_{oc}$ and FF as a Function of P3HT-PP Loading Level

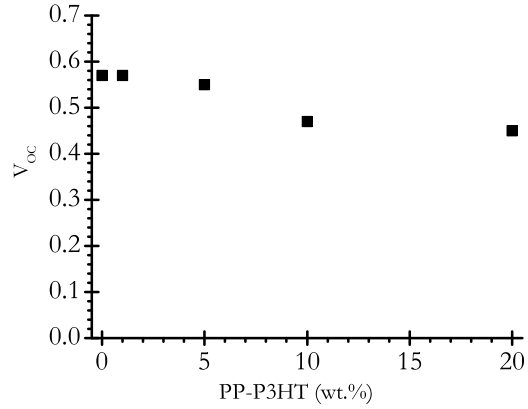


**Figure B.9:**  $V_{oc}$  as a function of P3HT-PP loading level that reveal a slight decrease as the PP-P3HT content is increased.

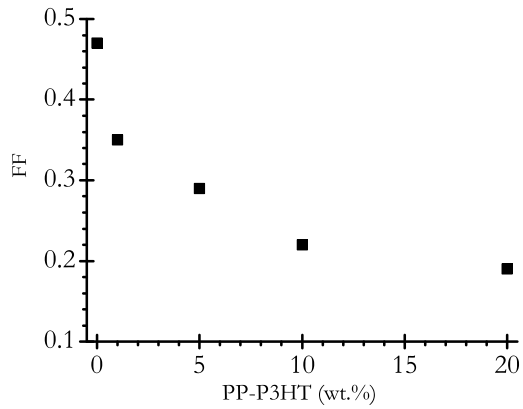


**Figure B.10:** Fill factor (FF) as a function of P3HT-PP loading level. The sharp decline in FF is a major driving force for the lackluster PCEs obtained for the PP-P3HT devices discussed in Chapter 4.

# Vita

Zach Daniel Seibers was born in Columbus, Mississippi, and raised in Shelbyville, Tennessee, where he attended Cascade School for kindergarten through 12th grade. Immediately after graduating in 2006, Zach attended Tennessee Technological University in Cookeville, Tennessee, and graduated with a B.S. in Chemical Engineering in 2011. He came to the University of Tennessee in 2012 to pursue a doctorate in Energy Science & Engineering, where he joined the research group of Prof. S. Michael Kilbey II and studied methods for controlling the morphology of bulk heterojunction-based organic photovoltaic devices.